UNIVERSITY OF CALIFORNIA SAN DIEGO

Simplifying Terrain Navigation with Soft Legs

A dissertation submitted in partial satisfaction of the
requirements for the degree
Doctor of Philosophy

in

Engineering Sciences (Mechanical Engineering)

by

Dylan Drotman

Committee in charge:

Professor Michael T. Tolley, Chair
Professor Nikolay Atanasov
Professor Todd Coleman
Professor Nick Gravish
Professor Miroslav Krstic

2021

The dissertation of Dylan Drotman is approved, and it is acceptable in quality and form for publication on microfilm and electronically.

University of California San Diego

2021

DEDICATION

I dedicate this to my family. You can now stop asking “Wait, you’re still in school?”

EPIGRAPH

Do not go where the path may lead,

go instead where there is no path

and leave a trail.

— Ralph Waldo Emerson

TABLE OF CONTENTS

LIST OF FIGURES

LIST OF TABLES

ACKNOWLEDGEMENTS

I would like to take a moment to express my gratitude towards people who have helped me along my PhD journey.

I would first like to thank my advisor Mike Tolley. I am so grateful for his guidance and support throughout my PhD. I thank Mike for being such a great leader and for helping me become a better researcher. Not only was Mike a great PhD advisor, but he was also a fun person to go surfing with. I couldn't have asked for a better advisor. I also thank Mike for making me submit to Science Robotics.

I would like to thank my dissertation committee members Miroslav Krstic, Todd Coleman, Nick Gravish, and Nikolay Atanasov for taking time to examine my thesis. I sincerely appreciate the feedback they provided over the course of my PhD.

I really appreciate Professor Mamadou Diagne and Kurt Talke for taking supportive roles in my development. Both of them provided guidance when it mattered and always pushed me to be successful. I can not thank them both enough.

I would like to thank the undergraduates who have helped me throughout my Ph.D. Kazu Otani, Philip deZonia, Tina Ghafel, Eric Shnell, Andrew Wang, David Sharp, and Christian Chan. I really couldn't have done this without them. Thanks Eric Shnell and Andrew Wang for all of the lasercutting. Thanks David Sharp and Christian Chan (and Saurabh Jadhav) for making so many soft valves.

I would also like thank my other co-authors/collaborators Saurabh Jadhav, Michael Ishida, Mark Hermes, Mitul Luhar, Paul Glick, Donald Ruffatto, Jeffrey Friesen, Tom Kalisky, Yueqi Wang, Eliah Aronoff-Spencer, Mahmood Karimi, Ben Shih, Caleb Christianson, Zhaoyuan Huo, Ruffin White, and Henrik I Christensen. I appreciate your time and effort you put forth on each publication.

I would like to thank the rest of the members of the Bioinspired Robotics and Design Lab for their valuable advice and suggestions during my PhD. I appreciated the camaraderie during

late night publication deadlines.

I would like to thank the supporting staff at UCSD such as Roxanne Vanderheiden, JV Agnew, Chris Cassidy, Tom Chauffant, Ioana Patringenaru, and David Baillot.

Lastly, my biggest thanks goes to my family and friends for all of the encouragement and support they have provided over the years. Many thanks to them for listening to my complaints and for pushing me to become the best version of myself.

The material enclosed in this dissertation are from three different publications focused on the design, control and actuation of soft legged robots.

Chapter 2 uses the material as it appears in the published paper in IEEE/ASME Transactions on Mechatronics 2018, D. Drotman, M. Ishida, S. Jadhav, M.T. Tolley "Application-Driven Design of Soft, 3-D Printed, Pneumatic Actuators With Bellows." The dissertation author was the first author and primary investigator of this material.

Chapter 3 uses the material currently in preparation for the journal Soft Robotics 2021, D. Drotman, P. Glick, M.T. Tolley "Gait Sequence Optimization for Soft Legged Robots." The dissertation author was the first author and the primary investigator of this material.

Chapter 4 uses the material as it appears in the published paper in Science Robotics 2021, D. Drotman, S. Jadhav, D. Sharp, C. Chan, M.T. Tolley "Pneumatic circuits for controlling the gaits of soft legged robots." The dissertation author was the first author and the primary investigator of this material.

The work in this manuscript is supported by the Frontiers of Innovation Scholarship Program (FISP) and Office of Naval Research, grant numbers N00014-17-1-2062 and N00014-18-1-2277.

VITA

2013	B. S. in Mechanical Engineering, University of California San Diego
2015	M. S. in Engineering Sciences (Mechanical Engineering), University of California San Diego
2017	Teaching Assistant University of California San Diego
2021	Ph. D. in Engineering Sciences (Mechanical Engineering), University of California San Diego

PUBLICATIONS

Drotman, D., Jadhav, S., Sharp, D., Chan, C. and Tolley, M.T., 2021. Electronics-free pneumatic circuits for controlling soft-legged robots. Science Robotics, 6(51).

D. Drotman, P. E. Glick and M. T. Tolley,"Evolution of Gait Sequences for Soft Legged Robots", Soft Robotics *In Preparation*

P. E. Glick, D. Drotman, D. Ruffatto and M. T. Tolley, "High Strength Inflatable Pouch Anchors," in IEEE Robotics and Automation Letters, vol. 5, no. 3, pp. 3761-3767, July 2020, doi: 10.1109/LRA.2020.2982069.

Ishida, M., Drotman, D., Shih, B., Hermes, M., Luhar, M. and Tolley, M.T., 2019. Morphing structure for changing hydrodynamic characteristics of a soft underwater walking robot. IEEE Robotics and Automation Letters, 4(4), pp.4163-4169.

Drotman, D., Ishida, M., Jadhav, S. and Tolley, M.T., 2018. Application-driven design of soft, 3-D printed, pneumatic actuators with bellows. IEEE/ASME Transactions on Mechatronics, 24(1), pp.78-87.

Kalisky, T., Wang, Y., Shih, B., Drotman, D., Jadhav, S., Aronoff-Spencer, E. and Tolley, M.T., 2017, September. Differential pressure control of 3D printed soft fluidic actuators. In 2017 IEEE/RSJ International Conference on Intelligent Robots and Systems (IROS) (pp. 6207-6213). IEEE.

Shih, B., Drotman, D., Christianson, C., Huo, Z., White, R., Christensen, H.I. and Tolley, M.T., 2017, September. Custom soft robotic gripper sensor skins for haptic object visualization. In 2017 IEEE/RSJ international conference on intelligent robots and systems (IROS) (pp. 494-501). IEEE.

Drotman, D., Jadhav, S., Karimi, M., de Zonia, P. and Tolley, M.T., 2017, May. 3D printed soft actuators for a legged robot capable of navigating unstructured terrain. In 2017 IEEE International Conference on Robotics and Automation (ICRA) (pp. 5532-5538). IEEE.

ABSTRACT OF THE DISSERTATION

Simplifying Terrain Navigation with Soft Legs

by

Dylan Drotman

Doctor of Philosophy in Engineering Sciences (Mechanical Engineering)

University of California San Diego, 2021

Professor Michael T. Tolley, Chair

Traditional robots, such as robotic arms in assembly lines, are designed for specialized, repeatable tasks. However, robotic applications are not always set in structured environments. Rather than using rigid components, soft robots made from soft materials are able to bend, extend, and deform. These movements enable soft robots to swim, walk, crawl, and grasp objects like the impressive capabilities of biological systems, such as the octopus. I hypothesized that the ability of soft legs to easily compress and bend would reduce the complexity of the control algorithms and hardware required for navigating unstructured obstacles. However, because soft walking robots move very differently than their rigid counterparts, they provide a new challenge. Soft appendages must be soft enough to passively adapt to the environment while being stiff enough

to generate forces for walking.

In this thesis, I have investigated methods to design, fabricate, model, and control soft-legged robots that are able to navigate over obstacles using simple control strategies. Inspired by nature, I found that a pneumatically actuated soft-legged quadruped robot with three actuated degrees-of-freedom (DoF) per leg was able to navigate over loose rocks or pebbles, squeeze into tight spaces, and walk underwater against flow when augmented with an inflatable soft body. I developed an application-driven design framework to relate the geometry and material properties of the soft legs to common metrics such as bend angle and blocked force. This design framework enables roboticists to rapidly design and fabricate soft robots to satisfy functional requirements. I also developed a lumped-parameter soft robot simulator to replicate the movement of the robot and used genetic algorithms to evolve practical, task-driven control strategies for accomplishing challenging problems, such as squeezing through a confined opening. Practical implementation of these gaits normally requires heavy and bulky pumps and valves which can be very challenging to carry onboard a robot with soft legs. To address this concern, I developed soft air-powered circuits to control the gait of the soft-legged robot without requiring any electronic components. The sequential behaviors were mechanically "programmed" in the circuit by storing information using the snap-through instability in hemispherical elastomeric membranes. The pneumatic memory elements in the circuits changed the walking direction of the robot based on physical interactions with the world. These pneumatic circuits could potentially be used to control electronics-free soft robots for navigating environments where electronics may not be suitable, such as environments sensitive to spark ignition. The contributions in this dissertation enable more versatile soft robotic systems which could potentially be used to monitor hazardous environments.

Chapter 1

Introduction

1.1 The Field of Soft Robotics

The impressive capabilities of biological systems have been used as inspiration for developing soft robots. The octopus, for instance, is able to squeeze its appendages and body through extremely small openings because of its lack of an internal skeleton. The design of these creatures can help engineers design robots that can navigate over obstacles or through cluttered environments. The field of bioinspired soft robotics has grown significantly, resulting in soft robotic systems with animal-like behaviors including swimming [1], jumping [2], and crawling [3].

In contrast to rigid robots, soft robots made from soft materials are highly dexterous and able to reach into inaccessible locations by bending, extending, or deforming. Soft robots have infinite passive degrees-of-freedom (DoF) compared to the finite passive DoFs on their rigid counterparts. Soft robots can safely adapt to their surroundings which can be used for grasping fragile objects and human-robot interactions. Soft robotic designs have previously been used for applications that rigid robots were not well-suited for, including wearable systems [4], haptic devices [5], and surgical devices [6].

1.2 Legged Locomotion

From a historical perspective, robotic locomotion became a topic of interest in the 1940's because of the potential use cases for the US military and space exploration [7]. Rigid legs require many joints and corresponding actuators to achieve complex motions required for navigating different environments. Soft robotic limbs, on the other hand, are an attractive option for legged locomotion over uneven terrain because compliant materials can passively conform to their surroundings. In addition, soft robots can squeeze into tight spaces to explore environments that are inaccessible to rigid systems. The challenge with designing soft robots is to balance strength and compliance; soft walking robots need to be soft to adapt to their environment while being strong enough to carry payloads and generate forces required for locomotion.

Traditional legged robots require direct drive motors or geared transmissions that drive each DoF. As robots become more complex with more controlled degrees of freedom, they require more motors. As a point of comparison, there are over 600 muscles that control the movement of a human body [8]. Embedding 600 motors into mobile robots would be expensive and unwieldy using current actuator technologies. Alternative fabrication techniques such as multi-material 3D printing and soft lithography can help to conserve space by embedding actuators into the structure of the robot. The hardware limitations and mechanical design of current rigid robots limit their potential to generate movements similar to biological systems.

The culmination of the work presented in this dissertation provide the tools necessary to design and control pneumatically actuated soft walking robots. The actuators are embedded into the structure which reduces the algorithmic and mechanical complexity required for controlling soft robots.

1.3 Thesis Outline and Contributions

The chapters and contributions from each chapter are as follows:

Chapter 1: Introduction

- This chapter introduces soft robotics as a field and highlights key background information that is relevant to the work in this thesis.

Chapter 2: Application-Driven Design Framework

- We developed an application-driven design framework for modeling multi degree-of-freedom (DoF) actuators with bellows.
- We used these soft actuators for three different soft robotic applications:
    1. Legs on a 3D printed soft walking robot capable of navigating over natural terrain
    2. Fingers on a soft robotic gripper capable of rotating a fragile light bulb
    3. Robot arm with a suction end effector for manipulating objects

Chapter 3: Gait Optimization for a Soft Legged Robot

- We developed a lumped-parameter model for the soft legs and designed a soft robot simulator to replicate the movement of the soft-legged quadrupedal robot interacting with obstacles.
- We used genetic algorithms to evolve the simulation to generate new gait sequences.
- The evolved gaits enabled the robot to walk faster on flat ground and navigate through an obstacle that was previously impossible using heuristic control strategies.

Chapter 4: Pneumatic Circuits for Controlling the Gaits of Soft Legged Robots

- We designed pneumatic circuits to control the gait of a walking robot without any electronics.
- We developed a new soft valve that enabled the circuits to control the omnidirectional movement of the robot based on interactions with the environment.

Chapter 2

Application-Driven Design of Soft, 3D Printed, Pneumatic Actuators with Bellows

2.1 Introduction

As robotic systems become increasingly integrated into our daily lives, there is a growing need for robots that can safely work and interact with humans. The development of new materials and advanced manufacturing techniques has led to an interest in robotic systems made of soft materials. In contrast to rigid robots, soft robots have intrinsically soft and extensible bodies capable of absorbing impact from collisions [2]. Soft robots deform continuously along their bodies (as opposed to rotating about discrete joints), enabling them to change their shape safely when interacting with humans or obstacles in dynamic environments.

Nature provides inspiration for designing soft machines. Muscular hydrostats (e.g. the octopus tentacle) conform to objects in their surroundings through a combination of active motion and passive deformation. The motions of these appendages enable the animals to manipulate objects and navigate complex environments. Cephalopods can grasp objects, swim, and navigate the sea floor by contracting muscle fibers arranged along their soft tentacles [9]. Inspired by

these natural examples, researchers have sought to develop tentacle-like soft robots with actuated motion similar to the octopus [10, 11].

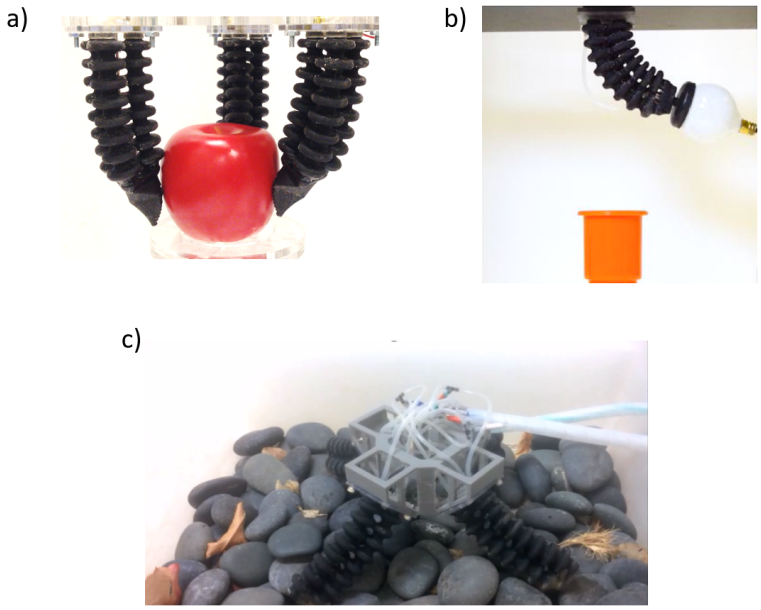

Figure 2.1: Soft robotic application for a 3D printed bending actuator module. a) Soft manipulator capable of rotating objects. b) Soft manipulator with a suction end effector [12]. c) Soft quadruped robot walking over rocky terrain [13].

Soft robots operate by actuating a deformable, soft structure to achieve controlled motion. Traditional actuators are constrained to linear or rotary motion while soft actuators are able to deform and adapt to objects in their environments with theoretically infinite degrees of freedom. Soft robots are generally controlled using pneumatic [14], hydraulic [15], or electrically actuated systems [16, 17].

Soft pneumatic actuators operate by applying positive or negative controlled input pressure to a hollow space inside a soft body. These actuators bend, twist, extend, or contract depending on the geometric or material asymmetries [18–20]. While many types of soft pneumatic actuators exist, they can be broadly organized into three categories: 1) McKibben actuators, 2) fiber reinforced actuators (FRAs), and 3) pneumatic networks (Pneunets). McKibben actuators have a meshed sleeve wrapped around a flexible membrane to create a contractile actuator [21, 22]. Fiber reinforced actuators use fibers to restrict motion of a pneumatic chamber causing the actuator to

move in a controlled direction depending on the fiber wrapping and fiber angle [23, 24]. Pneunets create a bending motion by using an inextensible strain limiting layer under a pneumatic network of air chambers [25]. These actuators are used for a wide range of applications such as a wearable device [4], a swimming robot [1], and a walking robot [3].

Soft robots have previously been fabricated using laborious molding processes [18, 26, 27]. These molding processes are limited when designing complicated actuator morphologies. Recent innovations in 3D printing have enabled the rapid fabrication of highly customizable, flexible, soft actuators. However, the materials available on commercial 3D printers often do not replicate the material properties (e.g. elasticity and strain-to-failure) of silicone rubbers traditionally used for soft actuators. Previous work has sought to address this challenge by developing custom 3D printers to print with a range of materials [28–31], although these systems do not yet have the precision and resolution of commercial systems.

3D printing has become a key technology for advancing the emerging field of soft robotics. Soft actuator designs can more closely resemble their bioinspired counterparts due to recent advances in 3D printing [32]. 3D printing enables researchers to rapidly fabricate new custom designs for soft actuators and sensors including 3D printed elastomeric actuators [33], integrated 3D printed actuators and sensors [34], and edible actuators [35]. 3D printing has enabled advances in the designs of soft robots actuated with smart materials such as dielectric elastomer actuators (DEAs) [36] and liquid-crystal elastomer actuators (LCEs) [37].

We, and others, have taken advantage of the capability of 3D printers to produce complex geometries with little to no extra cost [38]. Commercially available multi-material 3D printers are capable of printing mixtures of a rubbery and rigid material, greatly expanding the capabilities of directly manufacturing fully functional soft robots. We have designed soft components with a combination of intrinsic and extrinsic compliance sufficient to allow large, repeatable deformations. We have recently demonstrated the benefits of using multi-material 3D printing to fabricate a jumping soft robot powered by combustion [2] and an end effector inspired by a

squid sucker [39]. In this work, we designed the soft actuators manufactured on multi-material 3D printers that use the Polyjet technology (i.e. Connex printers by Stratasys), one of the few commercially available multi-material 3D printers. However, we hope that the general approach (as described in Section III) would be equally applicable to the design of soft robots manufactured using a variety of 3D printers.

A soft robotic application, such as locomotion, may require a specific actuator geometry (e.g. overall length or actuator diameter) or a specific actuation metric (e.g. blocked force or displacement). It is challenging to make early design decisions to satisfy application constraints due to the coupling between the effects of various design parameters (e.g. actuation method, material, actuator geometry) on the performance of a soft robot. Thus, a systematic approach is needed for the design of soft robots.

In this paper, we create a design framework to predict application-based metrics for a soft, 3D printable bending actuator with bellows. This design approach limits the design-iteration cycle time by relating the geometric parameters of the actuators to application-oriented metrics such as bend angle and blocked force. In Section II, we describe the design of the soft actuators. The models for the soft actuator are detailed in Section III. In Section IV, we describe the fabrication process. In Section V, we validate the forward kinematic model with experiments. We also tested the repeatability of the actuator chamber in bending by cyclically pressurizing an actuator chamber. In Section VI, we perform a sensitivity analysis on the geometric parameters of the bellows and compare the predictions of the model in response to varying key design parameters to experiments for a few actuator designs. In Section VII, we discuss how these bending actuator modules are used as legs for a soft quadruped robot. In Section VIII and IX, we discuss our findings and conclude this paper.

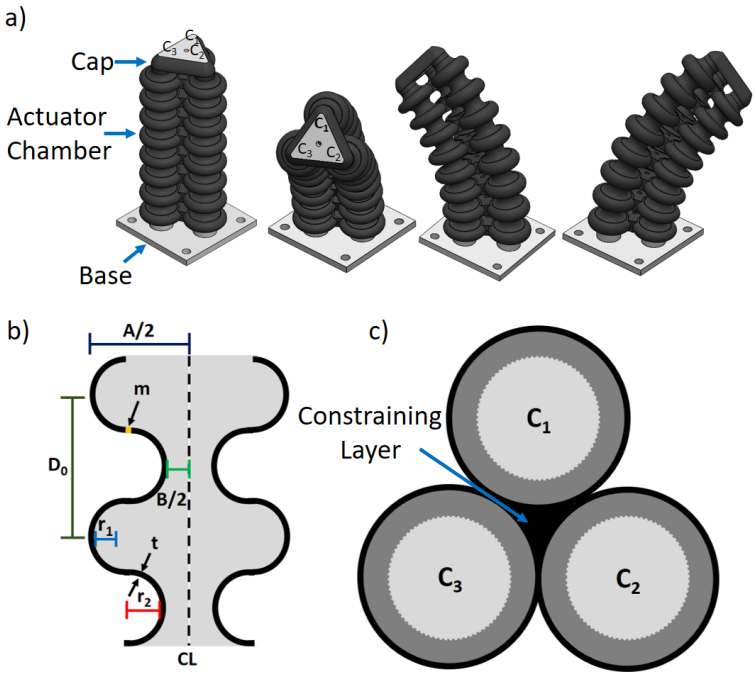

Figure 2.2: Actuation and geometry of a 3D printed soft actuator. a) Demonstrating the motion of an actuator from an uninflated state, to three inflated states by pressurizing chamber C_1, chamber C_2, and chamber C_3 respectively. b) Vertical cross-section of a single chamber of the bellows in the uninflated state. The vertical dashed line represents the center line of a single actuator chamber. The shaded region represents the inside of the chamber. c) Top perspective of the soft actuator. Each actuator contains three pneumatic chambers which are pressurized independently. The dark grey region represents the overlapping internal geometry of the bellows.

2.2 Actuator Design

3D printing actuators allows designers to create complex actuator designs that are difficult to fabricate using soft lithography or other molding techniques. We designed a 3D printed actuator capable of bending and extending about two axes (Figure 2.2a). These modular actuators are composed of three parallel, connected chambers rotated 120 degrees about the longitudinal axis of the actuator (Figure 2.2c). A rigid cap at the tip of the actuator module seals the three chambers. When each chamber is pressurized, the actuator module bends. The actuator module is connected to a rigid mounting plate at the base for interfacing with rigid components. In principle, this base could also be soft.

Each of the chambers of the actuator module can be pressurized with positive or negative

gauge pressure. When an actuator chamber is pressurized, the actuator bends in the direction away from the inflated chamber. If the actuator chamber is actuated with negative gauge pressure, the actuator bends towards the actuated chamber. In this work, we used a volumetric control system that can achieve both positive and negative gauge pressure [12].

2.3 Modeling

The extension, bending, and blocked force of the soft actuators at a constant pressure are affected by the geometry of the bellows and material properties. In this section, we model the motion of the actuators in 3D space and quantify how the performance of the actuators is affected by changing the geometry of the bellows.

Each actuator chamber has bellows allowing the actuator to extend, compress, and bend much more compared to cylindrical tubes of the same material. The bellows unfold and fold when the chambers are actuated with air or water. The geometry of the bellows is related to the initial length of the chamber of an actuator module in the uninflated state l_0 [40] (Figure 2.2b).

$$D_0 = 2(r_2 + r_1 + t) \tag{2.1}$$

$$l_0 = nD_0 \tag{2.2}$$

$$\frac{A}{2} = \frac{B}{2} + 2t + r_1 + r_2 + m \tag{2.3}$$

where D_0 is the distance from one of the bellows to the next for an actuator chamber, n is the number of bellows, r_1 is the inner radius of one of the bellows, r_2 is the outer radius of one of the bellows, t is the thickness of the wall of the bellows, m is the flat portion of the bellows, $\frac{A}{2}$ is the outer radius of the actuator, and $\frac{B}{2}$ is the inner radius of the actuator.

The kinematics of rigid robots are defined based on the displacement of each joint angle and the dimensions of each linkage. Soft continuously deformable actuators are more difficult to

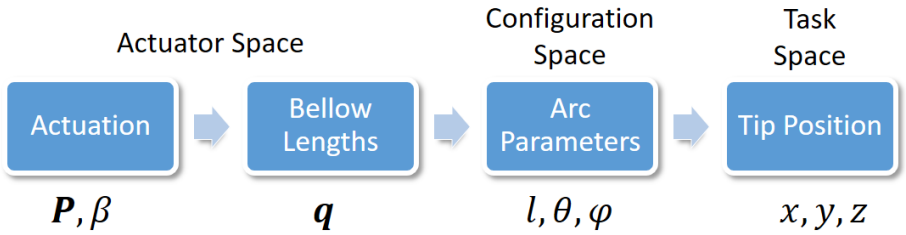

Figure 2.3: The actuator space is the space that represents actuator-specific characteristics (e.g. the material of the actuator and the geometry of the bellows) and how the chambers of the actuator change length depending on the input pressure. The actuator space is mapped to the configuration space and to the final task space for the position of the end of the actuator in Cartesian coordinates.

model compared to rigid linkages. An analytically tractable approach is to make the simplifying assumption that the actuator forms constant-curvature arcs [41]. We modeled the kinematics for the actuator in the actuator space, configuration space, and task space (Figure 2.3).

2.3.1 Forward Kinematics

The actuator space relates the pressure, geometry of the bellows, and material properties of the actuator to the length of the three chambers of the actuator. The actuator space, $\mathbf{q}$, is defined by the lengths of the three chambers l_i when $i = 1$,2, or 3.

$$\mathbf{q} = [l_1, l_2, l_3]^T \tag{2.4}$$

When an actuator chamber is actuated with positive or negative gauge pressure, the bellows extend or contract, changing the overall length of the chamber. The deflection of the chamber is modeled using elemental load cases applied to a half-convolution of one of the bellows [42, 43]. This model has been extended from [42] to account for a variation between the radius r_1 and r_2 by approximating the actuator stiffness for the two different radii as springs in series.

Assuming the axial stiffness is similar in extension and compression, the stiffness k_i of chamber i is:

$$k_i = \frac{1}{2n(\beta_1 + \beta_2)} \tag{2.5}$$

$$\beta_j = \frac{6\pi r_j^3 + 24mr_j^2 + m^3 + 3m^2 r_j \pi (1 + \frac{t^2}{12r_j^2})}{24EI} \tag{2.6}$$

where β_j is a geometric parameter related to the material and geometry of the bellows defined in Figure 2.2b, I is the averaged area moment of inertia of the chamber, E is the elastic modulus of the material and r_j is the radius of the bellows for the convex ($j = 1$) and concave and ($j = 2$) portions of the bellows. For non-negligible wall thickness ($t > \frac{r_j}{10}$), use $r_j + \frac{t}{2}$ instead of r_j. This assumption holds for applications where the actuator walls are thicker relative to the geometry of the bellows.

The change in length of an individual bellows chamber Δl_i^e due to its internal pressure P_i is determined from:

$$\Delta l_i^e = \frac{P_i A_p}{k_i} \tag{2.7}$$

$$l_i^e = \Delta l_i^e + l_0 \tag{2.8}$$

where l_i^e is the extended actuator chamber length for chamber i, A_p is the averaged cross-sectional area of a bellows chamber, and k_i is the stiffness of an an actuator chamber, given by Equation 2.5.

The three actuator chambers are connected by multiple constraining layers positioned in the center of the actuator along the length of the actuator (Figure 2.2c). These layers connect each of the bellows from one chamber to the two adjacent chambers, which is important for preventing buckling. However, this support structure also diminishes the extension of each actuator chamber. We account for this effect by defining the length of the actuator chamber including effects of the

constraining layers as:

$$\eta = \frac{l_i^e}{l_0} \tag{2.9}$$

$$l_i^c = \eta(l_0 - \gamma 2n(r_1 + t)) + \gamma 2n(r_1 + t) \tag{2.10}$$

$$l_i = \alpha l_i^c + (1 - \alpha) l_i^e \tag{2.11}$$

where η is the ratio of actuator extension to actuator chamber nominal length l_0, l_i^c is the constrained length of chamber i, l_i^e is the fully extended length of chamber i (unconstrained), and l_i is the final length of chamber i. The parameter γ specifies the percentage of the height of the bellows ($2n(r_1 + t)$) that is connected to the constraining layer. The coefficient α specifies the portion of the circumference of the bellows connected to the constraining layer. For our prototypical design, the constraining layers constrain the entire height of each of the bellows ($\gamma = 1$) and a third of their circumference ($\alpha = 1/3$).

The configuration space of the actuator is determined based on the constrained length of each actuator chamber, l_1, l_2, and l_3. The position of the actuator is defined based on the centerline of the actuator relative to each of three pneumatic chambers [41] (Figure 2.4).

$$l(\mathbf{q}) = \frac{1}{3}(l_1 + l_2 + l_3) \tag{2.12}$$

$$\phi(\mathbf{q}) = \tan^{-1}\left(\frac{\sqrt{3}(l_2 + l_3 - 2l_1)}{3(l_2 - l_3)}\right) \tag{2.13}$$

$$\kappa(\mathbf{q}) = \frac{2\sqrt{l_1^2 + l_2^2 + l_3^2 - l_1 l_2 - l_1 l_3 - l_2 l_3}}{d(l_1 + l_2 + l_3)} \tag{2.14}$$

$$\theta(\mathbf{q}) = l(\mathbf{q})\kappa(\mathbf{q}) \tag{2.15}$$

where l is the length of the centerline of the actuator, d is the distance between the center of the actuator and the center of each pneumatic chamber, κ is the curvature of the actuator, and ϕ is the angle of the actuator in the x-y plane.

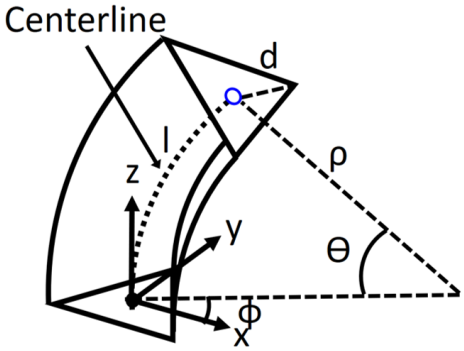

Figure 2.4: The three chambers of the actuator bend forming a constant curvature arc when one of the chambers is actuated. The position of the tip of the actuator is determined based on the deflection of the centerline.

The actuator's configuration space is then mapped to the task space of the actuator. This space represents the Cartesian coordinates of the distal end of the actuator.

$$c = 2\rho \sin\left(\frac{\theta}{2}\right) \tag{2.16}$$

$$x = c \sin\left(\frac{\theta}{2}\right) \cos(\phi) \tag{2.17}$$

$$y = c \sin\left(\frac{\theta}{2}\right) \sin(\phi) \tag{2.18}$$

$$z = c \cos\left(\frac{\theta}{2}\right) \tag{2.19}$$

where c is the chord length of the actuator, ρ is the radius of the actuator ($\rho = \frac{1}{\kappa}$), and x, y, and z are the x-coordinate, y-coordinate, and z-coordinate at the tip of the actuator.

2.3.2 Inverse Kinematics

The inverse kinematics are used to find the chamber lengths associated with a desired tip position of the actuator. The actuator configuration is unique when the base of the constant-curvature arc is normal to the plane it is attached to.

To solve the inverse kinematics, we relate the individual lengths of the actuator chambers

to the centerline of the actuator [44].

$$\phi = \tan^{-1}\left(\frac{y}{x}\right) \tag{2.20}$$

$$\kappa = \frac{2\sqrt{x^2+y^2}}{x^2+y^2+z^2} \tag{2.21}$$

$$\theta = \begin{cases} \cos^{-1}(1-\kappa\sqrt{x^2+y^2}) & \text{if } z > 0 \\ 2\pi - \cos^{-1}(1-\kappa\sqrt{x^2+y^2}) & \text{if } z \leq 0 \end{cases} \tag{2.22}$$

$$l = \frac{\theta}{\kappa} \tag{2.23}$$

The lengths of each individual chamber are then mapped to the position of the actuator in 3D space.

$$l_i = l - \theta d \cos\left(\frac{2\pi}{3}(i-1) + \frac{\pi}{2} - \phi\right) \tag{2.24}$$

where d is the distance from the actuator center to the center of each actuator chamber. By combining Equations 2.9, 2.10, and 2.11, we define the length and pressures for each chamber.

$$l_i^e = \frac{l_0(l_i - \alpha\gamma 2n(r_1+t))}{l_0 - \alpha\gamma 2n(r_1+t)} \tag{2.25}$$

$$P_i = \frac{(l_i^e - l_0)k_i}{A} \tag{2.26}$$

2.3.3 Blocked Force

We used Castigliano's method to derive an expression for the blocked force for a soft actuator by representing the actuator module as a curved beam (see Supplemental Info)

$$F_y^A = \frac{E_{eff} I(\rho(1-\cos(\theta)) - h_F)}{\rho^3\left(\frac{1}{2}\theta - \frac{1}{2}\sin(\theta)\cos(\theta)\right)} \tag{2.27}$$

$$E_{eff} = \frac{l}{A_0}\sum_{i=1}^{3} k_i \tag{2.28}$$

where F_y^A is the force from the bending actuator, E_{eff} is the effective Young's modulus of the actuator when pressurized, A_0 is the cross-sectional area of the three-chambered actuator, h_F is the height of the actuator off the ground, and k_i is the stiffness of actuator chamber i. The stiffness of the actuator depends on the input pressure to the actuator chambers, the geometry of the bellows, and the stiffness of the material. The stiffness of the actuator can also be resolved experimentally or by using finite element analysis (FEA). The stiffness of an actuator module used as the leg of a soft quadruped was determined using FEA [13] (see Supplemental Info).

2.4 Fabrication

We used a commercial multi-material 3D printer (Connex 3, Stratasys Inc.) to print the actuator modules. This printer mixes rubbery material with rigid material to create materials with a range of stiffnesses which can be represented on the Shore A scale from 35A-95A. We can tune the Shore value by changing the percentages of the rigid and soft materials. This printer provides a larger range of material stiffness choices compared to alternative FDM 3D printers that have limited options for flexible materials (e.g. NinjaFlex, thermoplastic polyurethane).

The material used for the actuator module is a mixture of commercially 3D printed, photocurable elastomer (Tango+ or Tangoblack+) and a hard plastic (VeroClear). We have used both black and translucent materials (Tangoblack+ and Tango+ respectively) for our actuators which have similar material properties. We chose a mixture of material that results in a Shore hardness value of 70A as a compromise between compliance and stiffness. We printed these actuators with a rigid base plate for mounting. The base plate and rigid cap are made of the same

hard plastic (VeroClear).

The multi-material 3D printer fills the internal volume of the actuator chambers with support material during the printing process to prevent parts from collapsing that have large, overhanging features. An alternative approach is to modify the 3D printer to print pre-filled fluidic channels [31]. The base plate and the actuator are printed as one part and the cap is printed separately to allow for the removal of support material from the actuator chambers. This support material can be difficult to clean when designing complex components.

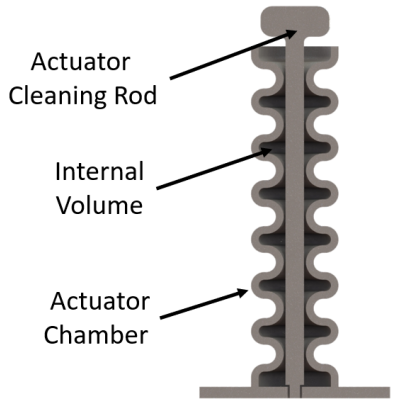

Figure 2.5: Cross-section view of one of the actuator chambers to show the placement of the rigid rods in the center of an actuator chamber.

To remove support material from the soft actuators, we used the chemical soaking approach recommended by Stratasys for their desolvable SUP706 support material (i.e. soaking printed parts in a solution of 2% sodium hydroxide and 1% sodium metasilicate with agitation). However, after this process, support material still remained in confined concave areas (i.e. inside the bellows). Therefore, we used high pressure water/air to remove any remaining support material.

We decided to use high pressure air/water to remove support material. However, high pressure water/air can cause ruptures in the actuators if the support material clogs the chambers during cleaning. To solve this problem, we 3D printed rods along the length of the internal cavity of the chambers of the bellows in place of the support material (Figure 2.5). The 3D printed rods are removed after the printing process has completed, which makes the cleaning process

much quicker. The cleaning rods can also have bellows to fill the internal cavity of the actuator chambers, but this type of cleaning rod is much more difficult to remove. Air and water are used to remove the remaining support material once the rods have been removed.

2.5 Experimental Testing

To demonstrate the versatility of the models, the tip position of the actuator was measured when the actuator chambers were pressurized within the operating pressure bounds. When all three chambers are inflated equally, the actuator extends axially. In all other cases, the actuator bends. The outer profile of the actuator workspace in the XY plane and XZ plane are shown in Figure 2.6. Figure 2.6a shows a top view while Figure 2.6b shows a side view (Plane 1). The experimental results were compared to the analytical model (Figure 2.6b).

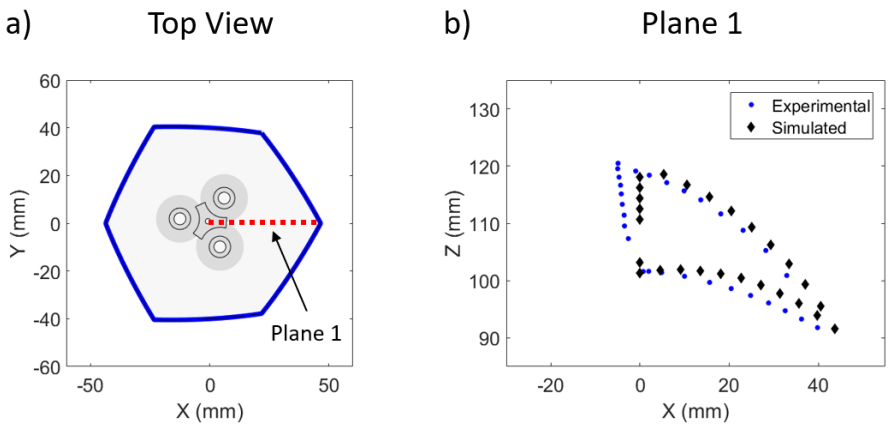

Figure 2.6: Motion capture data using a motion capture system for tracking the tip of the soft actuator extending and bending for varying input pressures. a) Top view of the actuator task space showing Plane 1 as a cross-section of the actuator task space (XY plane). The shaded area represents the actuator task space from a top projection. b) Experimental data for the bounds of the 3D task space when the actuator is bending in the XZ Plane (Plane 1). The actuator was inflated at varying positive pressure between 0 and 50 kPa at 5 kPa increments.

We actuated a single chamber of an actuator from 0 - 50kPa for 1000 cycles ($\sim$ 5 hours of data) and recorded the position of the tip of the actuator using our motion capture system (sampled at 120Hz) (Figure 2.7). The chamber was pressurized using our volumetric control

system [12] and controlled using PID (proportional–integral–derivative controller). The cycles were downsampled to 1Hz and overlapped. We chose the initial cycle to be the 10^{th} cycle instead of the 1^{st} cycle because it took a few cycles to reach a steady actuation cycle.

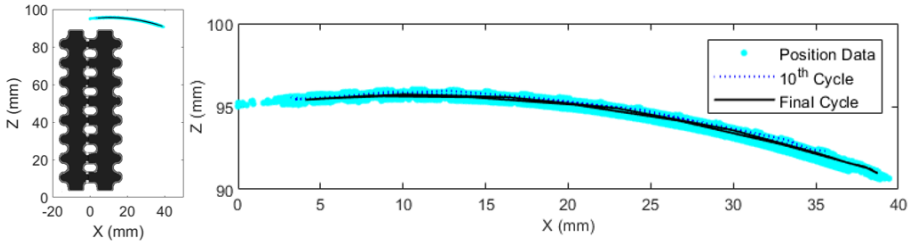

Figure 2.7: Position of the tip of the actuator when one actuator chamber is cyclically pressurized from 0-50kPa for 1000 cycles (∼5 hours of data). The 10^{th} and last cycle are emphasized in the dotted blue and solid black lines (respectively) and the cycles in between are shown in cyan. The trajectory is shown in a scaled image (left) and the zoomed in image (right). The actuator followed a similar path for all cycles, but the actuator extended further for the same pressure as the actuator cycles increased.

The actuator followed a repeatable path for all cycles and did not rupture during testing; however, the actuator extended further as the number of actuator cycles increased. The repeatability of the actuator depends on the choice for the the geometry of the bellows, input pressure, and material. The material changed stiffness slightly depending on the ambient temperature as reported previously [45].

We previously reported the max pressure for this actuator to be 105kPa when the layers of the actuator are printed along the width of the actuator [12]. We wanted to test whether print orientation had any affect on actuation so we tested the actuators to failure when pressurizing one chamber and compared results. We discovered that the actuator can handle up to 110kPa when printed with layers parallel to the bellows axis of rotation. Unless the geometry of the prints are close to the scale of the layer height (16 microns), there will be a minimal change in actuator performance. However, cleaning actuators near this scale would not be practical.

Table 2.1: Sensitivity values for geometric parameters of the bellows

	$\partial\theta$	$\partial F_\Gamma 30073^A$
$\partial r_\Gamma 29745$	4900	110
∂t	-6.8E-4	-1700
$\partial l_\Gamma 29744$	142	1.6
∂B	2.17E4	570
∂A	-4950	-66
$\partial \mathbf{n}$	6	0.144

2.6 Actuation Trends for Varying the Geometry of the Bellows

The models discussed in Section III relate the pressure in the actuator chamber and the geometry of the bellows to the position of the tip of the actuator and the blocked force of the actuator. By tuning the geometry of the bellows, robot designers can create soft robots that satisfy functional requirements.

There are many geometric parameters that can be tuned to adjust the motion of the bending actuator. We performed a sensitivity analysis to find which parameters have the greatest effect on bending and blocked force. We took the partial derivative of the analytical model for bend angle θ and output force F_y^A with respect to the geometric parameters r_1, t, B, l_0, n, and A. The results showed that the thickness of the material of the bellows t and the inner chamber diameter of the bellows B had the greatest effect on blocked force and bend angle. The sensitivity values (partial derivatives) are shown in Table 2.1.

Based on the results from the sensitivity analysis, we fabricated actuators with a $\pm 10\%$ percent variation of t and B. We compared these actuators to results from the analytical model (Figure 2.8).

The experimental data fits the model well despite model assumptions (linearly elastic material and constant curvature). As t gets smaller, the pressurized chamber strains the material

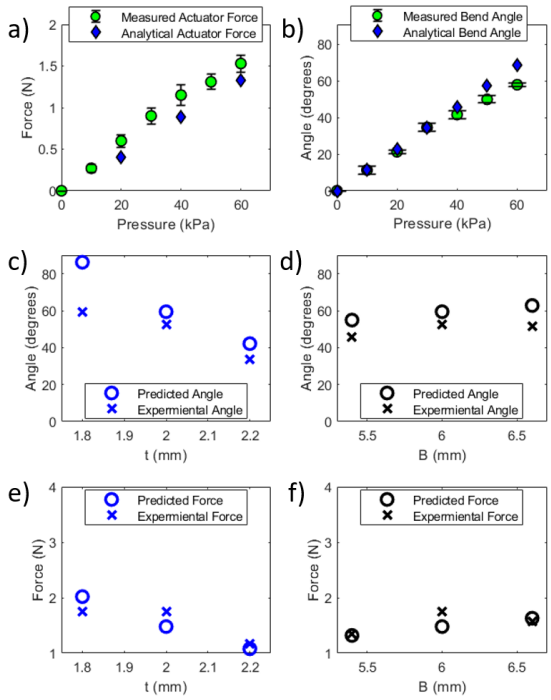

Figure 2.8: Comparing the actuator models to experimental results varying actuation pressure and varying the geometry of the actuator. Relationship between bend angle θ and force F_y^A to varying input pressures (Figures a-b) and to the two most sensitive geometric parameters of the bellows: wall thickness of the bellows t and the inner diameter of an actuator chamber B inflated at a constant pressure of 50kPa (Figures c-f).

more which causes the results to diverge from the model because of the linear elastic assumption.

There is a limitation on how thin the actuator walls can be due to the strength of the material used for the bellows. This thickness is dependent on the stress in the bellows when the chambers are actuated. The stress on the bellows over time can have an impact on the life span of the soft actuators. The max stress for an extending actuator chamber must be less than the yield strength of the material [42].

$$\sigma_{max} = \frac{3P_i A_p (A - B - t)}{2\pi t^2 (B + \frac{t}{2})}, \tag{2.29}$$

$$\sigma_{max} < \sigma_Y \tag{2.30}$$

2.7 Soft Robot Applications

The three-chambered 3D printed actuator analyzed in this paper can be used for a wide range of applications such as a finger for a soft gripper (Figure 2.1a), a soft arm capable of manipulating fragile objects (Figure 2.1b) [12], or a leg for a soft quadrupedal robot (Figure 2.1c) [13]. The geometry, material, and pressure can be tuned to develop actuators to fit the requirements needed for each application.

One can take advantage of this framework for practical soft robotic applications. The inverse kinematics are useful for fine positioning of the end effector of a bending module. For example, the soft arm pictured in Figure 2.1b is an example application that requires the actuator to be placed at specific positions to manipulate objects placed within the actuator workspace. The kinematics relationships provide the input pressures required to position the actuator. The force model is useful when determining what bellows geometry and pressure are required to meet application force requirements. For example, this model can be used to figure out how much weight a gripper can carry (Figure 2.1a). The sensitivity analysis described in Section VI can be used to determine which of the bellows geometric parameters need to be tuned to meet these functional requirements.

In the next section, we discuss the use of these actuators and legs for a quadruped robot.

2.7.1 Application Case Study: Soft Legs for a Quadruped Robot

Here we describe the use of the 3D printed soft actuators with bellows as the legs of a soft robot for passive adaptation to rough terrain.

Gait Model

The gait for a quadruped is defined by the common input pressure, the sequence of chamber inflation, and the duration of each inflation. Our goal is to compare the advantages of

various gaits on different terrain.

The dynamic pressure change in the chamber is modeled as a linear pneumatic RC circuit [46].

$$P(t) = (P_0 - P_{in})e^{-\frac{t}{R_{EQ}C_{EQ}}} + P_{in} \tag{2.31}$$

where P is the pressure in the actuated chamber, P_0 is the initial pressure, and P_{in} is the common input air pressure. The time constant $\tau = R_{EQ}C_{EQ}$ is a metric that tells how fast the actuators respond when pressurized where R_{EQ} is the resistance from the pneumatic valves and C_{EQ} is the capacitance from the actuator chambers. The capacitance from the tubing is neglected. Since the valves and the chambers of the quadruped are connected together in parallel, the equivalent resistance of the resulting system is the sum of the individual resistances while the reciprocal of the equivalent capacitance is the sum of the reciprocals of each capacitance.

This results in a model that predicts how quickly the robot reaches its pressure equilibrium. While R_{EQ} and C_{EQ} are difficult to determine individually, we identified the time constant τ by applying a step input in chamber pressure and observed the resulting motion (Figure 2.9).

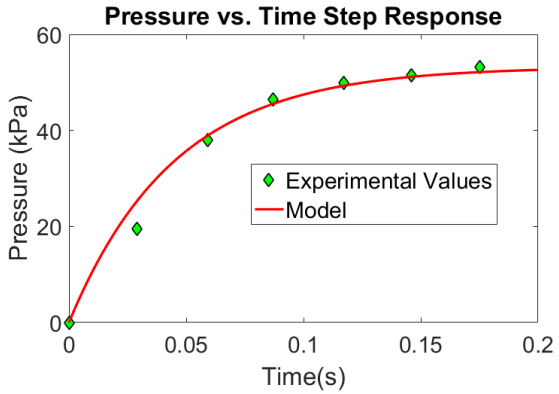

Figure 2.9: Pressure step response for bellowed actuator. The time constant for a single chamber at initial pressure P_0 = 0 kPa inflated with an input pressure of P_{in} = 50 kPa is τ = .045s. The response time to settle at the desired pressure is 0.2s.

The leg sequence chosen for this quadruped is a circular rotation counterclockwise or clockwise to lift the legs of the robot over obstacles. When the legs rotate, they push off the

ground creating a frictional force applied in the direction perpendicular to the orientation of the legs on the body. These circular rotation primitives are then sequenced for each of the legs. The bending direction of each leg is determined from a model of deflection and extension of soft actuators composed of three pneumatic tubes (Equation 2.13).

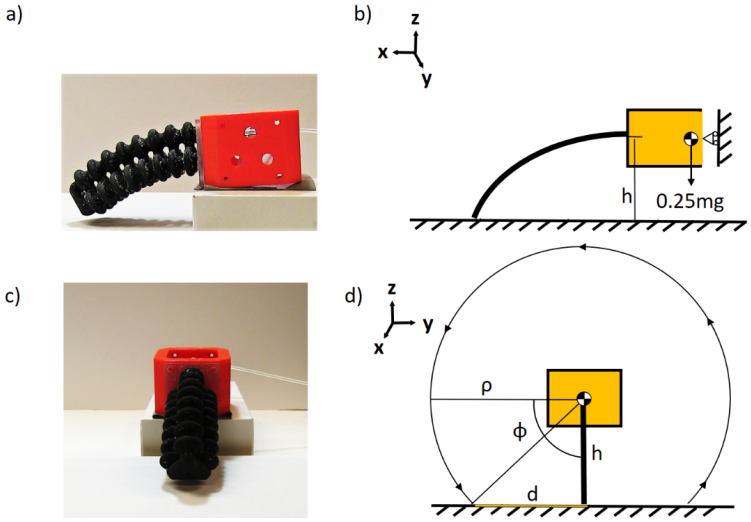

Figure 2.10: Locomotion of the quadrupedal robot. a) The height of the robot is determined by analyzing the deflection of a curved beam b) with an applied load. c) Side perspective of the quadruped in the inflated state. d) The soft limb creates a circle when the chambers are sequenced.

The weight of the robot body causes the base of each leg to deflect vertically (Figure 2.10a). Each leg is compliant with stiffness depending on the input pressure. We used Castigliano's method to calculate the vertical deflection of a soft leg assuming that the soft robotic leg is a curved beam fixed at the bottom and on a vertically constrained roller (Figure 2.10a)

$$\delta_y^A = \frac{\rho^3 mg}{4E_{eff}I}\left(\frac{1}{2}\theta - \frac{1}{2}\sin(\theta)\cos(\theta)\right) \tag{2.32}$$

$$h_F = H - \delta y^A = \rho(1-\cos(\theta)) - \delta y^A \tag{2.33}$$

where δ_y^A is the vertical deflection of the leg, h_F is the height off the ground after the applied load, H is the height before the applied load, ρ is the radius of the circular rotation when the leg

contacts a surface, g is gravitational acceleration, and m is the mass of the robot body.

The translational velocity of the robot is estimated based on the distance the leg contacts the ground assuming no slip (Figure 2.10b)

$$d = \sqrt{\rho^2 - h_F^2} \tag{2.34}$$

where d is half the distance the leg is in contact with the ground and h_F is the height of the robot off the ground. The velocity of each leg is determined based on one rotation of the leg

$$v_{leg} = \frac{\omega d}{\pi} \tag{2.35}$$

where ω is the rotational velocity of the leg. The pressure actuation time affects the rotational velocity of the leg.

Since each leg is oriented in the shape of an X, the velocity contribution to the robot is:

$$v_{robot} = \frac{\sqrt{2}}{2} v_{leg} = \frac{\sqrt{2}}{2} \frac{\omega d}{\pi} \tag{2.36}$$

This expression estimates how fast each leg moves through one cycle. The quadruped velocity is determined by combining the pressure response time with the estimate for the linear velocity.

Although one goal is rapid linear velocity, a competing goal is walking over obstacles. Three different gait sequences are defined to address these competing goals (Figure 2.11).

Quadruped Capabilities

The translational velocity of the robot was compared with different gait sequences, leg angles, and different terrain. The velocities were calculated as an average velocity for each condition using image processing. The results of these experiments are summarized in Figures

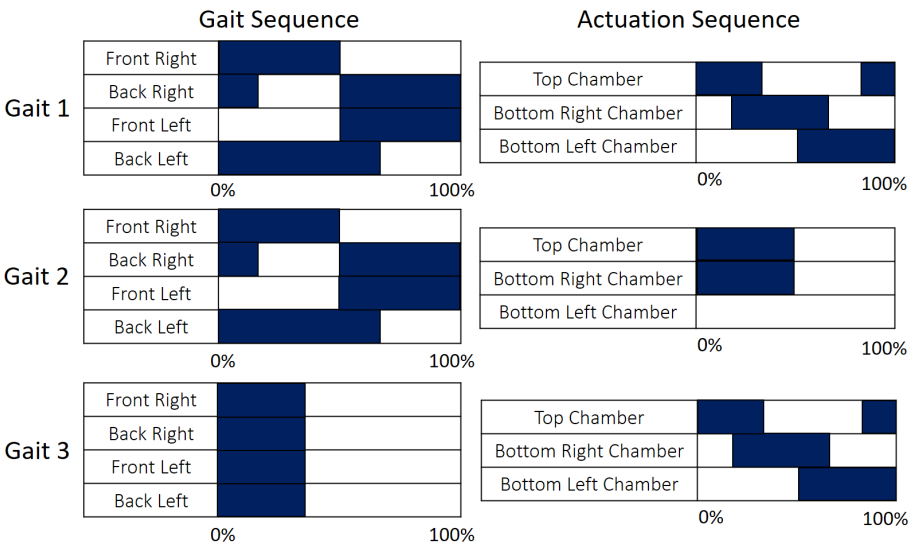

Figure 2.11: Actuation and gait sequences for one cycle of the quadrupedal robot gait. The shaded region for the gait sequences represents the time each leg contacts the ground. The chamber actuation sequence for all four limbs is next to the corresponding gait cycle. The shaded region in the chamber actuation sequences represents the time for which the chambers are inflated.

2.14a & 2.14b.

We control the soft quadruped robot using a modified version of an open-source control board [47]. This board controls the airflow through three to six independent solenoid valves (VQ100 Series, Steven Engineering) depending on the gait sequence. A common pressure regulator controls the input pressure P_{in} applied to each chamber. The controller (Mega 2560, Arduino) actuates the solenoid valves using ON-OFF control to achieve the gait sequences described above.

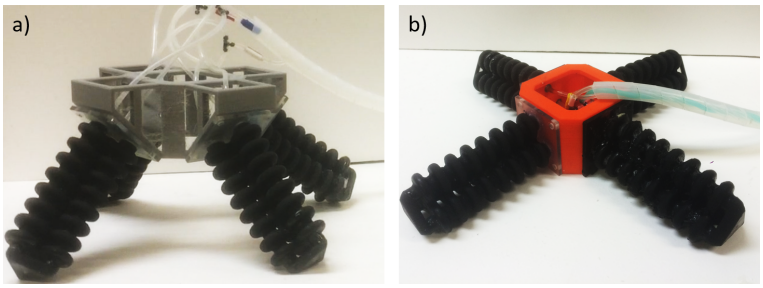

Figure 2.12: We compared the performance of two leg configurations for the quadrupedal robot. a) One configuration had an initial leg angle of 45 degrees, while b) the other robot had legs connected to the body horizontally.

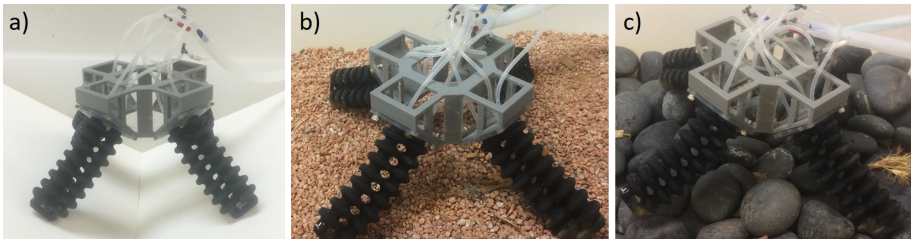

Figure 2.13: Locomotion of the quadrupedal robot. Angled quadruped demonstrating its ability to walk over a) a valley, b) small pebbles and c) large rocks.

We observed that *Gait 2* is the most effective gait for translational velocity on flat ground since it only requires two actuated chambers per gait cycle. However, this gait sequence is limited on rough terrain. By contrast, *Gait 1* and *Gait 3* were intentionally designed to lift the legs off the ground during the actuation sequence, resulting in improved speed over rough terrain.

Next we compared the two leg configurations (Figure 2.12). We found that the robot moved faster with angled legs compared to the flat configuration for each gait (Figure 2.14a). The angled legs support the weight of the robot at a lower moment arm and apply a larger traction force. For applications that require the robot to move through confined spaces, the flat configuration may provide more mobility.

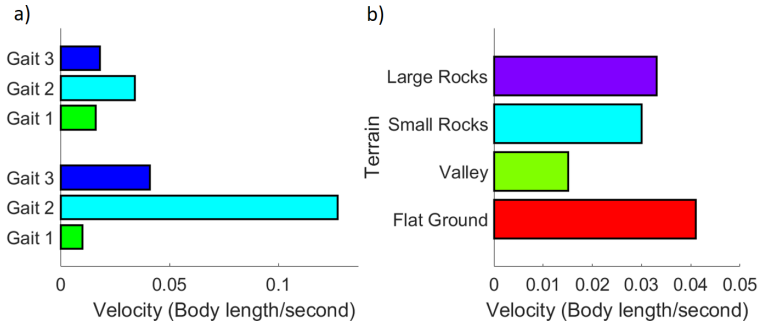

Figure 2.14: Velocity comparison for the quadruped a) Velocity of the robot compared to different leg angles and gait sequences on flat ground. b) Velocity of the robot on different terrain. The quadruped used for all four tests had angled legs and used *Gait 1*.

We concluded that an angled leg quadruped using *Gait 1* had the best performance on the largest variety of terrain. Thus, we tested the quadruped in this configuration over flat ground, pebbles, rocks, and over a valley (Figure 2.14b).

2.8 Discussion

The previous section showed how the 3D printed actuators with bellows presented in this paper can be used for a practical applications such as locomotion on rough terrain. However, the analytical model makes assumptions that will lead to errors in the force and deflection predictions when the assumptions do not hold. For example, since the model for bend angle is based on the deflection of one of the bellows, there will be an accumulation of error for actuators with large numbers of bellows. Therefore, the model for bend angle of the actuator is a better approximation if there are a lower number of bellows for each actuator chamber.

By modeling the actuator using a computational approach rather than an analytical expression, we can remove some of the assumptions that limit the accuracy of the model. FEA (finite element analysis) is commonly used for simulating the behavior of soft systems because it can account for the geometric and material nonlinearities in soft materials. Using FEA, there would also no longer be a constant-curvature assumption. However, FEA modeling is computationally intensive and specific to one geometry. Thus, an analytical expression for the behavior of the bellows enables roboticists to quickly make early design decisions for the entire class of 3D printable three-chamber actuators with bellows.

2.9 Conclusion

In this paper, we have described a framework for predicting the actuation characteristics of a three-chambered, 3D printed, soft actuator with bellows and related these actuation characteristics to the geometry of the bellows. By relating the geometry of the bellows to application-oriented metrics (e.g. bend angle and blocked force), designers can predict how their soft robot behaves before manufacturing it. These actuator models and multi-material 3D printing can greatly improve the versatility of practical soft robotic systems. This design framework enables roboticists to rapidly design and fabricate soft robots that satisfy functional requirements, opening up new

possibilities for how they approach designing soft machines.

The next steps would be to use a multivariable optimization method to tune the geometry of the bellows, material, and actuation pressure to satisfy robot constraints. The actuators in this work were tuned individually to demonstrate trends when parameters of the bellows were changed, but additional constraints may be required depending on the application. For example, an application may have both force and bending design requirements while needing a minimum stress in the actuator to ensure the actuator will have a long life-span.

2.10 Acknowledgement

This work is supported by the UC San Diego Frontiers of Innovation Scholarship Program (FISP) and the Office of Naval Research grant number N00014-17-1-2062. The authors would like to acknowledge Prof. Tom Bewley and the Coordinated Robotics Lab at UCSD for allowing us to use their Optitrack motion capture system.

Chapter 2 uses the material as it appears in the published paper in IEEE/ASME Transactions on Mechatronics 2018, D. Drotman, M. Ishida, S. Jadhav, M.T. Tolley "Application-Driven Design of Soft, 3-D Printed, Pneumatic Actuators With Bellows." The dissertation author was the first author and primary investigator of this material.

Chapter 3

Evolution of Gait Sequences for Soft Legged Robots

3.1 Introduction

Soft robots made from soft materials are highly dexterous and able to reach into inaccessible locations by bending, extending, or deforming. Researchers have previously built soft robots that are able to squeeze under obstacles [48], endure large impacts [3, 48, 49], and change shape [50, 51]. These capabilities are possible because soft robots are able to conform to their environment. Structural compliance reduces the algorithmic complexity required for navigating challenging environments [13, 52] which makes soft-legged robots an attractive option for locomotion.

Modeling soft robots is challenging because the designer must make assumptions to accurately describe the robot's behavior without making the simulation computationally expensive. Researchers have used voxelated soft robot simulations (i.e. robot simulations composed of many small, cubic blocks of a soft material) to generate new designs and actuation strategies [53–56]. The problem with using this approach is that voxelated robots model the internal volume of

the structure which does not significantly impact the gait of the robot. Efficient simulations are required to evaluate the robot's movement in different environments, especially for complex robots (i.e robots with a large number of active degrees of freedom, passive degrees of freedom and contacts with the environment). Computational modeling approaches are useful when representing intricate model interactions, however, these models are inefficient when solving system level problems such as gait discovery.

The Spring-Loaded Inverted Pendulum (SLIP) model [57] has been designed to simplify the movement of complex walking systems by using limited knowledge about the dynamics (i.e. the location of the center of mass and angular momentum) to replicate the movement of multi-legged biological and artificial creatures [58]. The problem is that the SLIP model abstracts away information that is necessary for a complete description of the dynamic movement of the robot. For example, the SLIP model does not take into account contact points along the legs and body and it does not include the swing phase of legs on multi-legged systems. The SLIP model lacks important information that is required for modeling and controlling multi-legged physical robots to navigate different environments.

Lumped parameter modeling is an effective approach for generating new behaviors on physical robots because it is analytically tractable and maintains model fidelity. For example, previous work modeled a soft inchworm robot as a multi-linked mechanism [59] which closely matched the movement of the physical robot for the normalized step size. Researchers used this simple model to find an optimal phase offset for the gait sequence of the robot. This demonstration showed that simple predictive lumped-parameter models can be used to design gait sequences for robotic systems without requiring excessive computational overhead.

Researchers in soft robotics have used splines [60], constant-curvature arcs [61], and rigid links [59, 62] to represent the movement of soft appendages. As the number of elements increases, the model becomes a closer representation of the deformable object. However, as the number of elements increases, the number of equations required to define the position of all element

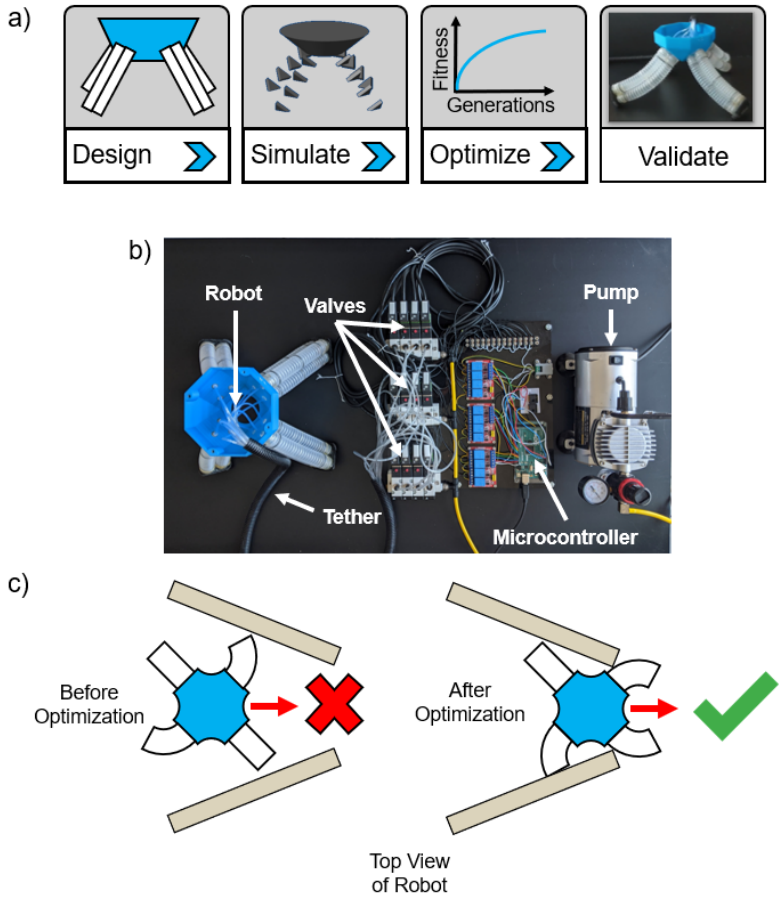

Figure 3.1: Gait optimization for a soft legged quadruped robot. a) Schematic of the workflow for optimizing gait sequences for a soft legged robot. b) Labeled image of pneumatic and electrical components required to control the walking robot. c) Schematic of the quadruped learning how to squeeze through an obstacle before and after the gait sequence has been evolved using a genetic algorithm.

increases (i.e. an equation for each element and the geometric constraints between neighboring elements). Lumped parameter models represent critical elements of inelastic and elastic bodies which are beneficial for designing soft robot simulators.

The manual design of soft robot controllers for walking robots is notoriously challenging. Experimental testing puts strain on the physical hardware which limits the number of gait evaluations. Researchers have used genetic algorithms since the early 1970's as a means of replicating the evolutionary process to design new robotic movements [63]. Genetic algorithms are designed to optimize traits loosely based on Darwin's principle of "survival of the fittest"

[63, 64]. Researchers have previously used genetic algorithms to evolve soft robots in simulation to squeeze through tight spaces [56] and navigate over aquatic and terrestrial environments [54]. Although these simulation results are impressive, limited research on evolving soft robots over challenging environments in simulation has transferred to hardware.

In this work, we simulated the movement of a soft-legged robot using a simplified lumped-parameter model and tuned essential gait parameters using genetic algorithms. In Section I, we discuss the design and simulation of the soft-legged quadruped robot. In Section II, we discuss how we validated the simulation with hardware. In Section III, we discuss how we optimized the gait sequence of the robot to walk faster on flat ground and squeeze through a confined opening.

3.2 Materials and Methods

3.2.1 Design of a Soft Legged Quadruped Robot

We designed a four-legged soft quadruped with three pneumatic chambers per leg. The design of the robot was similar to our previous work [13, 52] (Figure 3.3a). The legs of the robot were radially symmetric about the center of the body. Each limb was angled downward at a 45° angle relative to the horizontal, and composed of three parallel, connected pneumatic cylindrical chambers with bellows. When a chamber was pressurized, the limb bent towards the two uninflated chambers (Figure 3.3b). The three chambers of each limb provided the multi-axis bending required for walking. The bellows on each chamber reduced the resistance to bending when compared to simple tubes of the same material. Simple tubes can fatigue over time because of cyclic stretching and bending of the tube material.

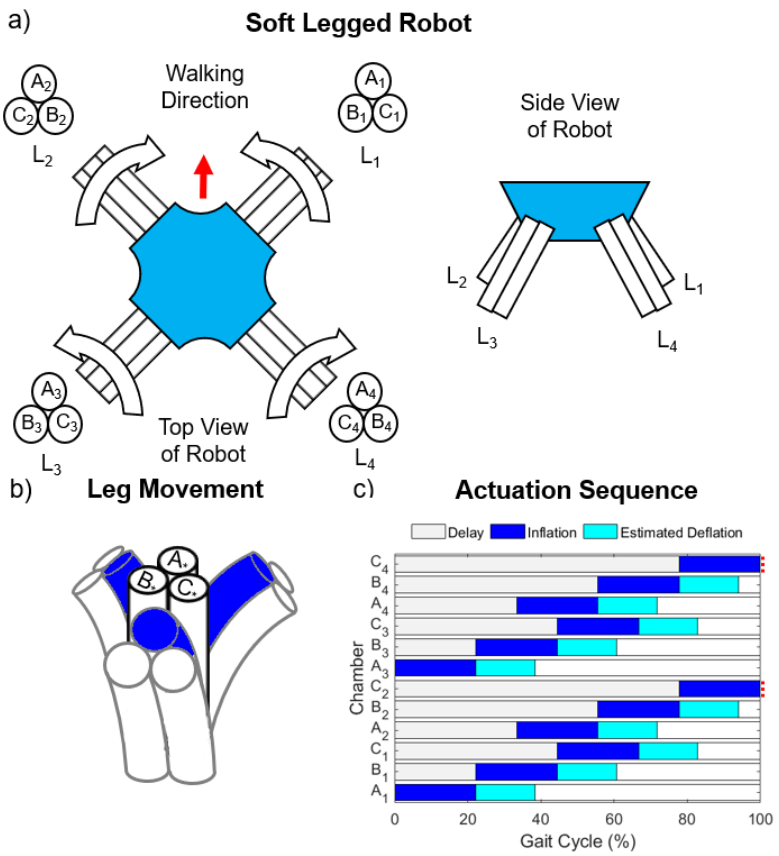

Figure 3.2: Labeled image describing the movement of the quadruped robot. a) The chambers on each leg are inflated in sequence which causes the robot to walk in a desired direction. b) When one chamber is inflated, the legs bend towards the other two uninflated chambers. c) Each chamber is then inflated in a sequence over the entire gait cycle. Each gait cycle is then repeated to produce movement. The delay and inflation time are directly programmed to produce this movement. The estimated deflation depicted in c) ends when pressure reaches 10kPa. The red dotted lines on the right indicates that the deflation stage for the corresponding chamber overlaps into the next gait cycle. The gait depicted in c) is labeled as the *Seed Gait*.

3.2.2 Design of the Gait Sequence

There are many possible gaits that can be used to solve navigation problems with the soft-legged robot. Each of the twelve chambers on the robot can be inflated and deflated in any order within the pressure limits of each chamber. Previously, we hand-tuned a diagonal couplet gait pattern which is similar to gaits observed in nature [13, 52]. This gait sequence was simple to implement because it only required a few valves (i.e. six valves instead of twelve valves) to control the robot. The robot was able to move forwards, backwards, sideways, and rotate in

place by using circular primitive movements. The direction of rotation of the legs determined the walking direction of the robot.

3.2.3 Soft Robot Simulator

Simulated environments can help to solve unexpected issues and lead to new qualitative and quantitative discoveries of successful gaits. Computationally efficient analytical models are useful for simulating the movement of walking robots. We developed simplified models to emulate the movement of the physical system without having to model the volumetric change that occurs when each chamber is inflated.

We previously predicted the tip position of the leg based on the arc lengths of each of the individual chambers [52]. We also showed that the length of the centerline of each leg was a function of the lengths of the individual chambers. In this work, we represented the flexible centerline as a combination of discretized elements to form a lumped mass-spring-damper model (Figure 3.3). Each leg was composed of translational spring-damper elements and rotational spring-damper elements. The lengths of the translational elements were described based on the chord lengths of each segmented arc along the centerline. Each linear segment had a mass that was a percentage of the total mass of the leg. The mass of the leg was equally distributed among each element. We assumed that all of the springs extended and bent the same amount when the chambers were pressurized. We also assumed that each mass-spring-damper element on each leg was spatially invariant. The stiffness and damping coefficients for each element on each leg depended on the pressure in the chambers of the corresponding leg. We used a weighted average of the pressure dynamic profile to estimate a constant stiffness and damping coefficient for each leg at different pressures (see Supplemental Materials). Four separate chains of elements representing four legs of the robot were attached to a rigid body to represent the soft walking robot.

Planar Bending Model

We identified the unknown leg parameters (i.e. stiffness and damping coefficients) based on the motion of one leg after one chamber was inflated. We assumed that the leg was radially symmetric about the central longitudinal axis (i.e. each chamber was identical).

When one chamber inflated, the leg extended and bent in plane (Figure 3.3a). We developed two different planar models: i) *Linear Spring* model and ii) *Prismatic Joint* model (Figure 3.3c). The *Linear Springs* model included masses, translational springs and dampers, and rotational springs and dampers distributed along the centerline. The *Prismatic Joint* Model includes masses, prismatic joints, and rotational springs and dampers distributed along the centerline.

The planar bending models were described in a 2D *xy* coordinate system. Let x_i and y_i be the coordinates defining the end position of element i with mass m_i. Each translational spring or prismatic joint element extended from the nominal length l_0 to a length l_i. Each torsional spring rotated about an axis that was normal to the *xy* plane. The angle α_i was measured from the relative x axis of each element.

The forces and torques that move each leg were described in terms of the pressure in each chamber. The torques were applied at each joint along the centerline and the forces were located at the center of the inflating chamber. The force was applied along unit vectors that point from one element to the neighboring element. The forces and torques that moved the soft elements depended on the pressure in each chamber. The inflation pressure dynamics of each chamber in each leg was represented as:

$$P_{Cn}(t) = P_e + (P_s - P_e)e^{-\frac{t}{\tau_{in}}} \tag{3.1}$$

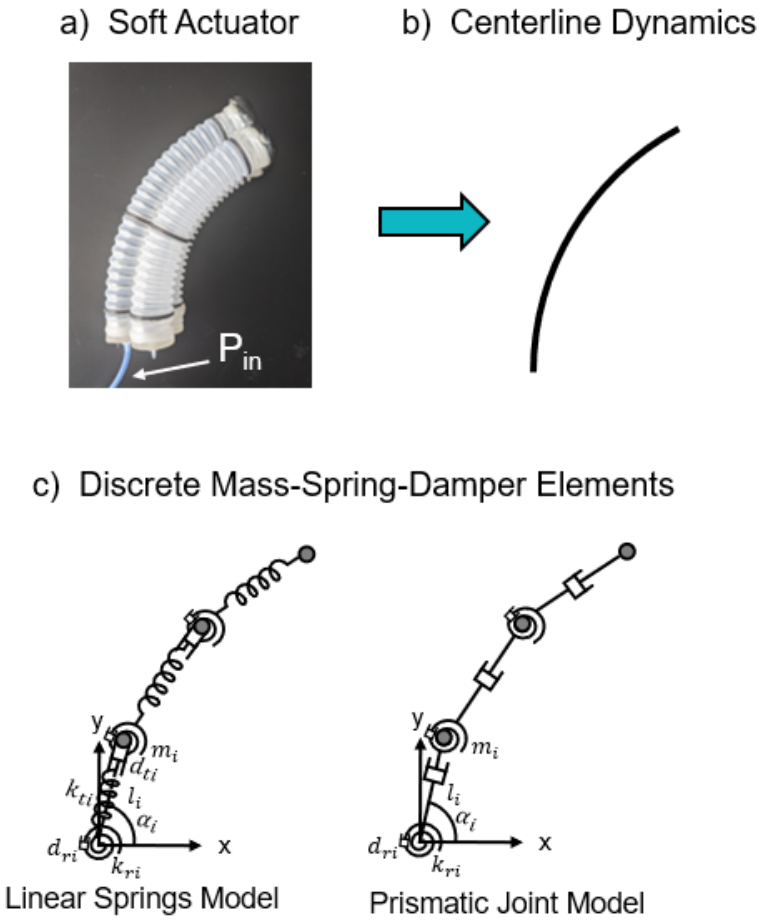

Figure 3.3: Analytical description of the soft leg dynamics. a) When one chamber was pressurized, the actuator bent towards the uninflated two chambers. b) The movement of the soft actuator was described based on the movement of the centerline of the actuator. c) The centerline was discretized into mass-spring-damper elements to model the quadruped robot interacting with the environment.

and the deflation of each chamber was represented as:

$$P_{Cn}(t) = P_s e^{-\frac{t}{\tau_{out}}} \tag{3.2}$$

where P_{Cn} was the pressure in chamber C_n for each of the n chambers, P_s and P_e are the pressures in a chamber at the start and end of a cycle (respectively), and τ_{in} and τ_{out} were the time constants in and out of the chamber(s). During inflation, $P_s = P_{atm}$ and $P_e = P_{max}$ while $P_s = P_{max}$ and $P_e = 0$ during deflation. We identified the time constants (τ_{in} and τ_{out}) for different numbers of

chambers by applying a step input in chamber pressure to measure the resulting pressure response in the chamber(s) (Figure 3.5).

The generalized coordinates q_i for each element i were defined as (l_i, α_i). The forces and torques representing the input u_{q_i} for each coordinate and each element were defined as:

$$u_{q_i}(t) = k_{q_i}(q_{di} - q_{0i}) \tag{3.3}$$

where q_{di} was the desired generalized coordinate for element i and q_{0i} was the initial position or orientation of element i.

We fit a quadratic function to define the steady-state trajectory of each generalized coordinate on each leg:

$$q_{i0}(P_{Cn}) = a_{Cn}P_{Cn}^2 + b_{Cn}P_{Cn} + c_{Cn} \tag{3.4}$$

where a_{Cn}, b_{Cn}, and c_{Cn} were fitting parameters for the two generalized coordinates for element i on chamber C_n (see Table 3.1 for these coefficients).

Table 3.1: Data-driven, steady-state model coefficients

	a_{Cn}	b_{Cn}	c_{Cn}	R^2
$l_{i0}(P_{Cn})$	-0.0002	0.0559	60.967	0.91455
$\theta_{i0}(P_{Cn})$	-0.0039	0.9918	4.7124	0.9703

The *Linear Spring* model included the transient and steady-state response of the translational elements while the *Prismatic Joint* model only included the steady-state response of the translational elements. The *Prismatic Joint* model reduced the model by i equations when compared to the *Linear Spring* model while still retaining model fidelity (see Results section).

Quadruped Simulation

We used Simulink®, Simscape™, and Simscape Multibody™ as the programmatic environments to simulate the movement of the robot. In Simscape Multibody™, every joint

block (i.e. every translational or rotational joint) was assigned mechanical stiffnesses, damping coefficients, and initial conditions. We configured the 3D rigid body robot mechanics based on physical constraints such as the geometry of the robot, the location of the ground and the position of the obstacles.

We precomputed the pressure dynamics (Equation 3.1 and Equation 3.2) for each chamber before running each simulation of the walking robot. We used a discrete time (0.5 ms timesteps) lookup table rather than using memory elements in Simulink to find the pressure in each chamber at each timestep. We used a simple nearest-point search method to find each pressure when using variable-step solvers.

Each foot was modeled using point contacts with frictional forces on the plane parallel to the floor. We modeled the static frictional force for each leg as:

$$F_f = \mu_s F \tag{3.5}$$

where F_f was the force of friction and μ_s was the static friction coefficient. The friction coefficient μ_s was evaluated at the point where the quadruped begun to slide down an inclined surface at an angle θ_s.

$$\mu_s = \tan(\theta_s) \tag{3.6}$$

The legs deformed when contacted by the environment (i.e. external forces) and from pressurized air (i.e. internal forces). In our model, we assumed the pressure in each chamber was not affected by contact with obstacles or the ground. In reality, the pressure in the chambers changed slightly ($\sim$15 kPa) when interacting with the ground and obstacles.

We used penalty force contact models for ground and obstacle contacts. These models increased force as two objects approached each other. The contact models were functions of the distance and velocity between two objects (h and $\dot{h}$ respectively). We used the inverse square

force law ($F_N = \frac{k}{h^2} - d\dot{h}$) for ground contact which was used in previous work [65]. For all other contacts (i.e. contact with obstacles), we used the spatial contact block (i.e. a classical spring-damper system) which is available in Simscape Multibody™. Both contact models are activated once the defined objects were less than 1 cm away from each other.

In Simscape Multibody™, models that contain physical components require variable-step, continuous implicit solvers. Implicit solvers are designed specifically for solving stiff problems. We used the solver ode23s which is based on a modified Rosenbrock formula of order two. We chose a minimum time step of 5E-4 s for our simulations.

We improved simulation speed by using the following methods: (1) parallel processing (i.e. using multiple cores), (2) fast restart (i.e. performing iterative simulations without completely recompiling for the next simulation), and (3) accelerator mode (i.e. the code was converted to C to speed up the simulations). The computer we used for the simulations has the following specifications: Intel i9, 12 core CPU, one NVIDIA 2080 Ti GPU, 64 GB of RAM, and a 1 TB M.2 SSD.

3.2.4 Hardware Design

The physical robot was fabricated using the same materials used in previous work [66]. To manufacture the soft legged quadruped, we used commercially-available polyvinyl chloride (PVC) cylindrical bellows (Corr-A-Flex tubing, Teleflex Inc.) for the pneumatic chambers due to their extrinsic compliance (to allow bending) combined with the intrinsic stiffness of the material (to permit large internal pressures). As a result, we actuated the robot with a maximum internal pressure of 170 kPa (compared to 110 kPa pressure from our previous, 3D printed legs[13, 52]).

The sections of tubing that formed each leg were held together with retaining rings. The robot body and retaining rings were 3D printed out of polylatic acid (PLA, Makerbot Replicator 2, Stratasys Inc.). We used a commercial multi-material 3D printer (Connex 3, Stratasys Inc.) to print the feet of the robot out of a soft material (TangoBlack+) for traction, as well as rigid back

plates to mount the legs to the body of the robot (VeroClear).

We previously used a modified version of an open-source control board [47] to control the diagonally-coupled chambers on the soft legged robot. We upgraded our control board to include twelve high flow valves (AVS-3211-24D) that were connected to a pressure-regulated pump (1/5 HP 58 PSI Oil-Free Airbrush Compressor, Central Pneumatic) (Figure 4.1b). The microcontroller (Mega 2560, Arduino) controlled the timing of the solenoid valves based on the gait sequence results from the quadruped simulations.

For each experiment, the robot walked on a chalkboard sheet. The obstacles for the confined space experiments were made by stacking and fixing two 2x4 pieces of wood on each side of the robot.

3.2.5 Parametric Identification

We used parametric identification techniques to identify the unknown model parameters which are the time constants for the pressure dynamics (τ_{in} and τ_{out}) and the leg parameters (i.e. translational and rotational stiffness and damping coefficients). We designed experiments to find each of these variables to uniquely define the configuration of the soft legs based on the pressure in each chamber.

Pressure Dynamics

We used a linear empirical model to relate the number of pressurized chambers to the time constants for the inflation and deflation phase (Figure 3.4b). We measured the rise and decay of pressure in the pneumatic chambers during the inflation and deflation phase respectively (see Supplemental Materials). The chambers were inflated for 1 second and deflated for 3 seconds. We used a nonlinear least-square fit to find the time constants for each phase.

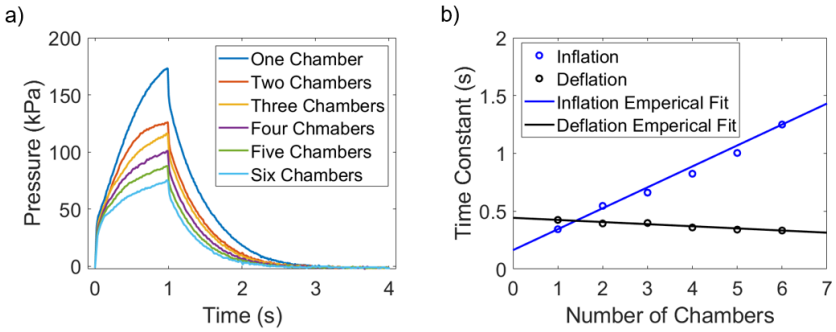

Figure 3.4: Model for pressure in each of the chambers during the gait sequence. a) Experimental results for the pressure dynamics as a function of the number of the number of inflated chambers. b) We modeled the time constants as a function of the number of chambers using an empirical linear fit ($R^2 = 0.9892$ for inflation and $R^2 = 0.9413$ for deflation). Each time constant datapoint was calculated from the exponential models (Equation 3.1 and Equation 3.2) for different numbers of inflated and deflated chambers. See example fit for a single chamber in Figure SB.1

.

Planar Bending

We described the bending motion of the leg in terms of the steady-state response and transient response. We recorded videos of the leg bending in plane and we tracked the position of the centerline of the actuator for each experiment.

We measured the static position of the leg at different constant pressures to calculate the chord length and angle of each element on the leg. We ran this experiment from 0 to 125 kPa at 25 kPa increments. We fit the quadratic model shown in Equation 3.4 to the collected data for the translation and rotation steady-state models (Table 3.1).

We assumed the leg formed a constant-curvature arc when bending in free space with radius R and angle θ. The angle θ was measured from the center of the formed circle. We placed the base of the leg at the origin and calculated the angles of each element (θ_i and α_i) and the length of each element l_i based on the position of the ends of each element (x_i,y_i).

$$x_i = R\cos(\theta_i) + R \tag{3.7}$$

$$y_i = R\sin(\theta_i) \tag{3.8}$$

$$l_i = \sqrt{x_i^2 + y_i^2} \tag{3.9}$$

$$\alpha_i = \frac{1}{2}(\pi - \theta_i) \tag{3.10}$$

We used a forced vibration analysis for the transient response of the leg. We manually displaced the actuator and recorded how the radius and angle changed as a function of time. We measured the radius and angle of the actuator at different constant pressures (from 0 to 125 kPa at 25kPa increments). For each experiment, the leg oscillated around the steady-state positions from the static experiments. We used a least-square function to minimize the distance between the measured parameters (i.e. the extension and rotation of the elements) with their corresponding mass-spring-damper model (Figure 3.5d and 3.5f).

3.2.6 Validation with Hardware

We verified the model of the quadruped by comparing the movement of the simulation to the movement of the physical quadruped prototype. We tracked the center of mass (COM) of the physical robot from the side and compared the tracked position to the COM of the robot in the simulation for (1) a gait using one diagonal pair (*One Diagonal Gait*) and (2) a gait using two diagonal pairs (*Seed Gait*). The *One Diagonal Gait* actuated one diagonal pair of leg chambers in sequence so the legs rotated clockwise or counter clockwise. The two diagonal pair gait (*Seed Gait*) used the same sequence for each leg pair as the *One Diagonal Gait* except for both pair of legs. We set the pairs of legs out of phase by 180^o (i.e. when one pair of legs was on the ground, the other pair of legs was in the air).

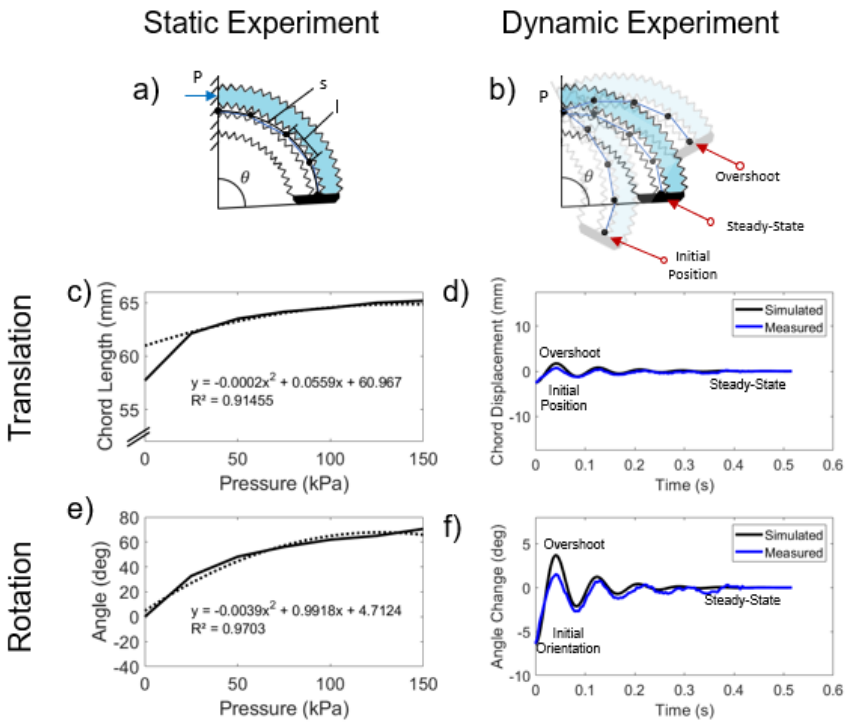

Figure 3.5: Static and dynamic planar bending experiments for modeling the movement of the soft legs. a) Schematic of the experiment used to model the steady-state response of the leg. The chord length and angle of each element was calculated when a pneumatic chamber was inflated to a constant pressure. b) Schematic of the experiment used to model the transient response of the leg. In this experiment, the leg was deflected to an initial position and orientation while inflated to a constant pressure. When the leg was released, we tracked the position at points along the leg to analyze the dynamic response of the individual elements. c) The quadratic model and experimental results for the change in chord length of each element. d) Oscillatory experimental results and mass-spring-damper model for the displacement of each element. e) The quadratic model and experimental results for the change in rotation of each element. f) Oscillatory experimental results and mass-spring-damper model for the rotation of each element.

We measured the coefficient of friction by tilting the quadruped on the chalkboard surface. The quadruped started to slip at 35^o which results in a friction coefficient of 0.7. However, we found that a friction coefficient of 0.8 more closely matched simulated results. We used a friction coefficient of 0.8 for the simulations in this work.

3.2.7 Gait Optimization

Tuning gaits by hand can be a non-trivial, time-consuming process. In addition, learned controllers can make robots crash into walls, tip over, or break. By learning controllers in simulation, soft systems can accomplish complex navigation tasks without requiring extensive experimental testing.

Researchers have evolved new behaviors and new designs of walking robots using genetic algorithms [55, 67]. Genetic algorithms are useful because there is a complex relation between the search space (i.e. all possible gait sequences) and the cost function (e.g. walking to a destination in a short amount of time) leading to multiple local minima. Genetic algorithms solve both constrained and unconstrained optimization problems on large problem spaces in hopes of finding a global optimum [64]. Genetic algorithms use the following steps to search for a global optimum :

1. Generate the initial population of individuals
2. Evaluate the fitness of each individual
3. Select the fittest individuals for reproduction (i.e. parents, elite individuals)
4. Create new individuals (i.e. children) through mutation and crossover. Children are produced either by making random changes to a single parent 'mutation' or by combining the vector entries of a pair of parents 'crossover'
5. Replace the least-fit individuals of the population with new individuals.
6. Repeat the following regenerational steps until termination (i.e. time limit, sufficient fitness achieved, etc.)

Genetic algorithms select, merge, and sort the individuals in a population to search for the minimum of a fitness function. Genetic operators (i.e. mutation and crossover) control how much

exploration versus how much exploitation is used in the genetic algorithm. The reproduction and selection processes pick two parents and uses mutation and crossover genetic operators to generate new populations. The algorithm stops when the stopping criteria (e.g. max number of generations, time limit, fitness limit, max number of stall generations, or function tolerance (i.e. change in fitness value between generations)) is reached.

Problem Formulation

We designed the genetic algorithm to optimize the gait of the simulated soft walking robot. The fitness function (i.e. objective function) is the equation that defines what is a "good" gait. The genetic algorithm was designed to: 1) improve locomotion speed on flat ground and 2) enable the robot to squeeze through a small opening. We set the fitness function for both cases based on the euclidean distance the robot traveled away from the origin and the time it took to get to the final position.

$$fitness = ((y_e)y_e^2 + (x_e)x_e^2)t_e \tag{3.11}$$

where x_e and y_e are the x-coordinate and y-coordinate (respectively) at the final time step. The simulations that walked the furthest from the origin in the correct direction had the highest reward. Individuals with low fitness values were removed from the evolutionary process.

The following parameters were used to define the gait of the robot: i) the gait period (1 parameter), ii) the delay time before each chamber was inflated (c number of parameters), and iii) the time that each chamber was inflated (c number of parameters) where c is the number of controlled chambers (the total number of parameters is 1+2c). For this problem setup, we assumed that each chamber inflated once per gait cycle.

The gait period was kept to a constant 4.5 s and the chamber delay and inflation were restricted to values between 0 and 2.25 s. The max inflation time was set to half of the gait period to prevent the chambers from over-inflating after multiple cycles.

We chose the *Seed Gait* (1 second inflation of coupled chambers with a 1 second delay before inflating the next set of coupled chambers, Figure 3.6) as a seed for the initial population because we already knew before running the genetic algorithm that this gait would enable the robot to walk in the desired direction. The *Seed Gait* helped to ensure the genetic algorithm would result in a successful solution. We evolved gaits with the *Seed Gait* as the seed for all of the genetic algorithms in this work.

We chose evolution parameters that would allow the genetic algorithm to explore new gaits without veering too far away from successful simulated gait solutions. We set 5 percent of the population as elite members with the remaining 95 percent of the individuals crossed over or mutated (80 percent and 20 percent of the remaining members, respectively).

We set the simulation time for the genetic algorithms for the obstacle experiments to be 13.5 seconds (3 gait cycles) and the simulation time for flat ground simulations to be 4.5 seconds (1 gait cycle). The simulation time for the obstacle experiments was longer so the simulated robot could have enough time to squeeze through the opening. We set a maximum position (1.5 m), maximum velocity (3 m/s), and a maximum acceleration (150 m/s^2) as the stopping conditions for each simulation. The genetic algorithms stopped when the maximum number of generations was met or when the fitness value stopped changing. We used a small function tolerance (1E-20) to allow the simulations to completely evolve for all generations.

Genetic algorithms with large search spaces can result in suboptimal solutions because larger search spaces have a tendency to get stuck in stall generations. The benefit of a large search spaces is that there is potentially a better gait when compared to smaller search spaces. To test this, we ran three genetic algorithms with the chambers coupled (12 variables) and we ran three genetic algorithms when the chambers were inflated individually (24 variables). When the chambers were coupled, we performed 2,304 simulations (96 generations with a population size of 24, 4 trials). We performed 25,000 simulations (1000 generations with a population size of 25, 4.5 seconds for each simulation (1 gait cycle), 4 trials) when the chambers were inflated

individually. We also tested the individual chamber genetic algorithm with a smaller number of generations (4,704 simulations, 196 generations with a population size of 24, 4.5 seconds for each simulation (1 gait cycle), 3 trials).

When in the uninflated state, the legs easily bend, twist, and extend. However, the longer the valves are open, the more air enters the chambers which causes the legs to become stiffer. When the legs become stiff, it is challenging for the robot to squeeze through obstacles. The robot also needs stiff legs to exert forces to squeeze through small openings. Therefore, there needs to be a careful balance between softness and stiffness which makes squeezing through a small gap opening a challenging problem.

We evolved the gait of the robot to squeeze through an obstacle using a genetic algorithm (1500 simulations, 100 generations with a population size of 15, 13.5 seconds for each simulation (3 gait cycles), 3 trials).

For each of the the genetic algorithms, we implementing code that takes the optimized result and organizes the sequence order of the chambers from first to last. This part of the process was necessary to estimate which chambers were inflated at the same time to precompute the time constants for the pressure input and to generate code to implement on hardware.

3.3 Results

3.3.1 Parametric Identification

During the inflation phase, air filled the chambers causing the bellows to expand. Once the bellows were fully expanded, additional air entering the chamber was compressed. The transition between these two phases can be observed in Figure 3.4a at $\sim$40 kPa. There was an abrupt change in pressure at this point. This effect did not occur during the deflation phase because the bellows contracted while the over pressurized air was deflating.

The time constant required for characterizing the inflation phase($\tau_{in} = RC$) varied as

the number of chambers increased. The capacitance C (i.e. the volume the air needs to fill) changed as the number of chambers increased therefore the linear trend shown in Figure 3.4b matches what is expected. The resistance R (i.e. length of tubing) also increased as the number of chambers increased but that resistance change is almost negligible when compared to the change in capacitance.

3.3.2 Validation with Hardware

One Diagonal Gait

We observed that the robot walking with the *One Diagonal Gait* closely matched the predicted *Linear Springs* model, but the COM dynamics had extra oscillations. The dynamics of the *Prismatic Joint* model more closely matched the movement of the physical robot when compared to the *Linear Springs* model. It is more important that the simulation matches the physical robot so that the gait improvement from the genetic algorithm translates from the simulated environment to the physical world.

Seed Gait

When we tested the *Seed Gait* on the physical robot, we observed that the dynamics and final position along both axis in simulation matched the movement of the physical robot. After a 10 second interval, the position error was 3.9 percent of the body length (10.5 mm) in x direction and 9.4 percent of the body length (25 mm) in the y direction .

3.3.3 Gait Optimization

Diagonal Couplet

When the diagonal pairs of legs were coupled together, the overall problem search space for the genetic algorithm was reduced and the evolved fitness function quickly stabilized at a

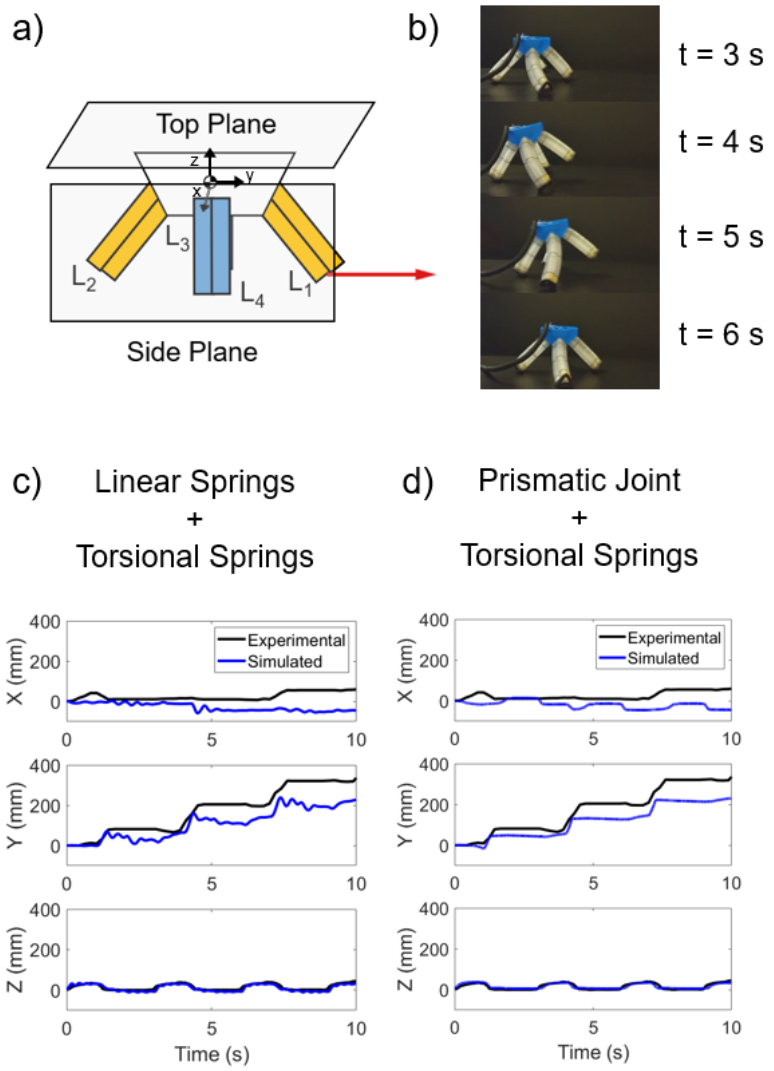

Figure 3.6: Comparison between the simulated movement of the quadruped to the movement of the COM of the physical robot walking with the *One Diagonal Gait*. a) Schematic of the robot from the side walking using the *One Diagonal Gait* on Legs L_3 and L_4. b) Screenshots from the video showing the quadruped taking steps forward by inflating each chamber in sequence (see Movie S1). We compared the movement of the physical robot walking in in x, y and z planes to the c) *Linear Springs + Torsional Springs* model and the d) *Prismatic Joint + Torsional Springs* model. We observed that the *Linear Springs + Torsional Springs* model had a close agreement between the simulation and experimental results, but there were additional oscillations. The *Prismatic Joint + Torsional Springs* model also showed a close agreement between simulation and experimental results with less equations and without the additional oscillations.

fitness value (Figure 3.8b). Although there was slight improvement in the fitness value at 80 generations, the overall gait did not significantly improve after $\sim$ 30 generations.

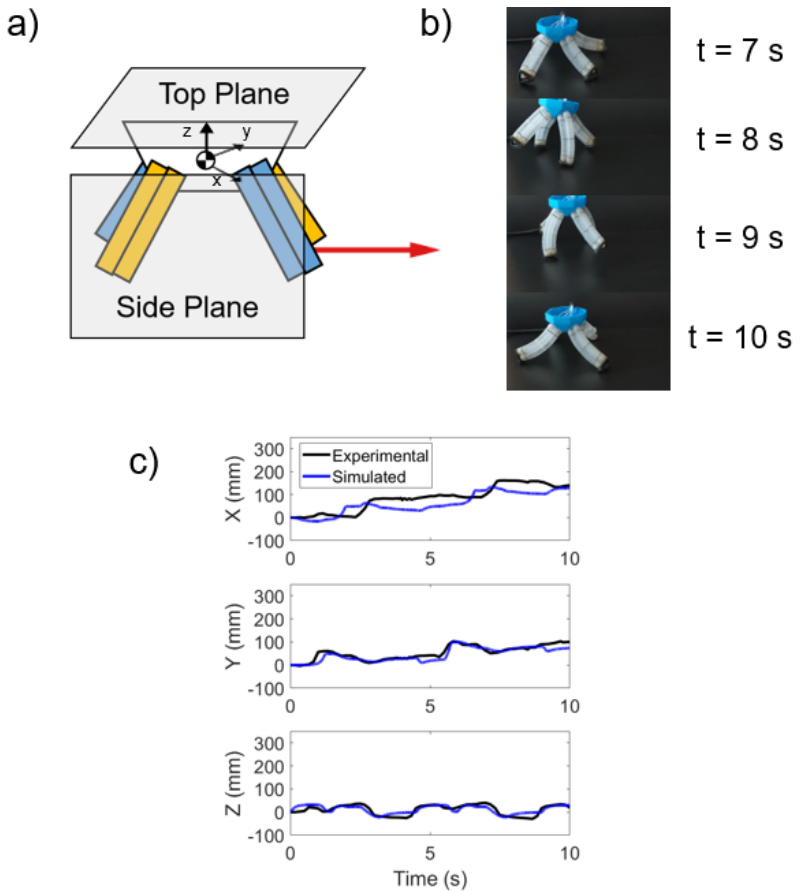

Figure 3.7: Comparison between the simulated movement of the quadruped to the movement of the COM of the physical robot walking with the *Seed Gait*. a) Schematic of the robot from the side walking using the *Seed Gait*. b) Screenshots from the video showing the quadruped taking steps forward by inflating each chamber in sequence (see Movie S2). We compared the movement of the physical robot walking in in x, y and z planes to the c) *Prismatic Joint + Torsional Springs* model. We observed that the dynamics of the simulated and experimental movement matched but there was a slight phase shift in the x-direction.

Individual Legs

It takes more generations for the fitness value in the individual chamber experiments to stall when compared to the fitness value of the coupled chamber experiments (Figure 3.8d). We noticed that the average fitness value for the coupled leg genetic algorithm was almost the same as the average fitness value for the individual leg genetic algorithm, however, there was a larger variance on the individual leg genetic algorithm. The genetic algorithm with the individual legs outperformed the genetic algorithm with coupled legs since there were more gait sequences

options to evolve. If the both genetic algorithms were run for a longer period of time, the gaits would eventually converge to a global maximum, however, we leave these simulations for future work.

Our results showed that the gaits did improve significantly when we ran genetic algorithms with the chamber inflated individually compared to the seeded gait (Figure 3.9g). We successfully improved the gait on flat ground in both simulation and on hardware. We observed that the genetic algorithm with a larger number of simulations (*Optimized Gait 1*) improved the max distance traveled more than the genetic algorithm with a smaller number of simulations (*Optimized Gait 2*) (5.3% improvement). The gaits obtained from both of the genetic algorithms improved the overall speed of the robot when compared to the seed gait (1.2 X distance traveled for *Optimized Gait 1* and 1.5 X distance traveled for *Optimized Gait 2*).

The experimental results from the genetic algorithm with a smaller number of simulations (*Optimized Gait 2*) and the *Seed Gait* closely matched the simulated results. The increased speed on flat ground demonstrates the benefits of simulating and learning new gaits in software rather than manually testing gaits on the physical soft legged robot.

The robot is unable to squeeze through a gap opening when controlled with the *Seed Gait*. When the leg are in the swing phase, the legs push against the obstacle which pushes the robot backwards and prevents the robot from squeezing through. After evolving gaits with the genetic algorithm, we found a gait that can control the robot to squeeze through a gap opening equal to 80% of the width of the robot (robot width = 250 mm) (Figure 3.9g). The robot almost able to completely navigate though an obstacle gap that was 70% of the robot's body width, however, the legs of the robot got stuck on the corner of the obstacle. A similar rigid system would not be able to squeeze though obstacles smaller than the robot's width without changing the gait for each gap width. Soft legs can use simple periodic gaits to navigate through a similar class of obstacles while a rigid robot would be unable to to accomplish this task. The results from these experiments demonstrate the benefits of soft legs and the importance of the periodic gait sequence

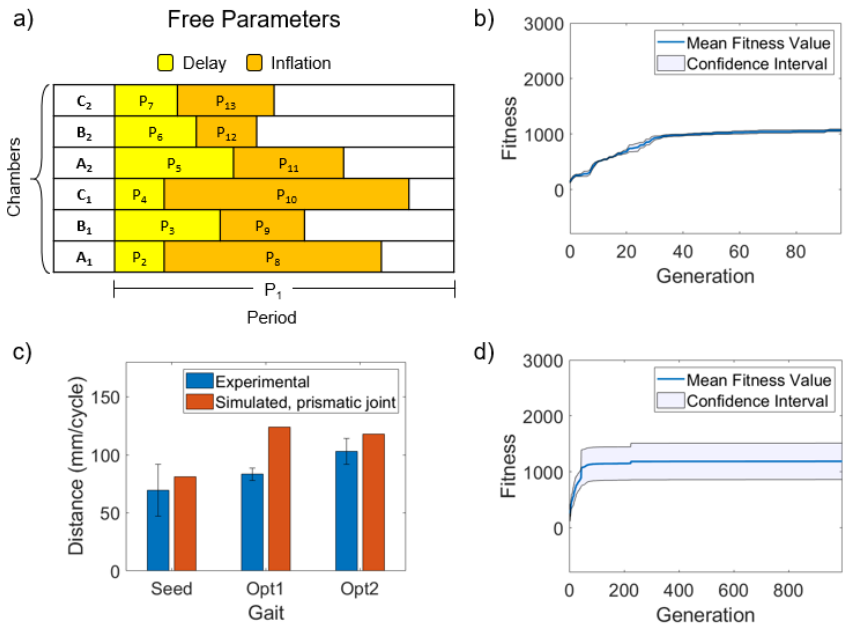

Figure 3.8: Results from the genetic algorithm for optimizing the gait of the quadruped walking on flat ground. a) Bar plot of the free parameters that are optimized using the genetic algorithm. b) Fitness evolution for each generation when pairs of chambers are coupled. Shaded region denotes one unit of standard error. c) Bar plot comparing the optimized results for the quadruped simulation to experimental results. The two are compared based on the euclidean distance per gait cycle for three different gaits (*Seed Gait*, *Optimized Gait 1*, and *Optimized Gait 2*). d) Fitness evolution for each generation when the chambers are optimized to inflate individually. Shaded region denotes one unit of standard error.

for sequencing through obstacles.

3.4 Discussion

Data collection for a simulator is less taxing on the hardware when compared to testing gait sequences directly on the robot. Hyper-parameter tuning does require experiments to develop a successful model but the number of experiments are drastically reduced. Simulating the robot makes it easier to prune out weak gaits and learn affordances about the environment in a shorter time frame.

Soft legs enable robots to traverse different classes of environments with simplified control strategies. Soft legs can take more paths (i.e. bend, twist, and deform) enabling robots to move

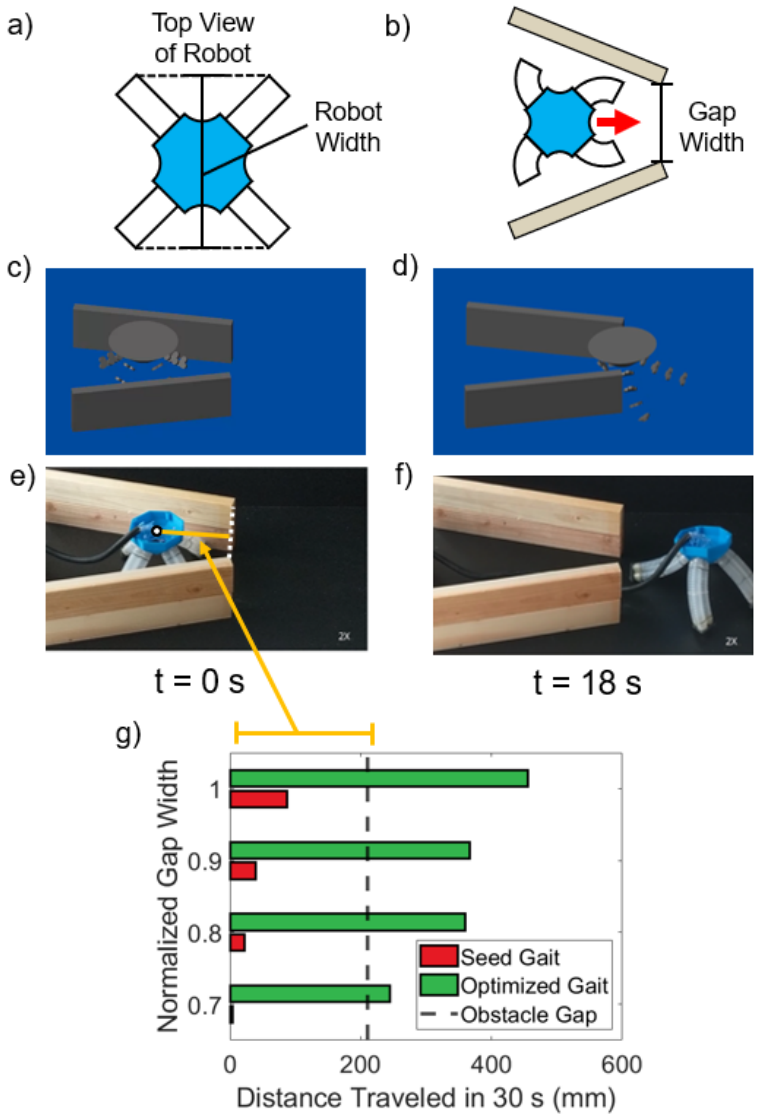

Figure 3.9: Success and failure of robot squeezing through normalized gap width (normalized by the robots width). a-b) Schematic of the robot squeezing through a gap opening smaller than the width of the robot c-d) Simulated results showing the robot before and after walking through the gap. e-f) Experimental results showing the robot before and after walking through the gap (see Movie S5). g) The results for each gap distance are plotted against the distance traveled in mm after walking for 30 seconds.

in more complex ways when compared to rigid legs. We have shown how important the gait sequence of soft legged robots can be when attempting to squeeze through an obstacle. If the gait sequence is not tuned properly, the robot will be unable to squeeze through tight spaces. The combination of soft legs with genetic algorithms enable soft legged robots to tackle challenging

navigation problems.

When modeling complex movements and interactions, it is almost impossible to exactly model the robot, the physical environment, and the interactions between the two. Robot behaviors trained in simulation do not always function properly when tested on the real robot leading to gaps between simulation and reality. In this work, we assumed that the simulated stiffness and damping coefficients were constant, however, this is not the case on the physical system. We believe the differences between the stiffness and damping coefficients is what caused the difference between the simulation results from the longer genetic algorithm (*Optimized Gait 1*) and the experimental results.

For the experiments presented, we used a constant period for each gait, however the period can also be optimized. The challenge with optimizing the period is that the parameter bounds for inflation and delay must change during the genetic algorithm to account for the changing period. Another approach would be to set the inflation and delay bounds to below enough to prevent the chambers from overinflating.

The methods presented in this work can be used to explore unique gait sequences for different environments (e.g. slippery surfaces, steps, tight vertical spaces, and rocky terrain). Previous researchers have used a simple reward function to optimize the gait of a quadruped to navigate hurdles, gaps, slalom walls, and platforms [67]. Their results show that a simple, generic reward function can be used to train non-trivial locomotion skills over a wide range of environments. The models presented in this work can be used to translate improvements in different simulated environments onto a physical soft legged robot.

There may be gaits that perform better as a generalist (i.e. gaits that are able to navigate all terrains) when compared to gaits that perform better as a specialist (i.e. gaits that are evolved for a specific terrain). This idea brings up interesting questions about how to identify gaits that are optimized for multiple environments. However, we leave this analysis for future work.

3.5 Conclusion

We developed a computationally-efficient quadruped simulator to replicate the movement of a soft legged quadruped robot. This simulator was designed to test gait sequences navigating over different environments. We validated the model with a single diagonal couplet gait (*One Diagonal Gait*) and *Seed Gait*. We then used a genetic algorithm to optimize the robotic gait to walk on flat ground and squeeze through a gap. We evolved a gait that showed 1.5 X improvement on flat ground. We found a gait that enabled the robot to squeeze through a gap up to 80% of the robot body width. The resulting evolved gaits are not intuitive to tune by hand. Robots with soft legs and simple gaits can be used to solve complex problem that are challenging for traditional rigid robots such as surveying land to help during disaster relief efforts. This work is a step towards robust walking robots using simplified control strategies.

3.6 Acknowledgements

Chapter 3 uses the material currently in preparation for the journal Soft Robotics 2021, D. Drotman, P. Glick, M.T. Tolley “Gait Sequence Optimization for Soft Legged Robots.” The dissertation author was the first author and the primary investigator of this material.

Chapter 4

Pneumatic Circuits for Controlling the Gaits of Soft Legged Robots

4.1 Introduction

Recently, soft robots that use flexible materials and structural compliance to achieve complex movements have demonstrated promise for simplifying interactions with complex environments and for safely interacting with humans [27]. Various approaches have been presented for the actuation of soft robots, including systems driven by pneumatic [48] or hydraulic pressure [1], tendons [68], or smart materials [69], [70]. Pneumatic actuation is particularly attractive for many applications due to the low fabrication complexity and the commercial availability of the required components [71]. Generally, this approach involves inflating a sealed chamber within a soft body with a controlled supply pressure. A material or geometric asymmetry then causes the soft body to move in a prescribed direction (e.g. bending, twisting, extension/contraction).

The ability of soft robots to adapt to variable terrain makes them attractive for locomotion. We have previously found that a pneumatically actuated soft-legged robot with three actuated degrees-of-freedom (DoF) per leg was able to navigate a variety of terrains (e.g. flat or valley-

shaped, covered with loose rocks or pebbles) using very simple gait patterns [13, 52]. The compliance of the soft limbs of the robot also enabled it to squeeze into tight spaces [13]. When augmented with an inflatable soft body, we further demonstrated that the robot was able to manipulate the hydrodynamic forces it experienced while walking underwater to improve locomotion for a variety of ambient flow conditions [72].

Previous pneumatically or hydraulically powered soft robots that use rhythmic motion to achieve locomotion (e.g. by walking [3, 13, 48, 52], crawling [73] rolling [74], slithering [46], swimming [1, 15, 75], peristaltic digging [76, 77], or jumping [2]), have been primarily controlled by pumps and/or solenoid valves connected to an electronic microcontroller. For example, we used a modified version of an open-source fluidic control board [47] to control the movement of our previous soft legged robot [13]. We, and others, have also used closed volume actuation systems (e.g pneumatic or hydraulic pistons) to supply both positive and negative pressure for controlling soft robotic systems [12, 78].

Despite these demonstrations, two major challenges for fluidic soft robots are the size and cost of the components (e.g. electronics, pumps and valves) required for their actuation and control [71]. Since at least one pump or valve is required per actuated degree-of-freedom, the size and cost of these components place a lower limit on the size of soft robots and an upper limit on the number of actuated DoF.

To address these limitations, recent work has investigated fluidic control circuits for soft robots. In these circuits, simple fluidic components (e.g. microfluidic valves[79]) can replace the relatively large and expensive electromagnetic components (e.g. solenoid valves). Previous work used microfluidic valves to interface with computer-controlled Braille displays consisting of 64 solenoid valves to independently actuate 32 pneumatic DoF [80]. Recent work has used microfluidic demultiplexers to decrease the number of solenoid valves required per independently controlled fluidic lines (to n valves for 2^n lines) [81]. The disadvantage of demultiplexing schemes is that only one of the outputs can be controlled at a time, limiting the temporal resolution of

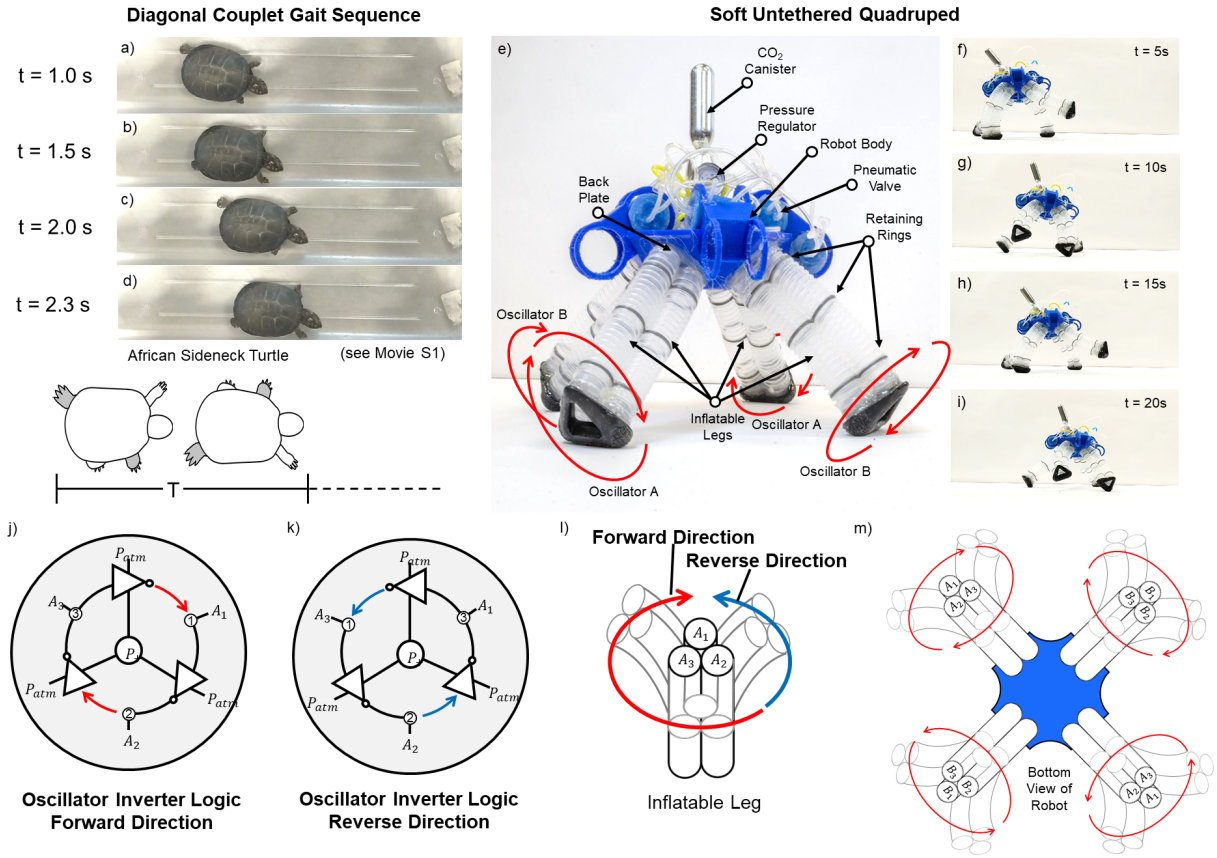

Figure 4.1: Soft legged untethered quadruped robot with a bioinspired gait pattern controlled with an electronics-free pneumatic actuation system. a-d) African sideneck turtle exhibiting a diagonal couplet walking gait. e) Image of the untethered quadruped robot with onboard soft valves powered by a pressure-regulated CO_2 canister; key components are labeled, as are the directions of leg motions for forward walking. Pneumatic oscillators are used to control the motions of each diagonal leg pair for forward walking. f-i) Sequence of images from a video of the robot walking using only the pressurized CO_2 canister as a source of energy, with two pneumatic oscillator circuits generating rhythmic leg actuation. j) Pneumatic logic circuit for rhythmic leg motion. A constant positive pressure source (P_+) applied to three inverter components causes a high pressure state to propagate around the circuit, with a delay at each inverter. While the input to one inverter is high, the attached actuator (i.e. A_1, A_2, or A_3) is inflated. This sequence of high pressure states causes each pair of legs of the robot to rotate in a direction determined by the pneumatic connections. k) By reversing the sequence of activation of the pneumatic oscillator circuit, the attached actuators inflate in a new sequence (A_1, A_3, A_2), causing l) the legs of the robot to rotate in reverse. m) Schematic bottom view of the robot with the directions of leg motions indicated for forward walking.

actuation.

Garrad et. al developed an alternative type of fluidic circuit that converts sequences

of conductive and dielectric fluids into analog or digital signals that can be used to generate sequences of actuation to control soft robots such as a soft worm [82]. This approach has the potential to reduce some of the components (e.g. valves) required to control a soft robot, but still relies on a combination of fluidic and electrical components, and has yet to demonstrate control of complex soft legged robot.

To reduce the cost and complexity of soft machines, and enable applications in environments at risk of spark ignition (e.g. in underground mines), recent work has investigated fluidic circuits for controlling electronics-free soft robots. This work builds on a rich area of research on the design of integrated microfluidic circuits for signal generation and computation [83–88]. Integrating an oscillating microfluidic circuit into a soft body has led to a fully soft untethered robot that used monopropellant decomposition to power a simple motion pattern [89]. However, this work did not present an approach to control complex motions (such as the gait cycles of a legged robot), and the physical dimensions of the microfluidic channels limited the fluid flow rate—and hence power—of the actuators. Recent work took a step towards a microfluidic controller for legged robots [90]. With power, control, and clock inputs, this work demonstrated the selection of states (walking or grasping) for a rigid robot. However, this work did not address the generation of clock signals, or an approach to enable sufficient fluid flow to actuate a soft robot.

Rothemund et al. developed bistable valves that enabled sufficient fluid flow for controlling pneumatic soft robotic devices such as a gripper and an earthworm-inspired robot [91]. Subsequent work used similar valves to demonstrate digital logic circuits for soft robots [92], and to generate a soft ring oscillator that produced a continuous oscillatory movement for devices such as a rolling robot, and a device for separating particles [93]. However, this work has not addressed the challenge of generating more complex, coordinated motions for soft robots with many DoF, as required to generate responsive gaits for a walking robot.

Nature, however, provides inspiration for how to generate motion from oscillatory circuits.

Control circuits known as central pattern generators (CPGs) are used by natural organisms to produce rhythmic movements such as walking, flying, and swimming [94]. For example, CPGs observed in *Xenopus* tadpoles [95] and lampreys [96] produce simplified oscillatory movements with minimal feedback. Animals use sensors to regulate their oscillatory gait patterns based on the environment they are navigating [97]. Examples include stick insects that navigate large gaps by changing their walking speed based on feedback from their antennas [98], and cockroaches that use antennas to detect substrate conditions and adapt their walking gait [99].

Roboticists have been inspired by pattern-generating biological CPG networks to design robots that can respond to information from their environment [100–102]. For example, decentralized coupled oscillator CPGs observed in caterpillars inspired roboticists to develop a soft-bodied robot that was able to switch between an inching and crawling gait pattern based on tactile sensory information from the environment [103]. However, previous work on generating robotic gaits based on CPGs has used electric components to generate the patterns.

This work presents pneumatic circuits composed of fluidic control components [92, 93] that are designed to control the gait of a walking robot without electronics (Figure 4.1a-g). Analogous to biological gait control, these circuits generate oscillatory signals, and adapt the oscillatory signals in response to sensor input to generate responsive gaits. Our proposed approach for controlling soft systems enables robots to interact with the environment and make decisions based on these interactions without requiring electronics (Movie 1). The innovations that enable this approach are: i) pneumatic circuits composed of a small number of fluidic control components capable of generating gaits for legged locomotion, ii) a new pneumatic memory element (designed to mimic a double-pole double-throw switch) to enable gait selection, and iii) an onboard tactile sensor to semi-autonomously switch gaits based on input from the environment. Together, these innovations enable simple fluidic circuits for controlling soft legged robots and represent a step towards developing practical, electronics-free soft robots.

4.2 Results

4.2.1 Soft legged quadruped design

To demonstrate the use of a pneumatic control system on a soft legged robot, we designed a soft quadruped with three pneumatic chambers per leg (the overall morphology was similar to our previous work [13,52], Figure 4.1). The four limbs of the robot emanated from the robot body with two perpendicular vertical planes of symmetry. Each limb was angled downward at a 45° angle relative to the horizontal, and composed of three parallel, connected pneumatic cylindrical chambers with bellows. When a chamber was pressurized, the limb bent in the opposing direction (Figure 4.1e). The three chambers of each limb provided the multi-axis bending required for walking.

4.2.2 Diagonal couplet gait control

The gait for the quadruped was defined by the duration of inflation/deflation for the three chambers of each leg of the robot. Rather than individually addressing all twelve chambers, we simplified the control problem by pairing the similar chambers on the legs diagonally across from one another (Figure 4.3b). Here, we refer to the three paired chambers of one diagonal pair as A_1, A_2, and A_3, and the three paired chambers of the other diagonal pair as B_1, B_2, and B_3. Timed actuation of the paired chambers A_1, then A_2, then A_3 caused the first pair of legs to rotate in the same direction, causing the robot to take a diagonal step. Similarly, the sequence B_1, then B_2, then B_3 caused the robot to step in a perpendicular direction (see SI Movie S1).

Reversing the sequence of actuation of the chambers in a leg pair (e.g. A_1, A_3, and A_2), caused the robot to move in the opposite direction (see section *Reversing leg rotation with a 4/2 bistable control valve for omnidirectional locomotion*, below). Thus, with linear combinations of forward or reverse steps with the diagonal leg pairs, the robot was able to walk in any direction (see SI Movie S2 and Movie S5). Rotation was also possible by reversing the direction of

rotation of one leg in a pair with respect to the other. Thus, a simplified gait control system for omnidirectional locomotion required the diagonal leg pairs to be able to rotate clockwise and counterclockwise. In the following sections, we describe the pneumatic networks we designed to achieve these rhythmic gait motions with only a single pressure supply line. We also describe how these circuits are used to switch the rotation of the legs in response to user or environmental input.

4.2.3 Rhythmic leg motion with a soft ring oscillator

To control the gait sequences discussed above without electronics, we used soft pneumatic control circuits [91–93,104]. The basic rhythmic motion of a pair of legs was generated with a soft ring oscillator [93] acting as a pneumatic CPG. The soft ring oscillator propagated continuously with a constant pressure source acting both as signal (i.e. indicating when to oscillate) and source of energy (see *Methods and Materials, Soft ring oscillator analysis* for details).

To generate rhythmic motion of a pair of legs, we connected one port of each valve of the soft ring oscillator to pneumatic chambers of the legs. One set of paired legs (e.g. chambers A_1, A_2, and A_3) was connected to the nodes of the oscillator circuit (Figure 4.2a-c) which generated pressure in the connected chambers (Figure 4.2d). The pressure generated in each chamber during this process was consistent, with an average standard deviation of pressure throughout the cycle of 9.4 kPa (see Supplementary Materials, “Consistency of Pneumatic Circuit Oscillations”).

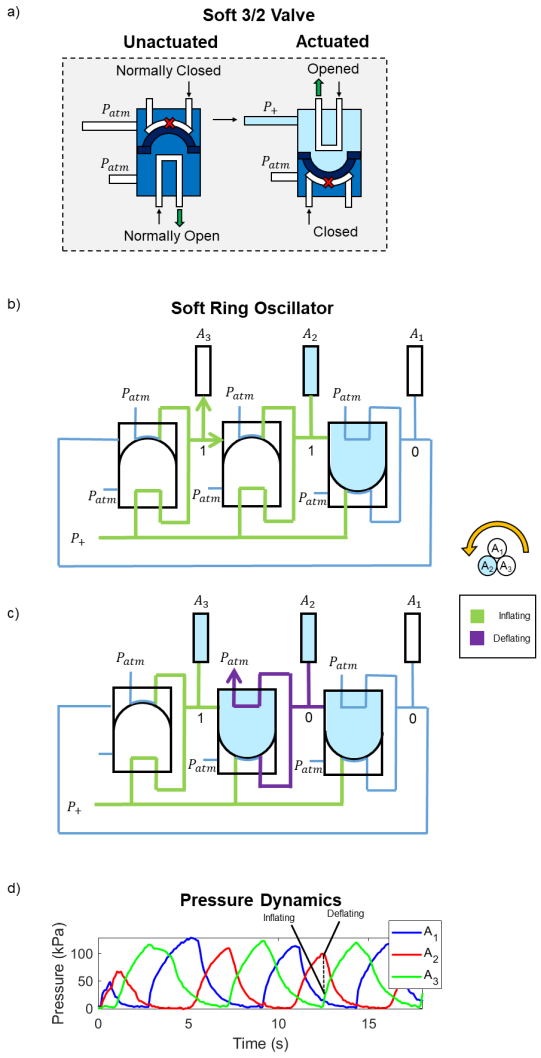

Figure 4.2: Soft ring oscillator concept. a) Each of the valves acts as an inverter by switching the normally closed half (top) to open and the normally open half (bottom) to closed. b-c) The soft ring oscillator is designed to sequence inflation and deflation of different chambers on the robot (e.g. Oscillator A: A_1, A_2, and A_3). The soft ring oscillator actuates the chambers in sequence which results in the limbs rotating in a circle. These schematics depict the moments immediately before (b) and after (c) the pressure in chamber A_3 increases beyond the valve snap-through pressure ($P_{st} = 35$ kPa). In (b) both A_2 and A_3 are inflating. In (c), once the pressure in $A_3 > P_{st}$, the exhaust for A_2 opens and A_2 begins deflating as depicted. d) Representative plot of the pressure at the three nodes of the oscillator when actuated at 150 kPa. The moments depicted in (b) and (c) are labeled on this plot as Inflating and Deflating, respectively.

4.2.4 Simplified pneumatic circuits for controlling two pairs of legs

The soft ring oscillator discussed in the previous section generated continuous oscillatory motion for a single pair of legs. However, the control of a quadruped requires coordination of two sets of diagonally connected pairs of legs to produce a diagonal couplet gait. To control both sets of legs, we considered two alternative pneumatic control circuits: a dual-purpose three-valve ring oscillator connected to both leg pairs that we call *Circuit 1*, and a circuit consisting of two three-valve ring oscillators in parallel (six valves to control the oscillation, one valve for phase control), that we call *Circuit 2*. In the following sections, we compare and contrast these options.

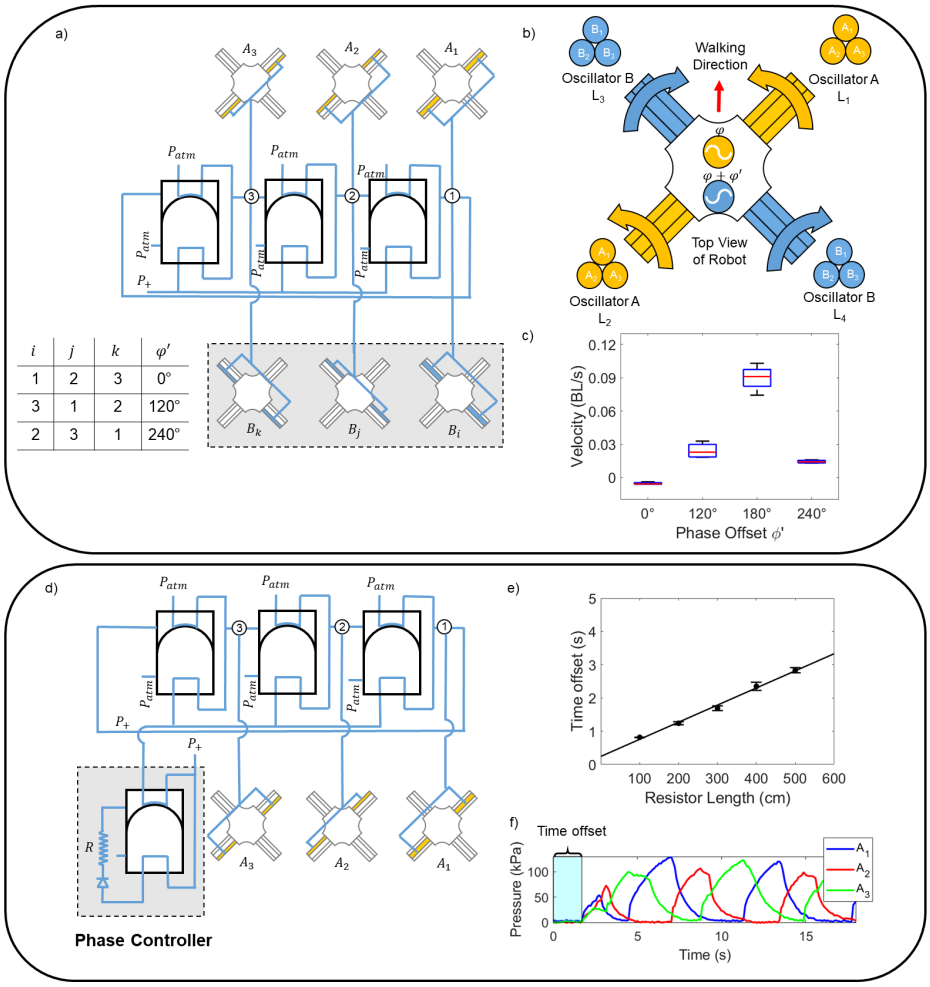

i	j	k	φ'
1	2	3	0°
3	1	2	120°
2	3	1	240°

Figure 4.3: Simple circuits for generating a diagonal couplet gait. a) The *dual-purpose three-valve ring oscillator circuit* (labeled as Circuit 1) controlled the pressure in twelve chambers with four chambers (two mirrored pairs) connected to each inverter for a phase offset of 0°, 120°, or 240° between the rotation of each diagonal leg pair (depending on the positions of the second pair of chambers relative to the first). b) Schematic of the quadruped robot controlled by Oscillator A and Oscillator B when Oscillator B has a phase offset of ϕ'. c) Box plot depicting the velocity of the robot for four different phase offsets. The 0°, 120°, and 240° phase offsets were controlled with Circuit 1 while the 180° phase offset was controlled by Circuit 2. d) The *parallel oscillator circuit* (Circuit 2) consisted of two oscillators controlling the two leg pairs in parallel. One of the oscillators was delayed by a phase controller (pictured here), and the other was not (not pictured), resulting in a one-time delay of one oscillator with respect to the other upon activation of both circuits. e) The delay was adjusted by changing the resistance of an element R (i.e. the length and inner diameter of a section of tubing) connected to an inverter so that it only delayed the circuit once at the initiation of oscillation. f) Representative measurement of the pressure in the three chambers of the delayed oscillator. The time offset delayed the initiation of the second oscillator (shaded region), effectively controlling the phase between two oscillators.

Circuit 1: Dual-purpose three-valve ring oscillator circuit

The first circuit for gait control consisted of a ring oscillator composed of three inverter valves (Figure 4.3a). This approach actuated both leg pairs simultaneously, but with a phase offset between the leg rotations. We achieved the phase offset by connecting one set of chambers (e.g. A_1, A_2, and A_3 from the first leg pair) to inverters at nodes 1, 2, and 3, respectively, and also connecting the chambers (B_i, B_j, and B_k) to the same inverters but at different node locations. When $i = 3$, $j = 1$, $k = 2$, this resulted in a phase offset of 120° between the leg rotations, and when $i = 2$, $j = 3$, $k = 1$, this resulted in a phase offset of 240° (see table in Figure 4.3a).

While the additional capacitance of the chambers from the second pair of legs increased the delay time of each inverter (see *Methods and Materials, Soft ring oscillator analysis*), the elimination of four valves (and their corresponding resistances and capacitances) led to a reduced overall period of oscillation. Furthermore, this elimination simplified the control circuit and reduced its mass.

We measured the walking speed for all three phase offsets achievable with this control circuit—0°, 120°, 240°—and found average robot velocities of -0.005 (s = 0.001), 0.024 (s = 0.007), and 0.014 (s = 0.001) body lengths per second (BL/s), respectively where s is the sample standard deviation. (Note: With all the legs rotating in unison, all feet stayed in contact with the ground throughout the gait with a little backward motion due to asymmetries in the friction at the feet.) For details on the method of velocity measurement, see *Materials and Methods, Robot velocity measurement*. A comparison of these results with the velocity generated by the parallel oscillator circuit (described in the next section), can be found in Figure 4.3c.

Circuit 2: Parallel oscillator circuit

Tortoises with a diagonal couplet gait pattern have approximately a 180° phase offset between the periodic forces exerted by the diagonal pairs of feet [105]. It is hypothesized that tortoises have adopted this gait to minimize metabolic cost [106, 107]. In our experiments with

diagonal couplet gaits with 120°, or 240° phase offsets, we observed interference of one couplet with the other that reduced the overall speed of locomotion.

The possibility of improved locomotion performance with a 180° phase offset between the diagonal couplets motivated us to design and test a second gait control circuit.

Circuit 2 consisted of two ring oscillators acting in parallel, each of which controlled one pair of legs (one couplet). To tune the phase offset between the two oscillators, we introduced an additional inverter valve to control a time delay element. This time delay element was designed to delay the second oscillator only once upon initiation of the circuit (Figure 4.3d-4.3f). After initially changing state, the soft valve bypassed the resistor, so the resistor would no longer affect the period of oscillation. Thus, after the initial delay, the second oscillator produced the same actuation as it's parallel twin, except with a phase offset between the two (plus any variations due to imperfect fabrication). This approach provided finer control of the phase offset between the motions of the diagonal pairs of legs, but required a total of seven valves (six valves for oscillator control, one valve for phase control).

Comparison of pneumatic control circuits

To validate the hypothesized improved performance of the locomotion gait produced by Circuit 2, we measured the speed of the robot with the phase tuned to approximately 180° (see *Materials and Methods, Robot velocity measurement*). For gait cycles in which the phase offset between the legs was approximately 180°, we measured a walking speed of 0.090 (s = 0.012) BL/s (see Figure 4.3c). When comparing this value to those for measured for Circuit 1 with fixed phase offsets of 0°, 120°, 240°, we found at least a 270% increase in the speed of the robot with Circuit 2, justifying the additional four valves required. Note that this speed increase was in spite of the increased mass of Circuit 2 ($\sim$ 112 g) due to the four extra valves. Based on our untethered experiments with varying payload (see *Untethered operation*, and Figure S3), we would expect a 10% decrease in the speed of the robot due to the effects of this added mass alone (assuming a

linear effect of payload).

Although the negative effects of the additional weight of the valves of Circuit 2 were outweighed by the improved efficiency of the gait, our testing revealed a more practical concern: the additional valves introduced more potential points of failure. This consideration was especially important for our case of laboratory manufactured components, which had limited lifespans. Thus, to minimize the risk of failure, we chose to use Circuit 1 for the majority of our experiments, despite the reduced speed.

Reversing leg rotation with a 4/2 bistable control valve for omnidirectional locomotion

The soft ring oscillator circuits described above actuated the pneumatic chambers of the legs in continuous, cyclical patterns (with various phase offsets between the diagonal couplets). However, to change the walking direction, a more complex circuit was required to reverse the sequence of actuation of the chambers. To achieve this direction reversal with a reduced number of additional components, we designed a component to selectively switch the connections between two of the mirrored pairs of chambers and two of the ring oscillator valves, resulting in a reversed sequence (Note: This reversal was simplified by the fact that the robot had only three pneumatic chambers per leg. For a leg with more pneumatic chamber, this reversal would have required a more complex circuit).

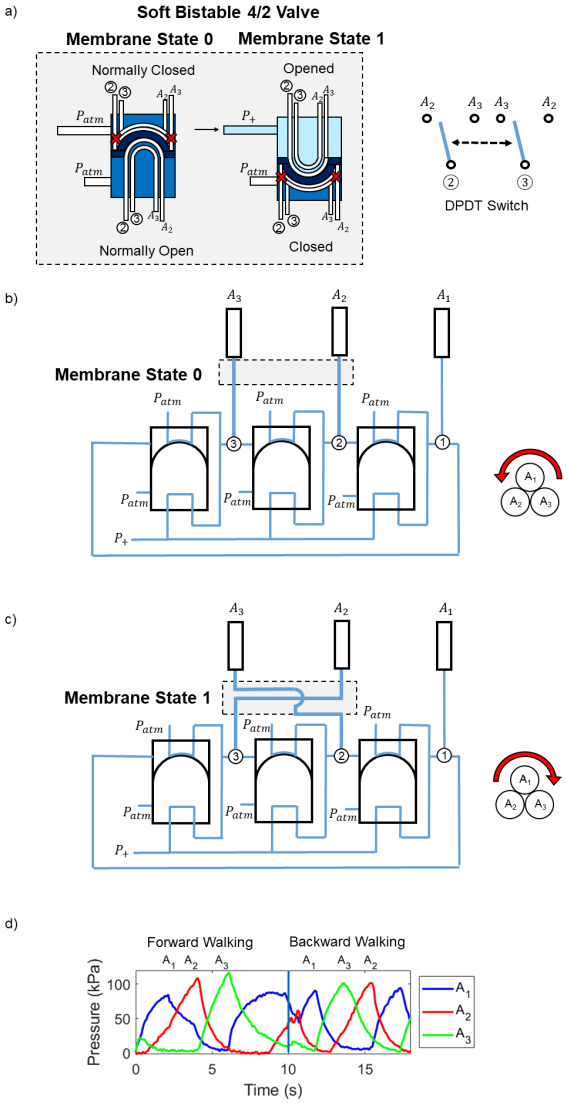

Figure 4.4: Soft bistable 4/2 valve for switching gaits. a) Operation of the 4/2 valve acting as a latching double pole, double throw (DPDT) switch. The valve switches the direction of rotation of the limbs between b) counter-clockwise and c) clockwise. d) Representative plot of the pressure in the three chambers A_1, A_2, and A_3 before and after the controlling 4/2 valve is switched (vertical line at 10 s).

We switched the connections between the oscillator and the pneumatic chambers using a soft 4/2 bistable control valve that is analogous to a latching double pole, double throw (DPDT) switch (Figure 4.4a). This valve controlled the flow between four ports by switching between two different states (corresponding to counterclockwise or clockwise rotation of the limbs; Figure 4.4b and 4.4c respectively). Our design switched the state of an elastomeric membrane similar to

that used in the 3/2 soft valves of the ring oscillator (see Figure 4.2), except with two (rather than one) fluid lines connected to either side of the membrane. As a result, the sequence of chamber pressurization reversed when pressure was applied to switch the state of the 4/2 valve (either manually, or with a fluid; Figure 4.4d). Because the membrane was bistable, the valve did not require continuous pressure to remain in a state.

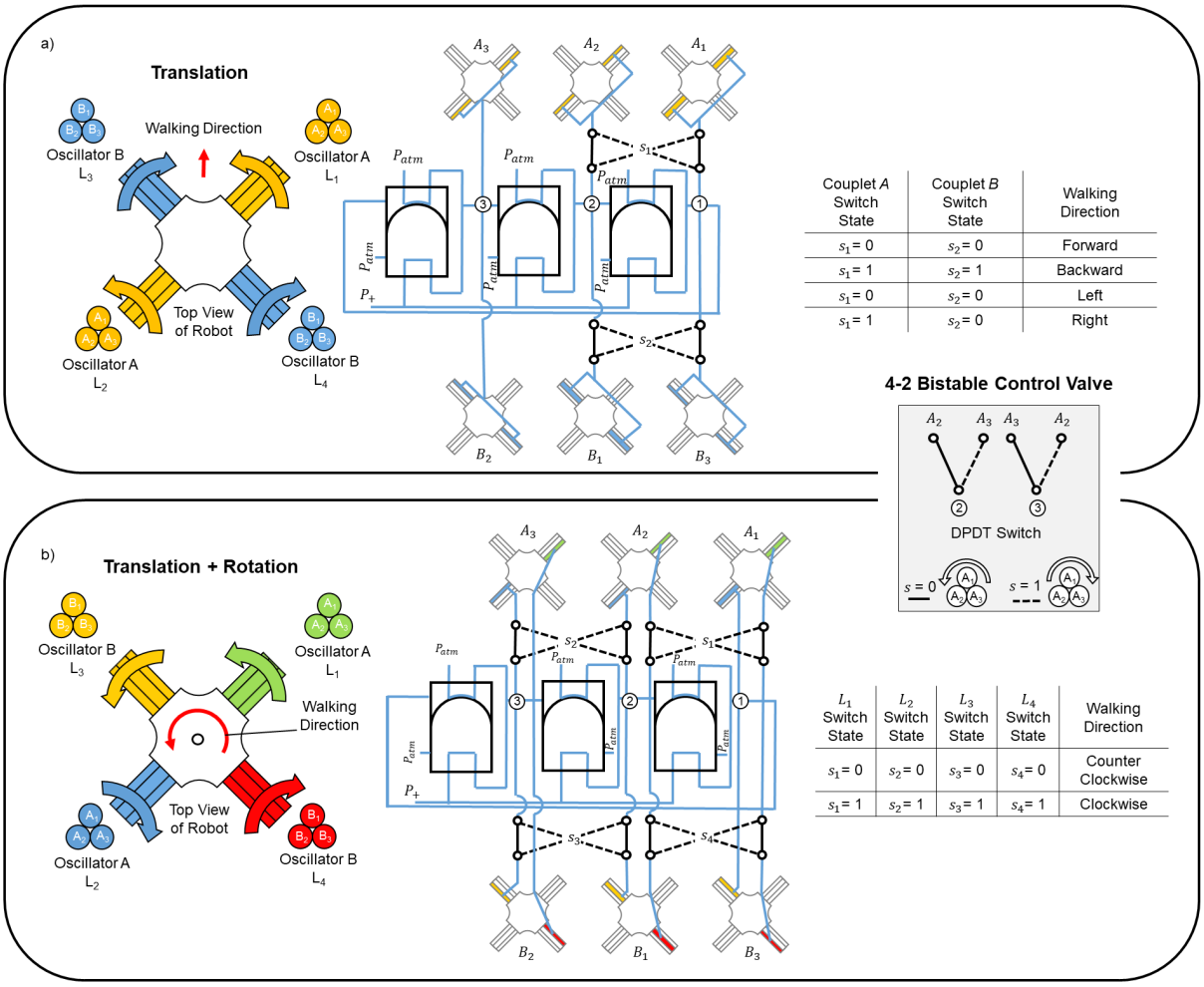

Figure 4.5: Omnidirectional control of the walking direction of the robot with 4/2 valves. a) The output sequences of a three-valve ring oscillator circuit are controlled by the states of the two 4/2 valves. The states of the valves control the direction of rotation of the two diagonal leg pairs. We connected the 4/2 valve between two of the chambers to switch the chamber order for the soft ring oscillator sequence. The robot can translate in four directions based on the states of the two 4/2 valves. b) By adding a 4/2 valve to the outputs corresponding to each leg, the robot can rotate clockwise or counterclockwise in addition to translating in any direction.

The 4/2 valve was partially enabled by an innovation in our soft valve design as compared to previous soft valves used to actuate soft robots [91–93]: we found that by adhering the tubes

directly to the membrane, they could be kinked (closed) in one membrane state, and opened in the other (see Figure 4.4). This approach allowed us to simply adhere both tubes next to one another for the 4/2 valve. See *Materials and Methods, Soft valve fabrication* for fabrication details.

The bistable valves allowed selection of the direction of rotation of each pair of legs. Thus, we used two 4/2 bistable control valves (one for each leg pair) to control the translational walking directions of the robot (Figure 4.5a). Two more 4/2 valves (e.g. one per leg, to individually control the direction of rotation of each leg) could be used to control either clockwise or counter-clockwise rotation (Figure 4.5b) which is left for future work. The mapping between the 4/2 valve states and the motions of the robot are shown in the tables in Figure 4.5.

Tethered control of omnidirectional locomotion

To test control of omnidirectional locomotion, we developed a manual controller to control two 4/2 valves (Figure 4.6a-c, SI Movie S2). Each position on the manual controller corresponded with half of a 4/2 valve to keep tube routing underneath the controller. This required us to press one of the two positions corresponding to the full 4/2 valve to control the walking direction of the robot (pressing both simultaneously would result in an undefined gait). We sequentially commanded the robot to walk forward, left, backward, then right by changing the corresponding valve states with the manual controller. Aside from this input, the robot required only a constant source of pressure to generate the appropriate gaits. We demonstrated omnidirectional control (Figure 4.5, SI Movie S2) using the *dual-purpose three-valve ring oscillator circuit*. Although this circuit resulted in slower gaits, it was simpler and lighter than the alternatives which each required seven valves.

As a demonstration of the use of omnidirectional locomotion for obstacle avoidance, we controlled the diagonal motion generated by one oscillator with forward movement generated by both oscillators to navigate around an obstacle (Figure 4.6d-f, SI Movie S4).

The motion of the robot was quasi-static (no ballistic phase). Thus, when one pair of legs

rotated, the robot leaned on one of the limbs of the opposite diagonal pair to remain stable. As a result, based on tracked data of six steps from SI Movie S1, the top of the feet lifted an average of 150.93 mm ($s = 27.44$ mm) which is 72% of the robot height. The ability of the robot to lift its feet this high off the ground could enable the robot to navigate over a variety of obstacles. We leave further investigation of navigating over obstacles to future work.

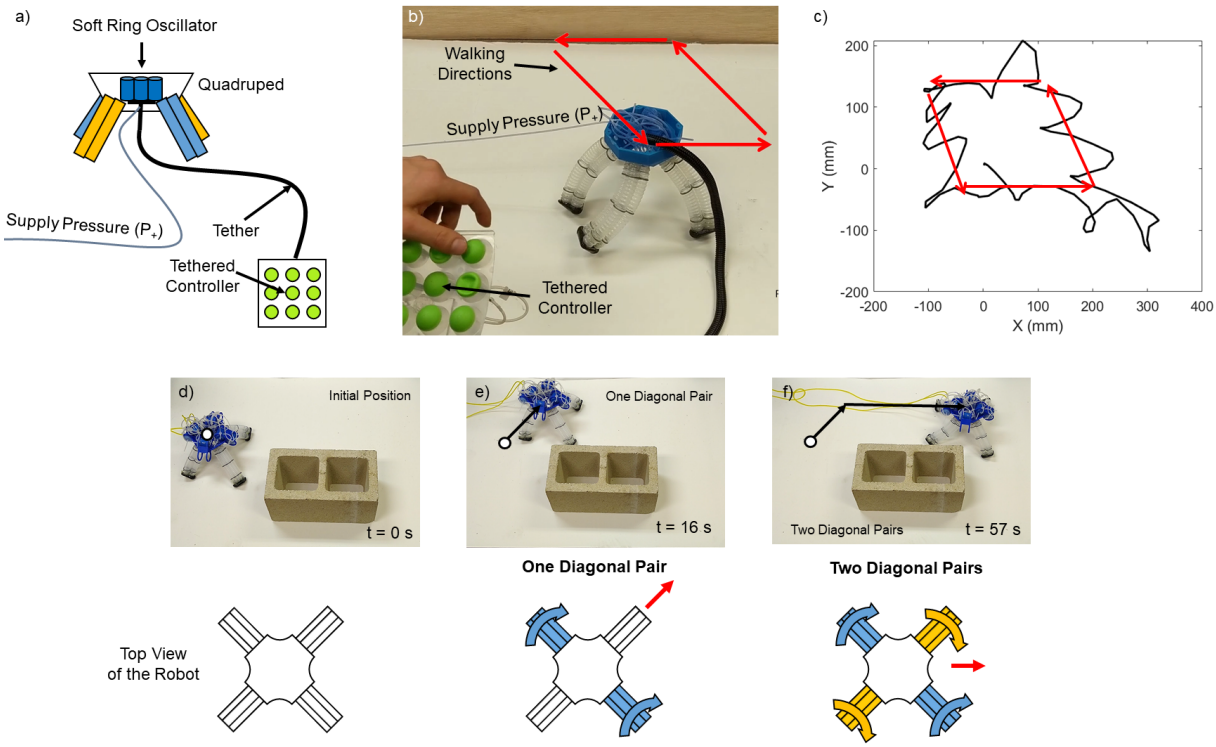

Figure 4.6: Tethered control of the quadruped robot. a) Schematic of the robot, with a single pressure supply line, tethered to a manual controller. b) Image from demonstration of the robot walking forward, left, backward, then right in sequence, with commanded directions indicated. c) X-Y position of a single point on the robot body during the experiment (see SI Movie S2) tracked from the video with motion tracking software. d-f) Images of demonstration of manually controlled obstacle avoidance by first walking diagonally using one diagonal pair of legs and then walking forward with both diagonal pairs, with associated schematics indicating the actuation of the legs.

Tactile sensor

We designed a soft sensor to semi-autonomously trigger a reversal of the walking gait upon contact (Figure 4.7, SI Movie S5). The sensor was composed of an elastomeric membrane

connected by a fluidic transmission to a 4/2 bistable control valve. When an object contacted the sensor, the membrane pushed on the enclosed transmission fluid (water) to immediately switch the state of a connected 4/2 control valve, resulting in a reversal of the direction of motion of the robot (see previous section). This computation was done onboard the robot without any electrical components. To increase the sensitivity of the sensor to external contact, we pre-pressurized the transmission fluid until the connected 4/2 valve was near the point of instability but still stable (the fluid was initially pressurized to less than P_{st} for the bistable valve to remain in the initial state).

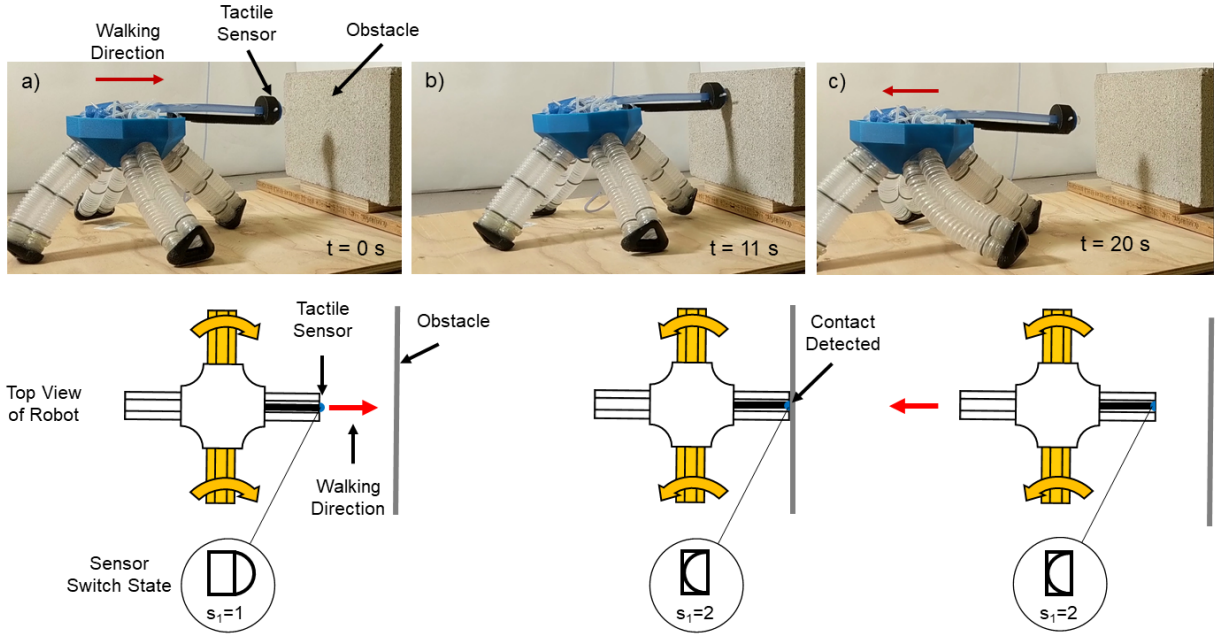

Figure 4.7: Sensor input for autonomous gait reversal. Contact with the wall switches the walking direction of the robot by switching the state of a soft sensor that is connected to a 4/2 bistable valve. a) The pneumatic control circuit powered by a constant pressure source actuated one diagonal pair of legs causing the robot to walk towards a wall. b) When the soft sensor contacted the wall, the soft sensor switched state and c) the robot began walking in the opposite direction.

4.2.5 Untethered operation

We demonstrated untethered walking of the robot by powering it with a disposable CO_2 canister and a pressure regulator (Figure 4.1a-g). We tested the robot walking with the CO_2

regulated to 140 kPa. The smaller 57 g CO_2 canisters provided $\sim$45 s of operation and the larger 306 g provided $\sim$4 minutes at this operating pressure. We used Circuit 1 for each of the demonstrations of the untethered robot.

Although the larger canister provided a longer operating time, the added weight of the larger canister and regulator (666g, or 170% of the weight of the robot) negatively affected the speed of the robot, causing it to walk 42% slower than when carrying the smaller canister and regulator (194 g, see Figure S3).

Additionally, we measured the mass of compressed gas used per unit distance traveled by the robot when walking over a 30 second interval of the gait by weighing the canisters before and after walking. While carrying the large canister, the robot used 1.7$\times$ the mass of compressed gas per unit distance traveled as compared to while carrying the small canister. Thus, the smaller CO_2 canister and regulator is a more efficient power source for the robot during untethered operation, but resulted in a robot with a reduced operation time (45 s vs. 4 min).

Even while controlled with a completely pneumatic circuit, and carrying its power source, the robot presented in this paper demonstrated a comparable top speed (0.09 BL/s) to our previous, tethered, soft legged robot controlled by electromechanical components (0.13 BL/s) [13, 52].

4.3 Discussion

Soft, pneumatically actuated valves are inexpensive, lightweight, and easy to manufacture as compared to the electromechanical valves commonly used to control soft robots. With appropriate design, these components can be combined to create sophisticated fluidic circuits that can control the gaits of legged robots without any electronics. In this work, we demonstrated the use of such fluidic circuits to control the omnidirectional locomotion of a soft legged robot to navigate around obstacles. These circuits used a soft ring oscillator composed of soft valves to generate rhythmic motions, which were acted on by additional control elements to adjust the

walking gaits autonomously or based on manual input.

The properties of biological CPGs provide benefits for walking gaits as they enable animals to generate stable rhythmic movements using minimal control inputs (i.e. minimal descending locomotor commands) [94, 108]. In particular: 1) The neurons in CPG networks produce signals that generate oscillatory motions (gaits), 2) these oscillatory signals are robust to disturbances, and 3) sensors inputs act on these signals to adjust the gaits in response to interactions with the environment. In this work, we have demonstrated each of these properties with our experimental soft robotic system. First, each of the pneumatic circuits presented in this work used a single pneumatic source to generate oscillatory motion, which reduced the number of components—and hence the weight—of the robotic system. Second, when perturbed (by temporarily changing the pressure in the pneumatic circuit), the circuits returned to their rhythmic oscillation within one cycle (see SI Section *Robustness of Pneumatic Circuit to Pressure Variations*). Third, the pneumatic logic components and sensors presented in this work allowed the robot to adjust its stable rhythmic pattern based on information from the external world.

With the approach described in this paper, it is possible to modulate the frequency and amplitude of the walking gaits (and hence the speed and foot clearance of the walking robot) based on the design of the pneumatic components (e.g. the dimensions of the membranes of the valves). Previous work has analyzed [109] and experimentally characterized [93] the effect of membrane dimensions on their snap-through and snap-back pressures. In this work, we have described the relationships between the snap-through and snap-back pressures required to choose a set of membrane parameters appropriate for our walking robot. Future work could investigate ways to adjust these parameters (e.g. switching between valves with different membrane dimensions) to adjust the amplitude and frequency of limb oscillation during operation.

Circuit 2 was designed with a delay element to offset the phase of one oscillator relative to another. Ideally, this phase should not shift over time. However, due to our manufacturing method and the materials used, we observed variabilities between the pneumatic parameters of

the valves and the chambers of the robot, as well as temporal variation in these parameters (see Figure S1). These inconsistencies did not have a large impact on the gait for the time frames we tested. However, future work could consider phase-locking circuits designs that can be used to prevent a shift over time in the phase between the leg pairs due to manufacturing variabilities. Circuit 1 had the advantage of avoiding this problem.

The physical size of the elements of the pneumatic circuit depended on the requirements placed on the circuit. I.e. the pneumatic elements were designed to work within the operating pressures of the soft robot and the pneumatic elements were required to transmit sufficient fluid to actuate the robot. As a result, the elements added considerable mass and volume to the system, both of which place a limit on the performance of an untethered walking robot. These challenges are exacerbated by the increase in complexity of the circuit required to increase the autonomy of the system. Approaches to reduce the mass and volume of the pneumatic circuits are needed, perhaps by separating the pneumatic system into "power" and "control" circuits as is typically done with electronics.

This work could be extended to apply to robots with more/fewer limbs or limbs with a different number of DoF. The number of DoF for the oscillatory movement scales linearly with the number of valves as long as the number of chambers is odd (e.g. oscillating 3 chambers requires 3 valves, but oscillating 4 chambers requires 5 valves). However, reversing sequences of more than 3 chambers requires more 4-2 bistable valves. By inspection, we find that for n chambers on each leg (when n is greater than 1 and odd), there needs to be $\frac{n-1}{2}$ bistable valves to change the direction of rotation of the legs.

Future work could also investigate increasing the mobility of soft walking robots. Potential avenues of research include autonomous object traversal and the navigation of natural terrains. These feats would likely require a more sophisticated network of sensors, and a correspondingly more complex pneumatic control system.

Overall, the integration soft pneumatic control circuits into the body of the robot is a step

towards autonomous, electronics-free, mobile soft robotic systems. Inspired by animals with simple nervous systems that are able to produce coordinated oscillatory movements regulated by sensor feedback [95, 96], this work has demonstrated a pneumatically powered and controlled soft robot to generate complex locomotion without electronics. This approach could lead to robots useful for a variety of applications, including operating in environments sensitive to spark ignition (e.g. in underground mines), in environments that do not allow metal (e.g. in an operating MRI machine), or for the mass production of simple, inexpensive autonomous systems (e.g. for cleaning robots or for entertainment). (For further discussion of potential applications, see Supplementary Materials, *Considerations for future applications*).

4.4 Materials and methods

4.4.1 Soft robot fabrication

To manufacture the soft legged quadruped, we used commercially-available polyvinyl chloride (PVC) cylindrical bellows (Corr-A-Flex tubing, Teleflex Inc.) for the pneumatic chambers due to their extrinsic compliance (to allow bending) combined with the intrinsic stiffness of the material (to permit large internal pressures). As a result, we were able to actuate the robot with a maximum internal pressure of 170 kPa (compared to 110 kPa pressure for our previous, 3D printed legs[13, 52]). The sections of tubing were held together with retaining rings. The robot body and retaining rings were 3D printed out of polylatic acid (PLA, Makerbot Replicator 2, Stratasys Inc.). We used a commercial multi-material 3D printer (Connex 3, Stratasys Inc.) to print the feet of the robot out of a soft material (TangoBlack+) for traction, as well as rigid back plates to mount the legs to the body of the robot (VeroClear).

4.4.2 Soft valve fabrication

The valves were composed of a cylindrical body, two caps and tubing. The body of the soft valves and caps were molded out of a soft polymer (MoldStar 30, Smooth-On Inc.). The polymer was poured into a 3D printed mold made of polylactic acid (PLA, Makerbot Replicator 2). The caps closed off the normally-closed and normally-open cavities of the valve. We used a silicone adhesive (SilPoxy) to adhere the caps of the valve to the cylindrical body. Tubes were fed through the side walls of the cylindrical body and the caps to create the inlet, exhaust, and opened/closed airways (see Figure 4.2). Please refer to Supplemental Materials for more details.

Control valve characterization

We measured the snap-through and snap-back pressures for an individual 3/2 valve which resulted in an average of 35 kPa (s = 3 kPa) and 20 kPa (s = 2 kPa) respectively. We fit the pressure dynamics to an exponential function (solution to Equation 4.1) and found a time constant ($\tau = RC$) of 1.32 seconds. We measured the snap-through pressure for an individual bistable 4/2 valve (including tubing on both sides) to be 35 kPa (s = 5 kPa).

Soft ring oscillator analysis

The soft ring oscillator was formed by connecting three three-port, two-state (3/2) control valves in series, where the output from one valve served as the input to the next valve (Figure 4.2a-c). Each of the soft valves acted as an inverter (i.e. a NOT logic gate) with a time delay; thus the soft valves switched the state of each connected chamber from a high (inflated) state to a low (deflated) state, or vice versa. The valves regulated flow by closing and opening channels using a snap-through instability in a hemispherical elastomeric membrane. The valves switched between one of two states whether pressure was applied to the surface of the membrane.

The pneumatic soft ring oscillator can be modeled based on analogous electrical components [93], leading to the following relationships for the resistance, capacitance, and pressure

dynamics of the valves:

$$\frac{dP}{dt} = \frac{1}{RC}(P_i - P) \tag{4.1}$$

$$R = R_{tubing} + R_{inverter} \tag{4.2}$$

$$C = C_{chamber} + C_{inverter} \tag{4.3}$$

$$R_{tubing} = \frac{128\mu L}{\pi\rho D^4} \tag{4.4}$$

$$C_{chamber} = \frac{V_0 M}{R_u T} \tag{4.5}$$

where μ is the dynamic viscosity of air, L is the length of the tubing, ρ is the density of air, D is the inner diameter of the tubing, $C_{inverter}$ is capacitance of the inverter, $R_{inverter}$ is resistance of the inverter, R_{tube} is the resistance of added tubing, V_0 is the volume of air in the reservoir, M is the molar mass of the air, R_u is the universal gas constant, T is the temperature of the air, and P_i can either be P_+ (supply pressure) on inflation or P_{atm} on deflation.

The time delay propagated through each valve t_p was determined based on the two states of the membrane in the valve

$$t_p = RC\left[ln\left(\frac{P_{atm} - P_+}{P_{st} - P_+}\right) + ln\left(\frac{P_+ - P_{atm}}{P_{sb} - P_{atm}}\right)\right] \tag{4.6}$$

where P_{st} is the the snap-through pressure of the membrane, P_{sb} is the snap-back pressure of the membrane, and the supply pressure is P_+. If the tubing, chambers, and valves in the soft ring oscillator are the same, the period of oscillation is $T = nt_p$ where n is the total number of valves. The values of R and C can be tuned to adjust the time it takes for pressure to propagate through

each valve, hence, R and C can be used to adjust the period and timing of a soft ring oscillator.

Soft ring oscillator characterization

We measured the pressure in the oscillator at the nodes connected to one set of diagonally connected legs and processed the data with a ten point moving average sampled at 40 Hz for the case of free oscillation (Figure 4.2d). The average period for one complete cycle of the soft ring oscillator actuated at 150 kPa was 8.13 s ($s = 0.12$ s). The nodal pressures were measured with pressure sensors (100PGAA5, Honeywell International Inc.). The period between the peak pressures measured in each sequential node was 2.73 s on average ($s = 0.12$ s).

Differences between the pressure signals were due to slight variations in the fabrication of each valve.

For a soft ring oscillator formed of bistable valves, a high frequency spike occurred in the pressure when it reached the critical snap-back and snap-through pressures of the membrane [93]. In our oscillator, the pairs of limbs of the robot stored large volumes of air (i.e. had high capacitance), thus effectively acted as low-pass filters, filtering these high frequency pressure changes (Figure 4.2d).

Setting the phase delay of the parallel oscillator control circuit

The time offset for the parallel oscillator circuit was controlled by adjusting the length of tubing of the resistor. The length of tubing changed the time delay of the second oscillator with respect to the first in the parallel oscillator circuit (see *Circuit 2: Parallel oscillator circuit*). We measured the time delay in the ring oscillator circuit using different tube lengths (Figure 4.3e). To determine the time offset, we measured the pressure before and after the phase control elements as we applied a step input pressure. We performed five experiments for each resistor length and fit the data points to a linear trendline. An increase in the length of the tubing corresponded with a linear increase in the phase offset. This is consistent with our model which predicts that the

time delay of a valve varies linearly with its resistance R (Equation 4.6). We used tubing with a 0.3 mm inner diameter that was looped to keep the resistor in a small form factor. We looped the tubing eight times for each trial to control for the effect of the number of loops of tubing on the fluidic resistance. Each length of tubing was tested three times at a constant applied pressure of 155 kPa. The capacitance of the additional valve and tubing connecting the phase controller to the circuit also contributed to the time offset (we assumed that this was constant for each trial, i.e. that the capacitance change due to the change in the length of the looped tubing was negligible). We used a similar approach as used to characterize the pressure in the soft ring oscillator (see *Soft ring oscillator characterization*) to measure the pressure in the nodes of the oscillator with a phase delay component (Figure 4.3f).

Characterization of oscillation reversal with a 4/2 valve

We used a similar approach as used to characterize the pressure in the soft ring oscillator (see *Soft ring oscillator characterization*) to measure the pressure in the nodes of the oscillator before and after a 4/2 valve was used to switch the output sequence (Figure 4.4d). The timing within the oscillation cycle in which the 4/2 valve switched state determined how the pressure responded (i.e. pressure stored in the chambers, tubing, and valves was either released or reused after the switching occurred). While variable, the time delay during the transition was small ($<$ 1 second) relative to the time scale of the oscillation period.The experiments for switching the direction of the robot were performed using Circuit 1, however, since the soft ring oscillator circuit was identical to those used in Circuit 2, the direction reversal would work in the same way in both cases. It should be noted, however, that the simultaneous reversal of the two oscillating circuits could lead to variations in the phase offset between these circuits. We leave further investigation of this challenge to future work.

Controller fabrication

A manual controller was manufactured to control the walking direction of the robot. The controller was manufactured from an array of bistable elastomeric hemispheres from an ice tray (Zing Pop-Out Ice Cube Tray, Robinson Home Products Inc.). Each position on the controller was designed to behave in the same way as half of a 4/2 control valve. There were two tubes beneath each position on the controller that kinked when each of the membranes on the controller were pressed. The tubes routed beneath each of the membranes were routed as shown in Figure 4.5a.

Robot velocity measurement

We measured the velocity of the robot by tracking the movement of the robot body during multiple gait cycles. We actuated the robot with a set gait sequence and used the body of the robot and leg of the robot as visual markers to measure the displacement of the robot for each cycle. We recorded videos for each gait and tracked the position of the body using an open source video analysis software (Tracker [110]).

4.5 Acknowledgements

Chapter 4 uses the material as it appears in the published paper in Science Robotics 2021, D. Drotman, S. Jadhav, D. Sharp, C. Chan, M.T. Tolley “Pneumatic circuits for controlling the gaits of soft legged robots.” The dissertation author was the first author and the primary investigator of this material.

Appendix A

Supplemental Materials: Application-Driven Design of Soft, 3D Printed, Pneumatic Actuators with Bellows

A.1 Bending of a Circular Beam using Castigliano's Method

When an elastic beam is deflected by a generalized force, the generalized deflection is equal to the partial derivative of the strain energy. The strain energy due to bending is [111]

$$U = \int_0^{\theta} \frac{M^2}{2E_{eff}I} \rho d\alpha \tag{A.1}$$

where U is the strain energy, M is the moment, and α is the angle of the curved beam. The deflection of the bending beam is

$$\delta = \frac{dU}{dF} = \frac{1}{E_{eff}I} \int_0^{\theta} M \frac{\partial M}{\partial F} \rho d\alpha \tag{A.2}$$

where F is the generalized force, and δ is the generalized deflection. The effective elastic modulus is based on the stiffness of the three chambers of the actuator

$$E_{eff} = \frac{l}{A_0} \sum_{i=1}^{3} k_i \tag{A.3}$$

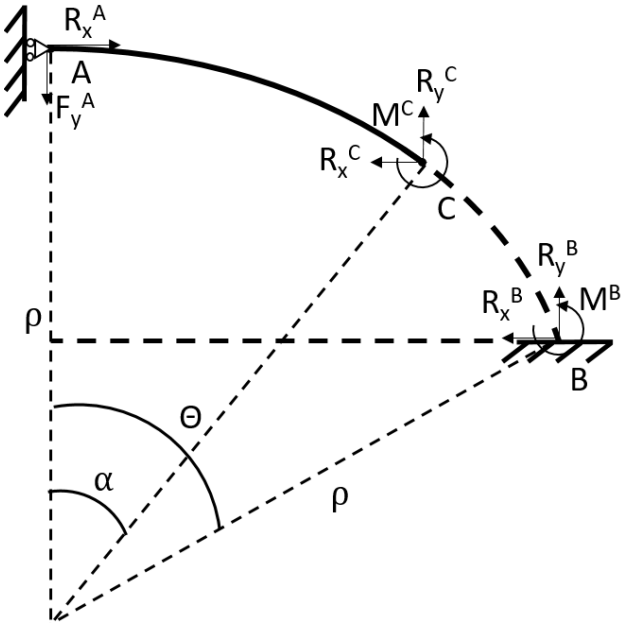

Figure A.1: The height of the robot and vertical actuated force is determined by analyzing the deflection of a curved beam with an applied load. Side perspective of an actuated limb with an applied vertical load.

The moment about an arbitrary point C on the arc of the leg was used to find the deflection of the leg in the x and y direction as a function of the bend angle of the leg (Figure A.1).

$$-M^C - F_y^A \rho \sin(\alpha) + R_x^A \rho (1 - \cos(\alpha)) = 0 \tag{A.4}$$

$$M^C = -F_y^A \rho \sin(\alpha) + R_x^A \rho (1 - \cos(\alpha)) \tag{A.5}$$

When the robot body is deflected by a vertical applied load, the horizontal force R_x^A is balanced with the leg on the other side of the quadruped. This dummy load is still required to determine the horizontal deflection at any point along the leg. When the horizontal force R_x^A is

cancelled, the deflections at point A is

$$\frac{\partial M^C}{\partial F_y^A} = -\rho\sin(\theta), \frac{\partial M^C}{\partial R_x^A} = \rho(1-\cos(\theta)) \tag{A.6}$$

$$\delta_y^A = \frac{\rho}{E_{eff}I}\int_0^\theta (-F_y^A\rho\sin(\alpha))(-\rho\sin(\alpha))d\alpha \tag{A.7}$$

$$\delta_x^A = \frac{\rho}{E_{eff}I}\int_0^\theta (-F_y^A\rho\sin(\alpha))\rho(1-\cos(\alpha))d\alpha \tag{A.8}$$

where δ_y^A is the vertical deflection at A and δ_x^A is the horizontal deflection at A. This is used to to solve for the vertical displacement δ_y^A in Equation A.7 and height of the leg off the ground after deflection h_F.

$$\delta_y^A = \frac{\rho^3 F_y^A}{E_{eff}I}\left(\frac{1}{2}\theta - \frac{1}{2}\sin(\theta)\cos(\theta)\right) \tag{A.9}$$

$$h_F = H - \delta y^A = \rho(1-\cos(\theta)) - \delta y^A \tag{A.10}$$

where H is the height before the applied load. The vertical force of the actuator is

$$F_y^A = \frac{E_{eff}I(\rho(1-\cos(\theta)) - h_F)}{\rho^3\left(\frac{1}{2}\theta - \frac{1}{2}\sin(\theta)\cos(\theta)\right)} \tag{A.11}$$

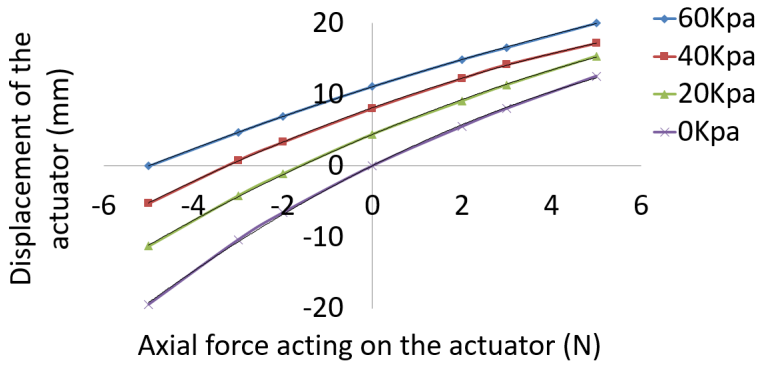

Figure A.2: We used a finite element analysis (FEM) to determine the stiffness k and extension Δl of a single bellowed chamber at varying pressures. An axial force was applied in compression and tension when one chamber was pressurized and the resulting deformation was determined. A positive sign indicates a tensile applied force while a negative sign indicates a compressive applied force.

Appendix B

Supplemental Materials: Evolution of Gait Sequences for Soft Legged Robots

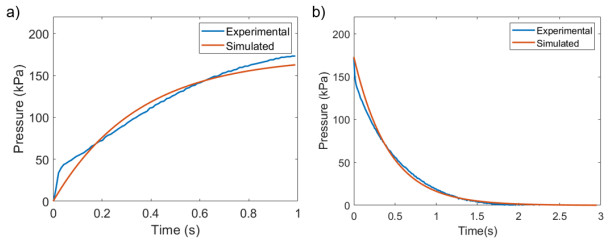

Figure B.1: Comparison between experimental results and the lumped parameter pneumatic model (Equation 3.1 and Equation 3.2) for a) inflation and b) deflation (respectively).

When the legs were inflated and deflated, the pressure dynamics matched an almost exponential rise and decay (Figure B.1). The inflation phase has a transition at 40 kPa where the bellows change from expanding to being fully expanded (Figure B.1a). Additional air added to the chamber after this point pressurizes the air rather than expanding the bellows. The deflation phase does not have this trait because the bellows are contracting at the same time as the compressed air is being released. We assumed that the pressure difference around the inflection point during the inflation phase was negligible.

When the chambers on each of the legs were inflated, the legs stiffness and damping coefficients changed (Figure B.2). As the pressure increased, the stiffness of the translational and

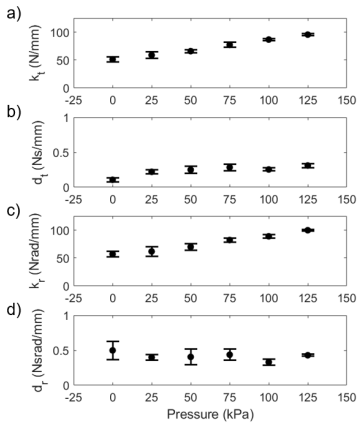

Figure B.2: Results for the linear mass-spring-damper models in translation and rotation. The stiffness and damping values were function of pressure in the inflated chamber. The stiffness in translation and rotation were roughly linearly increasing and the damping values roughly stay the same.

torsional elements increased linearly (Figure B.2a and B.2c) while the damping coefficients for the translational and torsional elements almost stayed the same (Figure B.2b and B.2d).

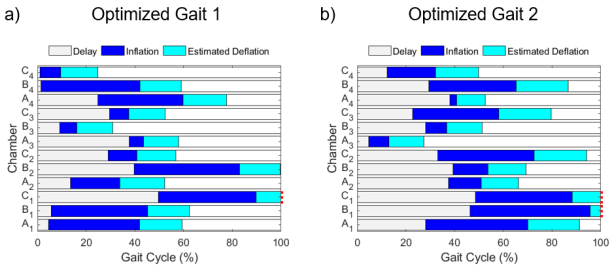

Figure B.3: Optimized gait sequences for walking on flat ground. a-b) Each chamber is inflated and deflated in a sequence over a gait cycle. Each gait cycle is then repeated so the robot can produce movement in a desired direction. The delay and inflation times are directly programmed on the microcontroller to make the robot walk. The estimated deflation depicted ends when pressure reaches 10kPa. The red dotted lines on the right of each bar plot indicates that the deflation stage for the corresponding chamber overlaps into the next gait cycle.

We used two different genetic algorithms to optimize the gait of the robot to walk on flat ground. Optimized Gait 1 used a larger number simulations when compared to Optimized Gait 2. Each of the genetic algorithms optimized the delay and inflation timing for the periodic gaits (Figure B.3).

Appendix C

Supplemental Materials: Pneumatic Circuits for Controlling the Gaits of Soft Legged Robots

C.1 Consistency of pneumatic circuit oscillations

The soft ring oscillators produced continuous oscillatory signals with minimal control inputs. To investigate the consistency of the periodic signal produced from the soft ring oscillator, we measured the pressure in one of the leg chambers during 10 oscillatory cycles, and plotted them together vs. the time since the start of each oscillation (Figure C.1). Over the oscillation period, the average standard deviation in the pressure between cycles was 9.4 kPa, with a worst case standard deviation of 15.5 kPa (19%) at $t = 1.8$ s.

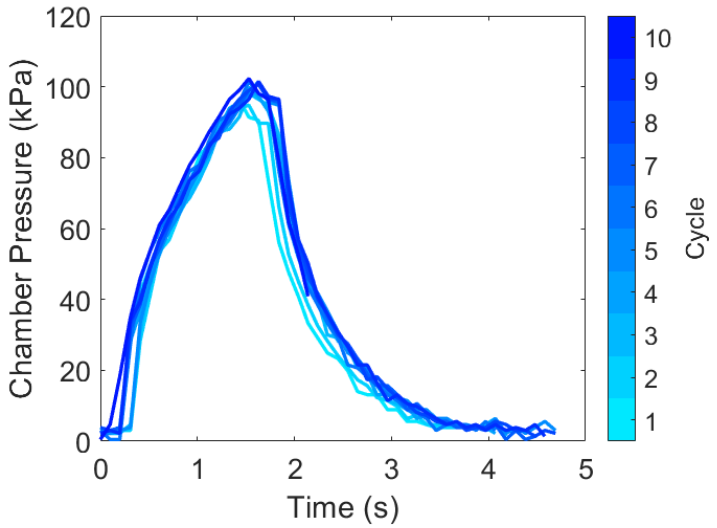

Figure C.1: Consistency of the soft ring oscillator. Pressure was measured at one node of the pneumatic circuit for 10 cycles and overlapped to show the consistency in the pressure oscillations in this component of the pneumatic circuit.

C.2 Robustness of pneumatic circuit to pressure variations

To demonstrate the ability of our pneumatic CPG-based circuit to reject pressure disturbances (e.g. as would be caused by, for example, impacts with the environment during the gait), we tracked the position of the end of a soft leg during a normal oscillatory cycle and then we perturbed the input pressure to the pneumatic circuit, reducing it to atmospheric pressure for roughly one half-cycle. (The 3D movement of the foot was projected onto an XY-plane orthogonal to the leg in its resting position, as seen in Figure C.2. The perturbation is labeled in blue on this figure.) The leg partially deflated and then the motion of the foot quickly returned to the pre-disturbance cycle. The red arrows on Figure C.2 indicate the direction of motion of the foot.

C.3 Quadruped Robot Assembly

This section presents a step-by-step guide to design, fabricate, and assemble the quadruped robot. Please refer to Figure 1 to see the each component on the assembled robot. The fabrication

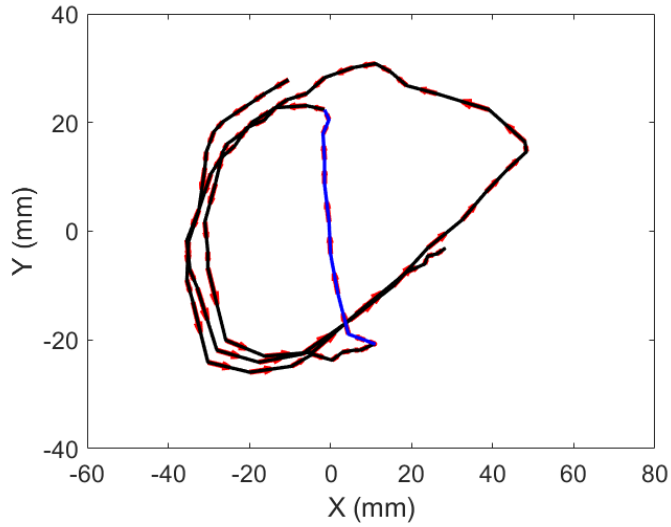

Figure C.2: Motion of the foot of the robot when the pressure in the pneumatic controller is perturbed. The position of the foot followed a cyclical trajectory during a normal oscillatory cycle (colored black). After the pneumatic circuit controlling the leg was temporarily perturbed by reducing the input pressure to atmosphere, the position of the foot deviated from the cyclical trajectory (colored blue). When this leak was sealed, the leg returned back to the normal oscillatory movement.

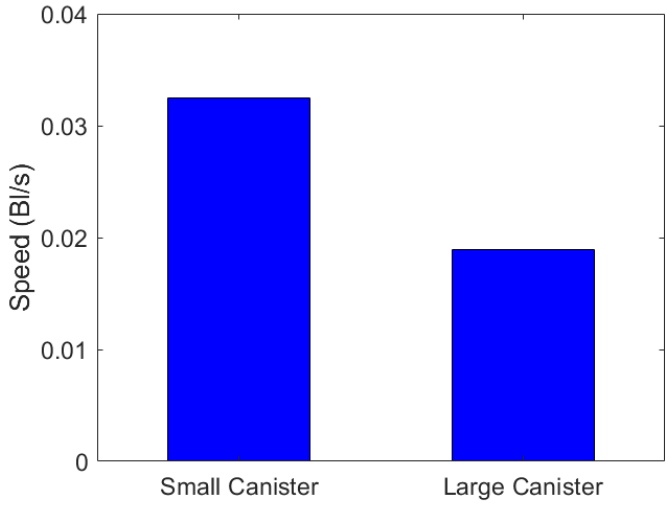

Figure C.3: Comparison of the speed of the robot while carrying the small (left) and large (right) CO_2 canisters and regulators.

and assembly process steps are as follows:

1. 3D Print Components

2. Leg Assembly

3. Quadruped Assembly

4. Valve Assembly

5. Sensor Assembly

1. **3D Print Components** The robot body, retaining rings, sensor boom, 3-2 valve mold, 4-2 valve mold, and sensor mold were 3D printed out of polylatic acid (PLA, Makerbot Replicator 2, Stratasys Inc.). We used a commercial multi-material 3D printer (Connex 3, Stratasys Inc.) to print the feet of the robot out of a soft material (TangoBlack+) for traction, as well as rigid back plates to mount the legs to the body of the robot (VeroClear). The foot assembly was composed of three parts: the soft treads, the center plate, and the connectors to the legs of the robot. The molds are composed of a three-part assembly and a cap. Two caps are fabricated for the 3-2 valve and 4-2 valve and one cap for the sensor mold. Each of the listed .stl files (Table C.1) are available to download and print.

Table C.1: List of .stl files

Object Name	**Part**	**Assembly**			
Robot Body	body_main.stl				
Sensor Boom	body_boom.stl				
Foot		foot_tread.stl	foot_plate.stl	foot_mount.stl	
Retaining Ring	leg_ring.stl				
Back Plate	leg_backplate.stl				
3-2 Valve Mold	3_2_mold_cap.stl	3_2_mold_bottom.stl	3_2_mold_excess.stl	3_2_mold_shell.stl	3_2_mold_top.stl
4-2 Valve Mold	4_2_mold_cap.stl	4_2_mold_bottom.stl	4_2_mold_excess.stl	4_2_mold_shell.stl	4_2_mold_top.stl
Sensor Mold	sen_mold_cap.stl	sen_mold_bottom.stl	sen_mold_excess.stl	sen_mold_shell.stl	sen_mold_top.stl

2. **Leg Assembly** The leg were composed of three parallel, connected chambers with bellows rotated 120 degrees about the longitudinal axis of the actuator. We used commercially-available plastic cylindrical bellows (Corr-A-Flex tubing, Teleflex Inc.) for the pneumatic chambers due to their extrinsic compliance (to allow bending) combined with the intrinsic

stiffness of the material (to permit large internal pressures). 3D printed retaining rings held the three pneumatic chambers together. We slid three retaining rings over the three chambers to fit into the grooves of the bellows. The back plates of the legs were tapped to attach threaded barbed adapters to the pneumatic lines. The three chambers were then press fit and glued onto the the feet and back plates.

3. **Quadruped Assembly** The legs of the quadruped are mounted on the body in the shape of an X for omnidirectional locomotion. The soft legs were mounted on a 3D printed rigid body frame. Each of the threaded adapters on the legs slide through the the three holes that are on the robot body with each foot oriented towards the ground. The base of each leg is then glued to the body of the robot.

4. **Valve Assembly** The 3-2 valve and 4-2 valve were composed of a cylindrical body, caps, and tubing. The body of the soft valves and caps were molded out of a soft polymer (MoldStar 30, Smooth-On Inc.). The polymer was poured into the cavity of the mold that form the cylindrical body of the valve. The polymer was also poured into the cap mold to form to the two caps of the valve. After the cylindrical body of the valve and the caps have cured, the opened/closed airways were fed through the holes in the caps. Each tube was connected to a barbed connector that contacts the membrane when the membrane switches state. we then used a silicone adhesive (SilPoxy) to adhere the caps to the cylindrical body. Tubes were fed through the side walls of the cylindrical body and the caps to create the inlet. The manufacturing process and assembly steps are similar for the 3-2 valve and the 4-2 valve except the 4-2 valve has twice the tubing routed through the caps.

5. **Sensor Assembly** The method used to manufacture the sensor is similar to the valves except there is only one cap. The fludic sensor channel is adhered to the cap of the sensor using a silicone adhesive (SilPoxy). Tubes were adhered to the side of the sensor to evacuate air bubbles in the sensor. The 3D printed sensor mount was press-fitted onto the wall of the

robot body and glued in place.

C.4 Considerations for future applications

This work presents an approach to the design of fluidic circuits that can be used to control a walking robotic toy. Since the circuits can be made completely out of molded or 3D printed polymers (rather than materials like metals and semi-conductors), we anticipate reduced materials costs. Furthermore, a single pneumatic source can be used to control multiple movements with simple pneumatic actuators, rather than requiring individual electromagnetic motors to control each behavior (e.g closing eyes, wiggling ears, and wagging tail would normally require a motor for each movement). Thus, this benefit increases with the complexity of the toy. The complexity of fabrication/assembly would also be reduced by combining the computation, sensing, and actuation components into a single fluidic system.

The soft fluidic valves can also be used in environments that do not allow metal such as in an MRI machine. Any metallic components can be placed outside of the MRI machine using a tethered version of the robot; the actuation and computation can be done in the MRI machine while the metallic pressure source used to operate the circuit can be moved to another location (it may also be possible to replace our metallic pressure vessel with an MRI-safe alternative).

Bibliography

[1] A. D. Marchese, C. D. Onal, and D. Rus, "Autonomous soft robotic fish capable of escape maneuvers using fluidic elastomer actuators," *Soft Robotics*, vol. 1, no. 1, pp. 75–87, 2014.

[2] N. W. Bartlett, M. T. Tolley, J. T. Overvelde, J. C. Weaver, B. Mosadegh, K. Bertoldi, G. M. Whitesides, and R. J. Wood, "A 3d-printed, functionally graded soft robot powered by combustion," *Science*, vol. 349, no. 6244, pp. 161–165, 2015.

[3] M. T. Tolley, R. F. Shepherd, B. Mosadegh, K. C. Galloway, M. Wehner, M. Karpelson, R. J. Wood, and G. M. Whitesides, "A resilient, untethered soft robot," *Soft Robotics*, vol. 1, no. 3, pp. 213–223, 2014.

[4] P. Polygerinos, Z. Wang, K. C. Galloway, R. J. Wood, and C. J. Walsh, "Soft robotic glove for combined assistance and at-home rehabilitation," *Robotics and Autonomous Systems*, vol. 73, pp. 135–143, 2015.

[5] B. S. Homberg, R. K. Katzschmann, M. R. Dogar, and D. Rus, "Haptic identification of objects using a modular soft robotic gripper," in *Intelligent Robots and Systems (IROS), 2015 IEEE/RSJ International Conference on*, pp. 1698–1705, IEEE, 2015.

[6] T. Ranzani, M. Cianchetti, G. Gerboni, I. De Falco, and A. Menciassi, "A soft modular manipulator for minimally invasive surgery: Design and characterization of a single module,"

[7] P. González de Santos, E. Garcia, and J. Estremera, *Quadrupedal Locomotion*. 2006.

[8] G. J. Tortora and B. H. Derrickson, *Principles of anatomy and physiology*. John Wiley & Sons, 2018.

[9] W. M. Kier and K. K. Smith, "Tongues, tentacles and trunks: the biomechanics of movement in muscular-hydrostats," *Zoological Journal of the Linnean Society*, vol. 83, no. 4, pp. 307–324, 1985.

[10] M. Calisti *et al.*, "An octopus-bioinspired solution to movement and manipulation for soft robots," *Bioinspir. Biomim.*, vol. 6, no. 3, p. 036002, 2011.

[11] R. V. Martinez, J. L. Branch, C. R. Fish, L. Jin, R. F. Shepherd, R. Nunes, Z. Suo, and G. M. Whitesides, "Robotic tentacles with three-dimensional mobility based on flexible elastomers," *Advanced Materials*, vol. 25, no. 2, pp. 205–212, 2013.

[12] T. Kalisky, Y. Wang, B. Shih, D. Drotman, S. Jadhav, E. Aronoff-Spencer, and M. T. Tolley, "Differential pressure control of 3d printed soft fluidic actuators," in *Intelligent Robots and Systems (IROS), 2017 IEEE/RSJ International Conference on*, pp. 6207–6213, IEEE, 2017.

[13] D. Drotman, S. Jadhav, M. Karimi, P. deZonia, and M. T. Tolley, "3D printed soft actuators for a legged robot capable of navigating unstructured terrain," in *Robotics and Automation (ICRA), 2017 IEEE International Conference on*, IEEE, 2017.

[14] F. Ilievski, A. D. Mazzeo, R. F. Shepherd, X. Chen, and G. M. Whitesides, "Soft robotics for chemists," *Angewandte Chemie International Edition*, vol. 50, no. 8, pp. 1890–1895, 2011.

[15] R. K. Katzschmann, J. DelPreto, R. MacCurdy, and D. Rus, "Exploration of underwater life with an acoustically controlled soft robotic fish," *Science Robotics*, vol. 3, no. 16, p. eaar3449, 2018.

[16] Z. Suo, "Theory of dielectric elastomers," *Acta Mechanica Solida Sinica*, vol. 23, no. 6, p. 549–578, 2010.

[17] M. Cianchetti, *Fundamentals on the Use of Shape Memory Alloys in Soft Robotics*, pp. 227–254. John Wiley Sons, Inc., 2013.

[18] A. D. Marchese, R. K. Katzschmann, and D. Rus, "A recipe for soft fluidic elastomer robots," *Soft Robotics*, vol. 2, no. 1, pp. 7–25, 2015.

[19] Y. Sun, Y. S. Song, and J. Paik, "Characterization of silicone rubber based soft pneumatic actuators," in *2013 IEEE/RSJ International Conference on Intelligent Robots and Systems*, pp. 4446–4453, Nov 2013.

[20] F. Connolly, C. J. Walsh, and K. Bertoldi, "Automatic design of fiber-reinforced soft actuators for trajectory matching," *Proceedings of the National Academy of Sciences*, vol. 114, no. 1, pp. 51–56, 2017.

[21] C.-P. Chou and B. Hannaford, "Measurement and modeling of McKibben pneumatic artificial muscles," *IEEE Transactions on Robotics and Automation*, vol. 12, pp. 90–102, Feb 1996.

[22] B. Tondu and P. Lopez, "Modeling and control of McKibben artificial muscle robot actuators," *IEEE Control Systems*, vol. 20, pp. 15–38, Apr 2000.

[23] F. Connolly, P. Polygerinos, C. J. Walsh, and K. Bertoldi, "Mechanical programming of soft actuators by varying fiber angle," *Soft Robotics*, vol. 2, no. 1, pp. 26–32, 2015.

[24] K. C. Galloway, P. Polygerinos, C. J. Walsh, and R. J. Wood, "Mechanically programmable bend radius for fiber-reinforced soft actuators," in *Advanced Robotics (ICAR), 2013 16th International Conference on*, pp. 1–6, IEEE, 2013.

[25] B. Mosadegh, P. Polygerinos, C. Keplinger, S. Wennstedt, R. F. Shepherd, U. Gupta, J. Shim, K. Bertoldi, C. J. Walsh, and G. M. Whitesides, "Pneumatic networks for soft robotics that actuate rapidly," *Advanced Functional Materials*, vol. 24, no. 15, pp. 2163–2170, 2014.

[26] A. D. Marchese, R. K. Katzschmann, and D. Rus, "Whole arm planning for a soft and highly compliant 2d robotic manipulator," in *Intelligent Robots and Systems (IROS 2014), 2014 IEEE/RSJ International Conference on*, pp. 554–560, IEEE, 2014.

[27] D. Rus and M. T. Tolley, "Design, fabrication and control of soft robots," *Nature*, vol. 521, no. 7553, pp. 467–475, 2015.

[28] R. L. Truby and J. A. Lewis, "Printing soft matter in three dimensions," *Nature*, vol. 540, pp. 371–378, 2016.

[29] E. Malone and H. Lipson, "Fab@home: the personal desktop fabricator kit," *Rapid Prototyping Journal*, vol. 13, no. 4, pp. 245–255, 2007.

[30] J. Morrow, S. Hemleben, and Y. Menguc, "Directly fabricating soft robotic actuators with an open-source 3-d printer," *IEEE Robotics and Automation Letters*, vol. 2, pp. 277–281, Jan 2017.

[31] R. MacCurdy, R. Katzschmann, Y. Kim, and D. Rus, "Printable hydraulics: a method for fabricating robots by 3d co-printing solids and liquids," in *Robotics and Automation (ICRA), 2016 IEEE International Conference On*, pp. 3878–3885, IEEE, 2016.

[32] M. Schaffner, J. A. Faber, L. Pianegonda, P. A. Rühs, F. Coulter, and A. R. Studart, "3d printing of robotic soft actuators with programmable bioinspired architectures," *Nature Communications*, vol. 9, p. 878, 2018.

[33] O. D. Yirmibesoglu, J. Morrow, S. Walker, W. Gosrich, R. Cañizares, H. Kim, U. Daalkhaijav, C. Fleming, C. Branyan, and Y. Menguc, "Direct 3d printing of silicone elastomer soft robots and their performance comparison with molded counterparts," in *2018 IEEE International Conference on Soft Robotics (RoboSoft)*, pp. 295–302, April 2018.

[34] R. L. Truby, M. Wehner, A. K. Grosskopf, D. M. Vogt, S. G. Uzel, R. J. Wood, and J. A. Lewis, "Soft somatosensitive actuators via embedded 3d printing," *Advanced Materials*, vol. 30, no. 15, p. 1706383, 2018.

[35] A. Zolfagharian, A. Kaynak, S. Y. Khoo, and A. Z. Kouzani, "Polyelectrolyte soft actuators: 3d printed chitosan and cast gelatin," *3D Printing and Additive Manufacturing*, vol. 5, no. 2, pp. 138–150, 2018.

[36] G. Haghiashtiani, E. Habtour, S.-H. Park, F. Gardea, and M. C. McAlpine, "3d printed electrically-driven soft actuators," *Extreme Mechanics Letters*, vol. 21, pp. 1–8, 2018.

[37] C. Yuan, D. J. Roach, C. K. Dunn, Q. Mu, X. Kuang, C. M. Yakacki, T. Wang, K. Yu, and H. J. Qi, "3d printed reversible shape changing soft actuators assisted by liquid crystal elastomers," *Soft Matter*, vol. 13, no. 33, pp. 5558–5568, 2017.

[38] T. Wallin, J. Pikul, and R. Shepherd, "3d printing of soft robotic systems," *Nature Reviews Materials*, p. 1, 2018.

[39] K. Kumar, J. Liu, C. Christianson, M. Ali, M. T. Tolley, J. Aizenberg, D. E. Ingber, J. C. Weaver, and K. Bertoldi, "A biologically inspired, functionally graded end effector for soft robotics applications," *Soft robotics*, 2017.

[40] S. Robyr, *FEM Modelling of a Bellows and a Bellows-based Micromanipulator*. 1999.

[41] R. J. Webster and B. A. Jones, "Design and Kinematic Modeling of Constant Curvature Continuum Robots: A Review," *The International Journal of Robotics Research*, vol. 29, pp. 1661–1683, nov 2010.

[42] A. Jönsson and M. Hermann, "Static characteristics of flexible bellows," 1997.

[43] Y. Li and S. Sheng, "Strength analysis and structural optimization of u-shaped bellows," *International Journal of Pressure Vessels and Piping*, vol. 42, no. 1, pp. 33–46, 1990.

[44] G. Z. Meng, G. M. Yuan, Z. Liu, and J. Zhang, "Forward and inverse kinematic of continuum robot for search and rescue," in *Advances in Manufacturing Science and Engineering*, vol. 712 of *Advanced Materials Research*, pp. 2290–2295, Trans Tech Publications, 7 2013.

[45] K. Reichl and D. Inman, "Dynamic mechanical and thermal analyses of objet connex 3d printed materials," *Experimental Techniques*, vol. 42, pp. 19–25, Feb 2018.

[46] C. D. Onal and D. Rus, "Autonomous undulatory serpentine locomotion utilizing body dynamics of a fluidic soft robot," *Bioinspiration & biomimetics*, vol. 8, no. 2, p. 026003, 2013.

[47] D. P. Holland, E. J. Park, P. Polygerinos, G. J. Bennett, and C. J. Walsh, "The soft robotics toolkit: Shared resources for research and design," *Soft Robotics*, vol. 1, no. 3, pp. 224–230, 2014.

[48] R. F. Shepherd, F. Ilievski, W. Choi, S. A. Morin, A. A. Stokes, A. D. Mazzeo, X. Chen, M. Wang, and G. M. Whitesides, "Multigait soft robot," *Proceedings of the National Academy of Sciences*, vol. 108, no. 51, pp. 20400–20403, 2011.

[49] M. T. Tolley, R. F. Shepherd, M. Karpelson, N. W. Bartlett, K. C. Galloway, M. Wehner, R. Nunes, G. M. Whitesides, and R. J. Wood, "An untethered jumping soft robot," in *2014 IEEE/RSJ International Conference on Intelligent Robots and Systems*, pp. 561–566, IEEE, 2014.

[50] D. S. Shah, J. P. Powers, L. G. Tilton, S. Kriegman, J. Bongard, and R. Kramer-Bottiglio, "A soft robot that adapts to environments through shape change," *Nature Machine Intelligence*, pp. 1–9, 2020.

[51] N. S. Usevitch, Z. M. Hammond, M. Schwager, A. M. Okamura, E. W. Hawkes, and S. Follmer, "An untethered isoperimetric soft robot," *Science Robotics*, vol. 5, no. 40, 2020.

[52] D. Drotman, M. Ishida, S. Jadhav, and M. T. Tolley, "Application-driven design of soft, 3-d printed, pneumatic actuators with bellows," *IEEE/ASME Transactions on Mechatronics*, vol. 24, no. 1, pp. 78–87, 2018.

[53] N. Cheney, R. MacCurdy, J. Clune, and H. Lipson, "Unshackling evolution: evolving soft robots with multiple materials and a powerful generative encoding," in *Proceedings of the 15th annual conference on Genetic and evolutionary computation*, pp. 167–174, ACM, 2013.

[54] F. Corucci, N. Cheney, F. G. Serchi, J. Bongard, and C. Laschi, "Evolving soft locomotion in aquatic and terrestrial environments: effects of material properties and environmental transitions," *Soft robotics*, vol. 5 4, pp. 475–495, 2018.

[55] X. Sui, H. Cai, D. Bie, Y. Zhang, J. Zhao, and Y. Zhu, "Automatic generation of locomotion patterns for soft modular reconfigurable robots," *Applied Sciences*, vol. 10, p. 294, Dec 2019.

[56] N. Cheney, J. Bongard, and H. Lipson, "Evolving soft robots in tight spaces," in *Proceedings of the 2015 Annual Conference on Genetic and Evolutionary Computation*, GECCO '15, (New York, NY, USA), p. 935–942, Association for Computing Machinery, 2015.

[57] R. Full and D. Koditschek, "Templates and anchors: neuromechanical hypotheses of legged locomotion on land," *Journal of Experimental Biology*, vol. 202, no. 23, pp. 3325–3332, 1999.

[58] P. Holmes, R. J. Full, D. Koditschek, and J. Guckenheimer, "The dynamics of legged locomotion: Models, analyses, and challenges," *SIAM Review*, vol. 48, no. 2, pp. 207–304, 2006.

[59] B. Gamus, L. Salem, A. D. Gat, and Y. Or, "Understanding inchworm crawling for soft-robotics," *IEEE Robotics and Automation Letters*, vol. 5, no. 2, pp. 1397–1404, 2020.

[60] S. Luo, M. Edmonds, J. Yi, X. Zhou, and Y. Shen, "Spline-based modeling and control of soft robots," in *2020 IEEE/ASME International Conference on Advanced Intelligent Mechatronics (AIM)*, pp. 482–487, 2020.

[61] I. Robert J. Webster and B. A. Jones, "Design and kinematic modeling of constant curvature continuum robots: A review," *The International Journal of Robotics Research*, vol. 29, no. 13, pp. 1661–1683, 2010.

[62] W. Huang, X. Huang, C. Majidi, and M. K. Jawed, "Dynamic simulation of articulated soft robots," *Nature communications*, vol. 11, no. 1, pp. 1–9, 2020.

[63] J. H. Holland, *Adaptation in Natural and Artificial Systems*. Ann Arbor, MI: University of Michigan Press, 1975. second edition, 1992.

[64] D. E. Goldberg, *Genetic Algorithms in Search, Optimization and Machine Learning*. Reading, MA: Addison-Wesley, 1989.

[65] Çulha, U. and Giardina, F., "Modeling, soft robotics toolkit." Accessed: 2020-06.

[66] D. Drotman, S. Jadhav, D. Sharp, C. Chan, and M. T. Tolley, "Electronics-free pneumatic circuits for controlling soft-legged robots," *Science Robotics*, vol. 6, no. 51, 2021.

[67] N. Heess, D. TB, S. Sriram, J. Lemmon, J. Merel, G. Wayne, Y. Tassa, T. Erez, Z. Wang, S. M. A. Eslami, M. Riedmiller, and D. Silver, "Emergence of locomotion behaviours in rich environments," 2017.

[68] T. Umedachi, V. Vikas, and B. Trimmer, "Softworms: the design and control of non-pneumatic, 3d-printed, deformable robots," *Bioinspiration & biomimetics*, vol. 11, no. 2, p. 025001, 2016.

[69] A. O'Halloran, F. O'malley, and P. McHugh, "A review on dielectric elastomer actuators, technology, applications, and challenges," *Journal of Applied Physics*, vol. 104, no. 7, p. 9, 2008.

[70] R. S. Kularatne, H. Kim, J. M. Boothby, and T. H. Ware, "Liquid crystal elastomer actuators: Synthesis, alignment, and applications," *Journal of Polymer Science Part B: Polymer Physics*, vol. 55, no. 5, pp. 395–411, 2017.

[71] P. Polygerinos, N. Correll, S. A. Morin, B. Mosadegh, C. D. Onal, K. Petersen, M. Cianchetti, M. T. Tolley, and R. F. Shepherd, "Soft robotics: Review of fluid-driven intrinsically soft devices; manufacturing, sensing, control, and applications in human-robot interaction," *Advanced Engineering Materials*, vol. 19, no. 12, p. 1700016, 2017.

[72] M. Ishida, D. Drotman, B. Shih, M. Hermes, M. Luhar, and M. T. Tolley, "Morphing structure for changing hydrodynamic characteristics of a soft underwater walking robot," *IEEE Robotics and Automation Letters*, vol. 4, no. 4, pp. 4163–4169, 2019.

[73] J. Zou, Y. Lin, C. Ji, and H. Yang, "A reconfigurable omnidirectional soft robot based on caterpillar locomotion," *Soft robotics*, vol. 5, no. 2, pp. 164–174, 2018.

[74] C. D. Onal, X. Chen, G. M. Whitesides, and D. Rus, "Soft mobile robots with on-board chemical pressure generation," in *Robotics Research*, pp. 525–540, Springer, 2017.

[75] R. K. Katzschmann, A. D. Marchese, and D. Rus, "Hydraulic autonomous soft robotic fish for 3d swimming," in *Experimental Robotics*, pp. 405–420, Springer, 2016.

[76] A. A. Calderón, J. C. Ugalde, J. C. Zagal, and N. O. Pérez-Arancibia, "Design, fabrication and control of a multi-material-multi-actuator soft robot inspired by burrowing worms," in *2016 IEEE international conference on robotics and biomimetics (ROBIO)*, pp. 31–38, IEEE, 2016.

[77] D. Ortiz, N. Gravish, and M. T. Tolley, "Soft robot actuation strategies for locomotion in granular substrates," *IEEE Robotics and Automation Letters*, vol. 4, no. 3, pp. 2630–2636, 2019.

[78] A. D. Marchese, K. Komorowski, C. D. Onal, and D. Rus, "Design and control of a soft and continuously deformable 2d robotic manipulation system," in *2014 IEEE international conference on robotics and automation (ICRA)*, pp. 2189–2196, IEEE, 2014.

[79] M. A. Unger, H.-P. Chou, T. Thorsen, A. Scherer, and S. R. Quake, "Monolithic microfabricated valves and pumps by multilayer soft lithography," *Science*, vol. 288, no. 5463, pp. 113–116, 2000.

[80] B. Mosadegh, A. D. Mazzeo, R. F. Shepherd, S. A. Morin, U. Gupta, I. Z. Sani, D. Lai, S. Takayama, and G. M. Whitesides, "Control of soft machines using actuators operated by a braille display," *Lab on a Chip*, vol. 14, no. 1, pp. 189–199, 2014.

[81] N. W. Bartlett, K. P. Becker, and R. J. Wood, "A fluidic demultiplexer for controlling large arrays of soft actuators," *Soft Matter*, 2020.

[82] M. Garrad, G. Soter, A. T. Conn, H. Hauser, and J. Rossiter, "A soft matter computer for soft robots," *Science Robotics*, vol. 4, no. 33, 2019.

[83] W. H. Grover, A. M. Skelley, C. N. Liu, E. T. Lagally, and R. A. Mathies, "Monolithic membrane valves and diaphragm pumps for practical large-scale integration into glass microfluidic devices," *Sensors and Actuators B: Chemical*, vol. 89, no. 3, pp. 315–323, 2003.

[84] W. H. Grover, R. H. Ivester, E. C. Jensen, and R. A. Mathies, "Development and multiplexed control of latching pneumatic valves using microfluidic logical structures," *Lab on a Chip*, vol. 6, no. 5, pp. 623–631, 2006.

[85] M. Rhee and M. A. Burns, "Microfluidic pneumatic logic circuits and digital pneumatic microprocessors for integrated microfluidic systems," *Lab on a chip*, vol. 9, no. 21, pp. 3131–3143, 2009.

[86] B. Mosadegh, C.-H. Kuo, Y.-C. Tung, Y.-s. Torisawa, T. Bersano-Begey, H. Tavana, and S. Takayama, "Integrated elastomeric components for autonomous regulation of sequential and oscillatory flow switching in microfluidic devices," *Nature physics*, vol. 6, no. 6, p. 433, 2010.

[87] K. W. Oh, K. Lee, B. Ahn, and E. P. Furlani, "Design of pressure-driven microfluidic networks using electric circuit analogy," *Lab on a Chip*, vol. 12, no. 3, pp. 515–545, 2012.

[88] N. S. G. K. Devaraju and M. A. Unger, "Pressure driven digital logic in pdms based microfluidic devices fabricated by multilayer soft lithography," *Lab on a Chip*, vol. 12, no. 22, pp. 4809–4815, 2012.

[89] M. Wehner, R. L. Truby, D. J. Fitzgerald, B. Mosadegh, G. M. Whitesides, J. A. Lewis, and R. J. Wood, "An integrated design and fabrication strategy for entirely soft, autonomous robots," *Nature*, vol. 536, no. 7617, pp. 451–455, 2016.

[90] S. T. Mahon, A. Buchoux, M. E. Sayed, L. Teng, and A. A. Stokes, "Soft robots for extreme environments: Removing electronic control," in *2019 2nd IEEE International Conference on Soft Robotics (RoboSoft)*, pp. 782–787, IEEE, 2019.

[91] P. Rothemund, A. Ainla, L. Belding, D. J. Preston, S. Kurihara, Z. Suo, and G. M. Whitesides, "A soft, bistable valve for autonomous control of soft actuators," *Science Robotics*, vol. 3, no. 16, p. eaar7986, 2018.

[92] D. J. Preston, P. Rothemund, H. J. Jiang, M. P. Nemitz, J. Rawson, Z. Suo, and G. M. Whitesides, "Digital logic for soft devices," *Proceedings of the National Academy of Sciences*, vol. 116, no. 16, pp. 7750–7759, 2019.

[93] D. J. Preston, H. J. Jiang, V. Sanchez, P. Rothemund, J. Rawson, M. P. Nemitz, W.-K. Lee, Z. Suo, C. J. Walsh, and G. M. Whitesides, "A soft ring oscillator," *Science Robotics*, vol. 4, no. 31, 2019.

[94] P. A. Guertin, "Central pattern generator for locomotion: anatomical, physiological, and pathophysiological considerations," *Frontiers in neurology*, vol. 3, p. 183, 2013.

[95] A. Roberts, W.-C. Li, and S. R. Soffe, "How neurons generate behaviour in a hatchling amphibian tadpole: an outline," *Frontiers in behavioral neuroscience*, vol. 4, p. 16, 2010.

[96] S. Grillner and T. M. Jessell, "Measured motion: searching for simplicity in spinal locomotor networks," *Current opinion in neurobiology*, vol. 19, no. 6, pp. 572–586, 2009.

[97] S. M. Danner, S. D. Wilshin, N. A. Shevtsova, and I. A. Rybak, "Central control of interlimb coordination and speed-dependent gait expression in quadrupeds," *The Journal of physiology*, vol. 594, no. 23, pp. 6947–6967, 2016.

[98] B. Bläsing and H. Cruse, "Stick insect locomotion in a complex environment: climbing over large gaps.," *The Journal of experimental biology*, vol. 207 Pt 8, pp. 1273–86, 2004.

[99] C. P. SPIRITO and D. L. MUSHRUSH, "Interlimb coordination during slow walking in the cockroach: I. effects of substrate alterations," *Journal of Experimental Biology*, vol. 78, no. 1, pp. 233–243, 1979.

[100] T. Buschmann, A. Ewald, A. von Twickel, and A. Büschges, "Controlling legs for locomotion—insights from robotics and neurobiology," *Bioinspiration & Biomimetics*, vol. 10, p. 041001, jun 2015.

[101] T. Barnes, T. Truong, G. Adams, and N. McGruer, "Large deflection analysis of a biomimetic lobster robot antenna due to contact and flow," *J. Appl. Mech.*, vol. 68, no. 6, pp. 948–951, 2001.

[102] A. J. Ijspeert, "Central pattern generators for locomotion control in animals and robots: A review," *Neural Networks*, vol. 21, no. 4, pp. 642 – 653, 2008. Robotics and Neuroscience.

[103] T. Umedachi, T. Kano, A. Ishiguro, and B. A. Trimmer, "Gait control in a soft robot by sensing interactions with the environment using self-deformation," *Royal Society open science*, vol. 3, no. 12, p. 160766.

[104] K. Luo, P. Rothemund, G. M. Whitesides, and Z. Suo, "Soft kink valves," *Journal of the Mechanics and Physics of Solids*, vol. 131, pp. 230–239, 2019.

[105] A. Jayes and R. M. Alexander, "The gaits of chelonians: walking techniques for very low speeds," *Journal of Zoology*, vol. 191, no. 3, pp. 353–378, 1980.

[106] R. Alexander, "Optimization and gaits in the locomotion of vertebrates," *Physiological reviews*, vol. 69, no. 4, pp. 1199–1227, 1989.

[107] R. M. Alexander, *Optima for animals*. Princeton University Press, 1996.

[108] M. MacKay-Lyons, "Central Pattern Generation of Locomotion: A Review of the Evidence," *Physical Therapy*, vol. 82, pp. 69–83, 01 2002.

[109] A. Pandey, D. E. Moulton, D. Vella, and D. P. Holmes, "Dynamics of snapping beams and jumping poppers," *EPL (Europhysics Letters)*, vol. 105, no. 2, p. 24001, 2014.

[110] D. Brown, "Tracker video analysis (2007)." Available at *http://physlets.org/tracker/*.

[111] Y. Gangamwar, V. Deo, S. Chate, M. Bhandare, and H. Deshpande, "Determination of curved beam deflection by using castigliano's theorem,"